| Volumen 41 | Número 3 | **SEPTIEMBRE-DICIEMBRE 2020**

UNA PUBLICACIÓN DE LA
SOMIB
Sociedad Mexicana de Ingeniería Biomédica

ib

REVISTA MEXICANA DE Ingeniería Biomédica

Nueva modalidad

Les recordamos que seguimos publicando bajo el esquema de *publicación continua*.

http://www.rmib.mx

ISSN 2395-9126

SOMIB
Sociedad Mexicana de Ingeniería Biomédica

Sociedad Mexicana de Ingeniería Biomédica

La Mesa Directiva de la Sociedad Mexicana de Ingeniería Biomédica hace una extensa invitación a las personas interesadas en participar, colaborar y pertenecer como Socio Activo de la SOMIB. La SOMIB reúne a profesionistas que se desarrollan en áreas de Ingeniería Biomédica, principalmente ingenieros biomédicos, así como otros profesionistas afines con el desarrollo de tecnología para la salud.

Membresía Estudiante
$850.00 ***PESOS MXN***
15% de descuento para grupos de 5 o más personas.

Membresía Profesional
$1,450.00 ***PESOS MXN***
15% de descuento para grupos de 5 o más personas.

Membresía Institucional
$11,600.00 ***PESOS MXN***
No aplica descuento.

Membresía Empresarial
$20,000.00 ***PESOS MXN***
La suscripción empresarial requiere invitación.

EL PAGO CUBRE UN AÑO DE CUOTA. EN CASO DE REQUERIR FACTURA
FAVOR DE SOLICITARLA, ADJUNTANDO COMPROBANTE DE PAGO Y ESPECIFICANDO CONCEPTO,
AL CORREO ELECTRÓNICO: ***facturación@somib.org.mx***

REVISTA MEXICANA DE Ingeniería Biomédica

AUTORES

Los trabajos a publicar en la RMIB, deben ser originales, inéditos y de excelencia. Los costos de publicación para autores son los siguientes:

NO SOCIOS:	***$4,060.00*** ***PESOS MXN*** *(INCLUYE I.V.A.)*
SOCIOS:	***$1,276.00*** ***PESOS MXN*** *(INCLUYE I.V.A.)*

PUBLICIDAD

A las empresas e instituciones interesadas en publicitar su marca o productos en la RMIB, los costos por número son los siguientes:

MEDIA PLANA:	***$4,999.00*** ***PESOS MXN*** *(INCLUYE I.V.A.)*
UNA PLANA:	***$6,799.00*** ***PESOS MXN*** *(INCLUYE I.V.A.)*
CONTRAPORTADA:	***$7,799.00*** ***PESOS MXN*** *(INCLUYE I.V.A.)*
FORROS INTERIORES:	***$7,799.00*** ***PESOS MXN*** *(INCLUYE I.V.A.)*

DESCUENTO DEL **20%** AL CONTRATAR PUBLICIDAD EN DOS O MÁS NÚMEROS.

Para ser socio

- Realiza el pago de derechos, de acuerdo a la categoría que te corresponde.
- Ingresa a *www.somib.org.mx/membresia* y elige el tipo de membresía por el cual realizaste el pago de derechos.
- Completa el formulario correspondiente y envíalo.
- Se emitirá carta de aceptación y número de socio por parte de la mesa directiva (aprobada la solicitud).
- Para mayor información sobre beneficios, ingresar a: *www.somib.org.mx* o comunícate al correo *socios@somib.org.mx*.

Datos bancarios

- **Beneficiario:** *Sociedad Mexicana de Ingeniería Biomédica A. C.*
- **Banco:** *Scotiabank*
- **Referencia:** *1000000333*
- **Cuenta:** *11006665861*
- **CLABE Interbancaria:** *044770110066658614*

La inserción de la publicidad será publicada en el libro electrónico y en el área de patrocinios en el sitio Web de la revista (RMIB), disponible en:

http://rmib.mx

REVISTA MEXICANA DE
Ingeniería Biomédica

Índices
La Revista Mexicana de Ingeniería Biomédica aparece en los siguientes índices científicos:
Sistema de Clasificación de Revistas Científicas y Tecnologías del CONACYT - Q4, SCOPUS, SciELO, EBSCO, Medigraphic Literatura Biomédica, Sociedad Iberoamericana de Información Científica - SIIC.

www.rmib.mx
ISSN 2395-9126

Asitente Editorial
Carla Ivonne Guerrero Robles

Editor Técnico y en Internet
Enrique Ban Sánchez

SOMIB
Sociedad Mexicana de Ingeniería Biomédica

Sociedad Mexicana de Ingeniería Biomédica
Periferico Sur #5374, Col. Olímpica, Alc. Coyoacán, C. P. 04710, Ciudad de México, CDMX, México (555) 574-4505

Afiliada a:
International Federation of Medical and Biological Engineering (IFMB-IUPSM-ICSU)
Federación de Sociedades Científicas de México, A.C. (FESOCIME)
Consejo Regional de Ingeniería Biomédica para América Latina (CORAL)

SOMIB
Periferico Sur #5374, Col. Olímpica, Alc. Coyoacán, C. P. 04710, Ciudad de México, CDMX, México (555) 574-4505
www.somib.org.mx

REVISTA MEXICANA DE INGENIERÍA BIOMÉDICA, Vol. 41, No. 3, Septiembre-Diciembre 2020, es una publicación cuatrimestral editada por la Sociedad Mexicana de Ingeniería Biomédica A.C., Periferico Sur #5374, Col. Olímpica, Alc. Coyoacán, C. P. 04710, (555) 574-4505, www.somib.org.mx, rib.somib@gmail.com. Editor responsable: César Antonio Díaz González. Reserva de derechos de uso exclusivo No. 04-2020-022012474000-102, ISSN (impreso) 0188-9532, ISSN (electrónico) 2395-9126; los tres otorgados por el Instituto Nacional de Derechos de Autor. Responsable de la última actualización de este número: Lic. Enrique Federico Ban Sánchez, Periferico Sur #5374, Col. Olímpica, Alc. Coyoacán, C. P. 04710, (555) 574-4505, fecha de última modificación, 1 de diciembre de 2020.

Disponible en línea:
www.rmib.mx

CONTENTS
CONTENIDO

RESEARCH ARTICLE

Vol. 41 | No. 3 | **SEPTIEMBRE - DICIEMBRE 2020** | pp 6-27

REVISTA MEXICANA DE Ingeniería Biomédica

dx.doi.org/10.17488/RMIB.41.3.1

E-LOCATION ID: 1034

Modified Oregonator: an Approach from the Complex Networks Theory

Oregonador Modificado: un Enfoque desde la Teoría de Redes Complejas

Jesús Andrés Arzola Flores, José Fernando Rojas Rodríguez, Esmeralda Vidal Robles

Benemérita Universidad Autónoma de Puebla

ABSTRACT

Within the framework of Systems Biology, this paper proposes the complex network theory as a fundamental tool for determining the most critical dynamic variables in complex biochemical mechanisms. The Belousov-Zhabotinsky reaction is proposed as a study model and as a complex bipartite network. By determining the structural property *authority*, the most relevant dynamic variables are specified, and a mathematical model of the Belousov-Zhabotinsky reaction is obtained. The bidirectional coupling of the proposed model was made with other models associated with biological processes, finding synchronization phenomena when varying the coupling parameter. The time series obtained from the numerical solution of the coupled models were used to construct their images using the *Gramian Angular Field* technique. In the end, a supervised learning tool is proposed for the classification of the type of coupling by analyzing the images, obtaining score percentages above 94%. The hereby proposed methodology could be extended to the experimental field in order to determine anomalies in the coupling and synchronization of different physiological oscillators.

KEYWORDS: Systems Biology; BZ Reaction; Complex Networks; Supervised Learning; Gramian Angular Field

RESUMEN

En el marco de la Biología de sistemas, se propone en el presente trabajo a la teoría de redes complejas como una herramienta fundamental para la determinación de las variables dinámicas más importantes en mecanismos bioquímicos complejos. Se emplea como modelo de estudio la reacción de Belousov-Zhabotinsky y se plantea como una red compleja bipartita. Mediante la determinación de la propiedad estructural *autoridad*, se determinan las variables dinámicas con mayor relevancia y se obtiene un modelo matemático de la reacción de Belousov-Zhabotinsky. Se realizó el acoplamiento bidireccional del modelo planteado con otros modelos asociados a procesos biológicos, encontrándose fenómenos de sincronización al variar el parámetro de acoplamiento. Las series de tiempo obtenidas de la solución numérica de los modelos acoplados se emplearon para construir sus respectivas imágenes mediante la técnica de *campo angular gramiano*. Finalmente, se propone una herramienta de aprendizaje supervisado para la clasificación del tipo de acoplamiento mediante el análisis de las imágenes, obteniéndose porcentajes de exactitud por encima del 94%. La metodología propuesta en el presente trabajo podría extenderse y trasladarse al campo experimental con la finalidad de determinar anomalías en el acoplamiento y sincronización de distintos osciladores fisiológicos.

PALABRAS CLAVE: Biología de sistemas; Reacción BZ; Redes Complejas; Aprendizaje supervisado; Campo angular gramiano

Corresponding author

TO: Esmeralda Vidal Robles

INSTITUTION: Benemérita Universidad Autónoma de Puebla

ADDRESS: Av. San Claudio S/N, Col. Ciudad Universitaria, C. P. 72570, Puebla, Puebla, México

E-MAIL: esmeralda.vidal@correo.buap.mx

Received:

11 February 2020

Accepted:

25 June 2020

INTRODUCTION

It is possible to study any physiological process through an intricate network of biochemical reaction mechanisms from the systems biology paradigm [1] [2] [3] [4], such mechanisms are responsible for regulating a wide variety of processes of utmost importance for life, through complex positive and negative feedback systems [5] [6]. A prominent example of negative feedback is the thyroid hormone regulatory mechanism [7] carried out by either thyroid cells or the leptin-insulin axis [8], which is strongly related to metabolic processes. Discrepancies in these feedback mechanisms can lead to multiple pathologies at the systemic level [7]. With the development of experimental tools for studying such complex systems, the need to understand the underlying dynamics of these regulatory mechanisms also arose, so biochemists undertook the task of studying the chemistry of these mechanisms to determine the kinetic parameters of the reactions participating in these processes. Meanwhile, biophysicists had to translate these biochemical processes to mathematical models using tools based on Dynamical Systems Theory (DST) and the discoveries made by biochemists [9] [10] [11].

B. Belousov was a Russian biophysicist who pioneered in the study of complex regulatory mechanisms present in biochemical processes at an experimental level. In 1950 he was given the task of proposing a reaction mechanism analogous to the Krebs cycle to study feedback processes [12] [13] [14]. Belousov conceived a chemical mixture made essentially of citric acid, bromate ions, and cerium ions in an acid medium under constant agitation [13]. During the reaction, Belousov observed that the mixture changed from being transparent to a yellow hue and vice versa. The phenomenon occurred time after time, being reminiscent of the Krebs cycle feedback processes. Nevertheless, his work was never officially published because reviewers concluded that the process was caused by mixture impurities, and that the phenomenon violated the natural laws of thermodynamics [13] [14]. Years later, Prigogine defined the basis of thermodynamics of irreversible processes [12] [13] [14].

Later on, another Russian biophysicist, A. Zhabotisky resumed Belousov's work. He replaced citric acid with malonic acid and cerium ions with iron ions to visualize chemical species concentration-oscillations obtaining a solution that shifted from red to blue and vice versa [12]. This chemical mechanism was thus named the Belousov-Zhabotinsky (BZ) reaction [12] [13] [14]. The work of Belousov and Zhabotinsky set the basis for the study of oscillatory biochemical processes [14].

In 1972, Field, Köros and Noyes proposed the first mathematical model in differential equations that described the underlying dynamics of the BZ reaction (FKN Model) and laid the groundwork for mathematical modeling of chemical mechanisms with oscillatory behaviors [15] [16]. This opened a vast field of study for the development of mathematical models in the area of systems biology [17]. The FKN model is extremely robust; however, it considers many chemical species as dynamic variables of the system, which makes it difficult to handle from an analytical point of view [15] [16]. To solve this problem, in 1974, Field and Noyes proposed a much simpler mechanism to describe reaction dynamics based on the FKN model, also known as *Oregonator* because it was created at the University of Oregon. However, said mathematical model was constructed from a reaction mechanism that consists of only five irreversible chemical reactions and that describes the BZ reaction qualitatively [18]. Years later, in 1990, Györgyi, Turányi, and Field proposed a detailed mechanism of the BZ reaction, that consisted of 80 chemical reactions and 27 chemical species and which is currently the most accepted reaction mechanism [19]. The BZ mechanism has two subsets, the first consists of a set of inorganic chemical reactions while the second one consists of organic chemical reactions. Just one year later, in his seminal

work *A history of chemical oscillations and waves*, Zhabotinsky presented a mathematical model in differential equations based on a subset of chemical reactions from the work of Györgyi et al., and mentioned that it is possible to explain BZ reaction dynamics with said subset [12]. At this point, the following questions arise: How reliable and valid is to reduce an extremely complex reaction mechanism to a subset of reactions? What criteria should be used to make this reduction? Could reducing the mechanism eliminate important system information? Is it possible to use mathematical tools to carry out this reduction properly without losing information? And if this is possible, can these mathematical techniques be used to study biochemical regulatory mechanisms to identify the most critical system variables?

To answer these questions, it is necessary to understand that DST is not the only mathematical tool used to study the complex mechanisms of biochemical regulation [20]. There are tools such as models of agents and cellular automata that have been used to explain at least qualitatively the phenomena that emerge from different physiological processes [20]. However, the tool that has attracted the most attention today is the Complex Networks Theory (CNT) based on graph theory [21] [22]. The CNT has been mainly developed by physicists, with the pioneering works of Barabasi et al., [23]. This theory has allowed us to understand the emergence of extremely complex behaviors in systems that involve a large number of variables because, through statistics, it enables us to study the structural properties of the networks to identify the variables or entities with greater relevance in the system of interest [24]. Multiple measures of centrality can be used to determine the level of importance of a variable in a complex network, such as degree, clustering, hub, *authority*, etc., [25]. In Biomedical research, CNT is widely used to study many phenomena including disease propagation, genetic regulation networks, protein-protein interaction networks, and identification of possible therapeutic targets in complex biochemical reaction mechanisms [25]. In their excellent work, Costa et al. describe the CNT as a vital tool for Systems Biology [26].

It is well known that the emergence of chronic degenerative diseases (such as insulin resistance, diabetes mellitus II, cancer, cardiovascular diseases among others) result from the mismatch of a wide variety of physiological processes that are in turn regulated by an intricate network of biochemical reactions, which makes it difficult to study the interaction, coupling, and activation that may exist between different physiological processes [27] [28] [29] 30]. The CNT could facilitate the study of different biochemical processes related to each other taking these processes as complex networks where the participating chemical species can be considered nodes or vertices, and all possible physicochemical interactions between them as links or edges. It is possible to identify the chemical species with greater relevance by determining network centrality properties, and applying the standard chemical kinetics techniques (CK) [31] gives rise to mathematical models in differential equations that facilitate the study of coupling and synchronization phenomena between different physiological processes and their possible relationship with various pathologies (see Figure 1).

It is necessary to identify when a group of physiological processes is coupled or synchronized, which requires tools that permit identifying such phenomena. Thanks to the development of machine learning, it is possible to create models capable of learning to recognize or identify a series of patterns with high precision through the acquisition of experience (data) [32]. Machine learning can be divided in supervised and unsupervised learning and can be further classified into different combinations of these [32] [33]. In general, supervised learning consists of providing a series of input data with their respective label to a model so

that the model is generalized and subsequently allows the label to be predicted knowing only the input data or characteristics [32] [33]. On the other hand, unsupervised learning consists of providing only the input data or characteristics to the model without its label, to identify specific patterns of information [32] [33]. Each supervised learning model must go through a training, validation, and testing process to ensure generalization [32] [33]. Supervised learning models can be divided into two large groups: classification models and regression models; in the former, the variable is to be predicted as a qualitative or categorical variable. In regression models, the variable to be predicted is a quantitative variable, either continuous or discrete [32] [33]. Hereby, the following question arises: Is it possible to use a supervised learning model to predict the coupling or synchronization of biochemical processes represented by systems of differential equations?

To answer this question, it is necessary to ask another one: How can data be provided to the supervised learning model to achieve the prediction of a coupling state? The answer is that by modeling biochemical processes as systems of differential equations and coupling them unidirectionally or bidirectionally, it is possible to numerically solve these models, from which the change in the concentration of chemical species with respect to time is obtained. Therefore, it is possible to determine if, for any value of the coupling parameter, these chemical species are synchronized. The degree of synchronization can be determined by evaluating some nonlinear metric, such as the fractal dimension of the time series, evaluation of Lyapunov exponents, entropy, the study of the synchronization variety in the phase space of the variables under study, etc. [35] [36] [37] [38], then it is possible to use some of these metrics to determine, through a supervised learning model, whether these systems are coupled or not. It is also possible to obtain images from the numerical solution of the systems of differential equations; such is the case of *recurrence diagrams* [39]

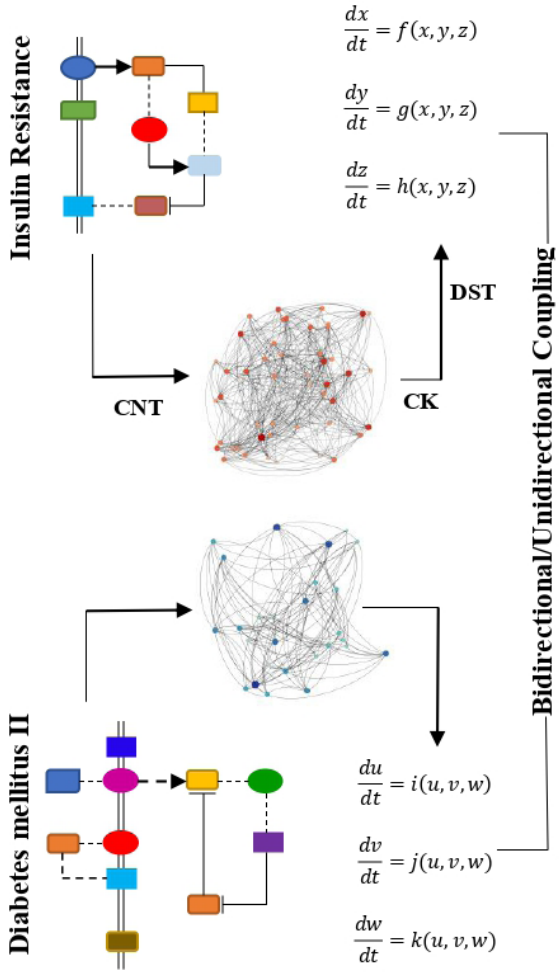

FIGURE 1. General diagram for obtaining a system of differential equations from a biochemical system. It is possible to build complex networks from biochemical reaction mechanisms and, through the network's structural properties, identify the most relevant variables to use CK standard tools to build a dynamic system that is representative of this process. Finally, coupling the systems of equations obtained employing a bidirectional or unidirectional coupling to study possible synchronization effects and their relationship with various pathologies. The block diagrams of the biochemical processes are only schematic representations of Insulin Resistance and Diabetes Mellitus II. The colors of the blocks and lines are also a graphic representation of the chemical species and the possible interactions present in these processes. However, they do not describe the actual biochemical process. For the construction of the network diagrams, the Gephi software was used (https://gephi.org/) [34].

[40] or *Gramian angular field images* (*gaf*) [40], which can be used with a supervised learning model to determine if a group of variables, in this case, chemical species related to important biochemical processes, are coupled or not, and thereafter, to associate a possible state of synchronization with various pathologies. Currently, it is possible to monitor blood concentration of a variety of chemical species related to critical metabolic processes, which are associated with different pathologies [41] [42] [43] [44], making it possible to construct time series and use them to build a database of *gaf* images to train, validate and test a supervised learning model to identify possible synchronization states and their relationship with pathologies; however, clinical trials can be expensive and, as a result, conducting this type of study is not practical [41] [42] [43] [44]. On the other hand, using mathematical models that represent the dynamics of these variables and using their numerical solution to obtain their respective *gaf* images to train, validate and test the supervised learning model, offers a solution to this problem. The ability of each mathematical model to represent a biochemical process depends on its degree of complexity, i.e., whether the model involves not only metabolic biochemical processes but also epigenetic processes [45].

To analyze the possibility of using CNT in biochemical regulatory mechanisms for identifying the most critical variables of the system and building a system of differential equations that model it, the BZ reaction was used as a study model since it is currently the most complex oscillating reaction discovered so far and it has been used to study the biochemical feedback mechanisms present in the Krebs cycle [12] [13] [14] [15] [16] [17] [18] [19]. On the other hand, to emulate the effects of coupling and synchronization, the obtained model was bidirectionally coupled with other models associated with oscillatory biochemical processes, and its numerical solution was used to obtain the *gaf* images. Finally, a supervised learning tool was used to identify the type of models coupled using the *gaf* images.

MATERIALS AND METHODS

For this study, the general mechanism of the BZ reaction proposed by Györgyi et al. [19] was used. A network was built considering two types of nodes or vertices, the "chemical species" type nodes, and the "chemical reaction" type nodes. The link or edge between species and chemical reactions is given by the reaction rate constant of each of the reactions, which gives place to a "bipartite" network [20] [21] [22] [23] [24] [25]. Once the network was built, the structural property *authority* was evaluated using the algorithm proposed by Kleinberg, which was initially proposed to determine the level of importance and information flow of websites, to reveal the sites with the highest traffic in a virtual hyperlink environment [46]. In this work, the structural property *authority* was used to determine the importance of each of the chemical species involved in the BZ reaction mechanism. To build a system of nonlinear differential equations capable of describing the BZ reaction mechanism, it was assumed that the most relevant variables have the most significant flow of "chemical" information. Once the most critical chemical species in the reaction mechanism were determined under the *authority* criteria, the mathematical model was constructed using standard techniques of CK [31]. When the model was obtained, the effects of synchronization that could emerge due to its coupling with different chemical oscillators were studied to emulate the synchronization processes present in different biochemical systems in mammals [47]. To this end, a bidirectional coupling was carried out with three different models [48]. The first one was an identical model, the second one was the model proposed by Levefer also called Brusselator [49] [50], which shows interesting autocatalytic processes and, lastly, the model proposed by Selkov that describes the oscillatory behaviors present in glycolysis [51] [52]. For each case, the coupling parameter was varied and the numerical solution of the systems of coupled differential equations was obtained using the standard fourth-order Runge Kutta technique [53]. Once the time series of the numerical solu-

tion of the differential equations were obtained, the image of the time series of the bidirectionally coupled variables was constructed using the *gaf* technique [54], which was described extensively by Wang et al [55]. In general, this technique consists in representing a time series in a polar coordinate system, each X_i value of the time series ($\tilde{X}$) is scaled so that all values are in the interval [-1,1] or [0,1], subsequently, with the rescaled values the angular cosine is obtained (φ_i= arccos (x_i), -1 ≤ x_i ≤ 1, $x_i \in \tilde{X}$) and the coordinate r ($r = \frac{t_i}{N}$, $t_i \in \mathbb{N}$), where t_i corresponds to the time interval between each value of the time series and N is a constant factor [55]. Lastly, the addition/subtraction between each point is determined to identify possible temporal correlations within different time intervals [55]. It is possible to obtain two types of *gaf*, the sum (*gasf*= cos (φ_i+φ_j)) and the subtraction (gadf= sin (φ_i+φ_j)). These values are used to construct the *Grammar matrix* that is used to obtain the image (see Figure 2) [55]. This technique in combination with supervised learning tools has been used to study time series of electroencephalograms [56], electrocardiograms [57], signals obtained from biosensors [58], etc.

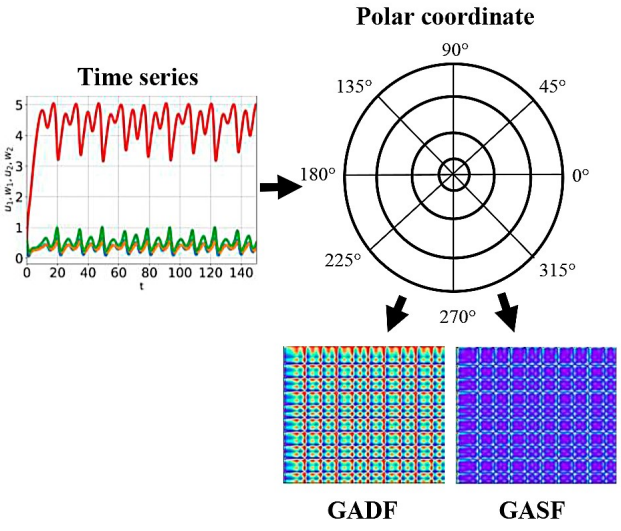

FIGURE 2. General diagram for obtaining the *gaf* images. The time series are rescaled, later these are represented in a polar coordinate system and finally, the *gaf* images are obtained.

After the *gasf* and *gadf* images were obtained, the supervised learning model was generated using the Orange Data Mining software (*https://orange.biolab.si/*) [58] [59], which is a visual toolbox where it is possible to build workflows that allow the use of widgets for analysis and data processing, supervised and unsupervised learning tools, data visualization and model evaluation. It also has extensions for text mining, spectroscopy, complex network analysis, time series, bioinformatics, and image analysis [59] [60] [61]. The transfer learning technique, which is an artificial intelligence technique that consists of pre-training a model with an extensive database and the experience gained from said training to apply it to another problem that may be completely different, was used to process the *gaf* images [61] [62] [63]. This technique is used in image processing as follows: deep convolutional neural networks (CNN) are used, which are pre-trained with a large number of images of all kinds, later, activations of the penultimate layer of the model (CNN codes) are used to represent the images with vectors (embedded), i.e., CNN is used as a feature extractor or descriptor, allowing supervised learning models to be used and thus obtaining high precision values in image classification [61] [62] [63]. In Orange, it is possible to embed images using different CNNs, including Google's Inception V3 neural network that has been pre-trained with the ImageNet database consisting of 1.2 million images. The neural network has 2048 nodes in its penultimate layer, so each image represents it with a vector of dimension 2048 [33] [64] (CNN by default in Orange). On the other hand, embedding images can also be done with CNN SqueezeNet, which is a much simpler network than Inception V3; nevertheless, it achieves a precision close to that of CNN AlexNet on the ImageNet database, this CNN represents each image as a vector of dimension 1000 [65]. It is also possible to embed with CNN's VGG16 and VGG19 proposed by the Visual Geometry Laboratory of the University of Oxford [66], in the same way, pre-trained with the ImageNet database, the CNN DeepLoc

pre-trained with 21882 images [67] and CNN Painters, a pre-trained network with 79433 images [59] [60] [61]. For embedding the images, Orange sends them to an external server, except for CNN SquezeeNet, which is done locally, making embedding faster. In this work, the *gaf* images were embedded using CNN Google Inception V3 and SquezeeNet. Subsequently, a supervised learning model was trained as a classifier of the type of coupled oscillators using the *gaf* images. A logistic regression with Ridge penalty or regularization (L2 = 1) was used as a classification method. Six different evaluation techniques were used to train, validate and test the classifier: 1) the standard stratified holdout technique (70% training set / 30% test set), the training and testing subsets are repeated 10 times (A), 2) a 3-fold stratified cross-validation (B), 3) a 5-fold stratified cross-validation (C), 4) a 10-fold stratified cross-validation (D), 5) a 20-fold stratified cross-validation (E) and 6) the leave-one-out cross-validation (F), to identify the best evaluation technique and avoid overfitting [33] [68] [69]. The previous procedure was repeated implementing a principal component analysis (PCA) using a number of components such that they explain 95% of the total variance of the images (21 principal components for Google Inception V3 and nine principal components for SquezeeNet). After embedding the images with the CNN, the same six evaluation techniques were used to study the effect of reducing dimensions and to avoid overfitting [33] [68] [69]. For both procedures the classifier confusion matrix was obtained to determine the classification metrics: Classification Accuracy (CA), Precision (P), Recall (R), and F1-score (F1) [33] [70].

RESULTS AND DISCUSSION

Figure 3a is a diagram that represents the complex network for the general mechanism of the BZ reaction proposed by Györgi et al. The nodes represent each of the 27 chemical species and 80 chemical reactions participating in the reaction mechanism, and the links represent the reaction rate constant magnitude. The largest nodes, which are shown in Table 1, represent the nodes with the highest numerical value of *authority*. Figure 3b shows the network *authority* property histogram. Of the 107 nodes, 49 (i.e. 45.79%) have an *authority* value between 0 and 0.1 (none being actually zero), 40 have an *authority* value between 0.1 and 0.2 (37.38%), 9 nodes between 0.2 and 0.3 (8.41%), 3 nodes between 0.3-0.4 (2.8%), 3 nodes between 0.4 and 0.5 (2.8%), 2 nodes between 0.5 and 0.6 (1.87%), and one between 0.9 and 1 (0.93%). This last one is the most important node, considering the *authority* centrality criterion. In the histogram, it is easy to distinguish that there are few nodes with a high *authority* value, making it possible to identify the chemical species with greater importance, possibly due to power-law-like behavior [71]. Power laws are present in a wide variety of biological phenomena and are related to processes of a universal nature [72].

As expected, the chemical node or species with higher *authority* is the H^+ cation because the chemical reaction at the experimental level is carried out in the presence of sulfuric acid (H_2SO_4), which is a source of H^+ and allows the formation of bromous acid ($HBrO_2$), an essential variable for the chemical feedback mechanism that enables the existence of periodic behaviors [12] [13] [14]. Furthermore, we can note that H_2O is the second chemical species with higher *authority* since the precursor solutions for the chemical reaction use deionized water as a solvent [12]. The third most crucial chemical species is the carboxy radical (*COOH) inasmuch as the breakdown of malonic acid as a precursor agent results in short-lived chemical species [12] [19]. The presence of Br* radicals is mainly because during the progress of the reaction molecular bromine (Br_2) occurs due to the bromate anion precursor agent (BrO_3), said Br_2 results in the formation of bromide ions (Br^-) and subsequently to Br* radicals, which are fundamental chemical species for the feedback mechanism [12] [19]. Because the chemical reaction includes organic components, specifically malonic acid and its

derivatives, it has carboxyl or carbonic acid groups that can be decomposed into carbon dioxide (CO_2), which is seen in the form of gas bubbles during the reaction [12] [13] [14].

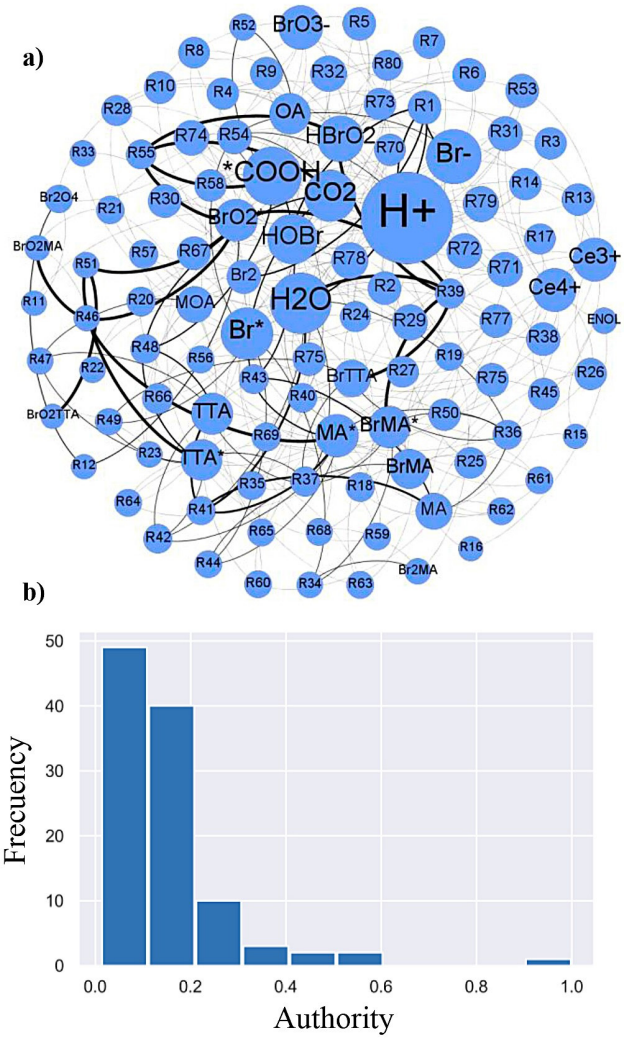

FIGURE 3. a) The complex network of the chemical mechanism of Györgyi et al [19]. The larger nodes correspond to those that have greater authority value; b) Histogram of structural property *authority*. It can be observed that most of the nodes have an *authority* value below 0.3 (91.58%), however, there are few nodes with *authority* values above 0.3 (8.42%), which can be considered as the most important nodes under the criterion of centrality *authority*. Gephi software was used for the construction of the network diagram (https://gephi.org/) [34].

Lastly, we can see that the oxidized form of the Cerium metal (Ce^{4+}) is also among the ten nodes with the highest *authority* value, this results from said chemical species acting as a catalytic agent in the chemical reaction and that alongside its reduced form (Ce^{3+}), it gives rise to the typical color changes of the BZ reaction [12] [18]. With these results, it is possible to observe that applying CNT to the BZ reaction mechanism proposed by Györgyi et al. [19] permits identifying the chemical species with greater relevance under the criterion of *authority*. Such chemical species appear naturally in the mechanism described by Zhabotinsky, either in its ionic form or in the form of a precursor compound [12], so it is possible to approximate the BZ reaction to said subset of reactions. Still, it is essential to mention that it is possible to use other centrality criteria to identify the nodes with greater relevance [25].

TABLE 1. *Authority* values.

Node	Authority
H^+	1
H_2O	0.5435
*COOH	0.5086
Br^-	0.4598
Br*	0.4133
CO_2	0.4062
HOBr	0.3870
$HBrO_2$	0.3289
BrO_3^-	0.3030
Ce^{4+}	0.2939

The mechanism proposed by Zhabotisnky uses Iron (Fe) as a catalyst instead of Cerium (Ce) [12]. Below is the chemical mechanism studied by Zhabotinsky replacing Fe with Ce.

BZ Chemical model [12]

1. $H^+ + HBrO_3 + HBrO_2 \leftrightarrow HBrO_2^+ + BrO_2 + H_2O$
2. $BrO_2 + H^+ \leftrightarrow HBrO_2^+$
3. $Ce^{3+} + HBrO^{2+} \leftrightarrow Ce^{4+} + HBrO^2$
4. $H^+ + 2HBrO_2 \leftrightarrow HOBr + HBrO_3 + H^+$
5. $H^+ + Br^- + HBrO_2 \leftrightarrow 2HOBr$

6. $H^+ + Br^- + HOBr \leftrightarrow Br_2 + H2O$
7. $H^+ + Br^- + HBrO_3 \leftrightarrow HBrO_2 + HOBr$
8. $2Ce^{4+} + CHBr(COOH)_2 \leftrightarrow 2Ce^{3+} + CBr(COOH)_2 + H^+$
9. $H_2O + CBr(COOH)_2 \leftrightarrow H^+ + Br^- + COH(COOH)_2$
10. $HOBr + CHBr(COOH)_2 \leftrightarrow CBr_2(COOH)_2 + H_2O$
11. $Br_2 + CHBr(COOH)_2 \leftrightarrow CBr_2(COOH)_2 + H^+ + Br^-$
12. $H_2O + CHBr(COOH)_2 \leftrightarrow CHOH(COOH)_2 + H^+ + Br^-$

To make studying the reaction mechanism easier, it is possible to make the following variable change: A= [$HBrO_3$]; B= [Any organic species derived from malonic acid]; P= [HOBr]; X= [$HBrO_2$]; Y=[Br^-]; Z= [Ce^{4+}]; C= [Ce^{3+}]+[Ce^{4+}]; $h_0 \approx H^+$ [12]; therefore, the chemical mechanism is transformed into:

1. $h_0 + A + X \leftrightarrow HBrO_2^+ + BrO_2 + H_2O$
2. $BrO_2 + h_0 \leftrightarrow HBrO_2^+$
3. $C\text{-}Z + HBrO_2^+ \leftrightarrow Z + X$
4. $h_0 + 2X \leftrightarrow P + A + h_0$
5. $h_0 + Y + X \leftrightarrow 2P$
6. $h_0 + Y + P \leftrightarrow Br_2 + H_2O$
7. $h_0 + Y + A \leftrightarrow X + P$
8. $2Z + B \leftrightarrow 2[C\text{-}Z] + B + h_0$
9. $H_2O + B \leftrightarrow h_0 + Y + B$
10. $P + B \leftrightarrow B + H_2O$
11. $Br_2 + B \leftrightarrow B + h_0 + Y$
12. $H_2O + B \leftrightarrow B + h_0 + Y$

Considering species A, B and P as constants and chemical reactions as elementary (the power of variables X, Y, and Z is directly related to their stoichiometric coefficients), it is possible to use the standard techniques of CK to construct reaction speed laws [12] [31]:

Equations 1

1. $V_X = k_1 h_0 AX$
2. $V = k_2[BrO_2]h_0$
3. $V_Z = k_3[HBrO_2^+][C\text{-}Z]$
4. $V_X = k_4 h_0 X_2$
5. $V_X = k_5 h_0 X_Y$
6. $V_Y = h_0 PY$
7. $V_X = k_7 h_0 AY$
8. $V_Z = k_8 BZ$
9. $V_Y = k_9 B$
10. $V = k_{10} PB$
11. $V_Y = k_{11}[Br_2]B$
12. $V_Y = K_{12} B$

Where the variables X, Y, and Z are the variables that generally describe the chemical mechanism of the BZ reaction [12]. Using the law of mass action, the following system of nonlinear differential equations is obtained. It models the change of X, Y, and Z with respect to time and as a function of the chemical concentrations of the precursors [12]:

Equations 2

$$\frac{dX}{dt} = k_1 h_0 AX - k_5 h_0 XY + k_7 h_0 AY - 2k_4 h_0 X^2,$$

$$\frac{dY}{dt} = \frac{F k_8 k_9 BZ}{k_{-8} h_0 (C-Z) + k_9} - k_5 h_0 XY - k_7 h_0 AY + k_{12} B,$$

$$\frac{dZ}{dt} = 2k_1 h_0 AX - \frac{k_8 k_9 BZ}{k_{-8} h_0 (C-Z) + k_9}.$$

Where k_i are the reaction rate constants and F is a stoichiometric factor used as an adjustment parameter [12] [13]. It is possible to simplify the model by dividing the numerator and denominator of the term $\frac{k_8 k_9 BZ}{k_{-8} h_0 (C\text{-}Z) + k_9}$ by k_9, then doing a geometric series development and neglecting terms of greater order $k_8 BZ \frac{1}{\frac{k_8 h_0 (C\text{-}Z)}{k_9} + 1} \approx k_8 BZ$ is obtained. Therefore, assuming that the concentration of H^+ remains constant and that $F = \frac{1}{2} f$, then the model proposed by Zhabotinsky can be reduced to [14]:

Equations 3

$$\frac{dX}{dt} = k_1 AX - k_5 XY + k_7 AY - 2k_4 X^2,$$

$$\frac{dY}{dt} = \frac{1}{2} f k_8 BZ - k_5 XY - k_7 AY + k_{12} B,$$

$$\frac{dZ}{dt} = 2k_1 AX - k_8 BZ.$$

The model described above is very similar to that proposed by Field and Noyes [13] [18], except for the term $k_{12}B$, which is related to the rate at which chemical species derived from malonic acid, specifically $CHBr(COOH)_2$ by its decomposition, it leads to the formation of new Br^- ions, which cannot be neglected from the mathematical model because they have a strong implication in the feedback process of the BZ reaction [12] [19] since the excessive production of these can lead to complete inhibition of oscillations. Also, these ions actively participate in the production of $HBrO_2$, which in turn facilitates the process of changing the oxidation state of the Ce catalyst.

Making the change of variable [13]:

$$u = \left[\frac{2k_4X}{k_1A}\right]; v = \left[\frac{k_5Y}{k_1A}\right]; w = \left[\frac{k_8k_4BZ}{(k_1A)^2}\right]; t = k_8B\tau.$$

So, Equations 3 in their dimensionless form are:

Equations 4

$$\frac{du}{d\tau} = \frac{qv-uv+u-u^2}{\varepsilon},$$

$$\frac{dv}{d\tau} \frac{-qv-uv+fw^2+\alpha}{\varepsilon'},$$

$$\frac{dw}{d\tau} = (u-w).$$

Where $\varepsilon = \frac{k_8B}{k_1A}$; $\varepsilon' = \frac{2k_4k_8B}{k_5k_1A}$; $q = \frac{2k_7k_4}{k_5k_1}$; $\alpha = \frac{k_{12}B}{k_1A}$.

However, as in the model proposed by Field and Noyes, the parameter ε', is very small compared to ε [13] [18]; therefore, it is possible to consider that the variable v, remains in a stationary state, so the system of Equations 4 can be reduced to:

Equations 5

$$\varepsilon\frac{du}{dt} = u(1-u) + (f\mathrm{w}+\alpha)\frac{q-u}{q+u},$$

$$\frac{dw}{dt} = u - w.$$

We named this model *Modified Oregonator* (NOM). Amemiya et al. [73], and Krug et al. [74], associated the term to the sensitivity of the BZ reaction to the presence of oxygen and its photosensitivity. In contrast, we associate this term with the decomposition of the derivatives of the malonic acid that give rise to Br- reduction. The chemical mechanism proposed by Györgyi et al. was used as a starting point [19] identifying the most relevant chemical species through the CNT under the *authority* criterion, which approximates the reaction mechanism BZ, to the subset of reactions proposed by Zhabotisky [12].

To emulate the synchronization processes present in different physiological systems, the mathematical model obtained in this work was coupled with different oscillators, all of them dimensionless. The parameters of the models were selected according to the stability criteria to ensure the presence of oscillations [13] [18]. The coupling was linear bidirectional in all cases, and the coupling force is modulated by parameter k. The system of Equations 6 shows two coupled NOM oscillators:

Equations 6

$$\varepsilon_1\frac{du_1}{dt} = u_1(1-u_1) + (f_1w_1+\alpha_1)\frac{q_1-u_1}{q_1+u_1} + k(u_2-u_1),$$

$$\frac{dw_1}{dt} = u_1 - w_1,$$

$$\varepsilon_2\frac{du_2}{dt} = u_2(1-u_2) + (f_2w_2+\alpha_2)\frac{q_2-u_2}{q_2+u_2} + k(u_1-u_2),$$

$$\frac{dw_2}{dt} = u_2 - w_2.$$

The system of Equations 7, shows the NOM model coupled with the Brusselator model:

Equations 7

$$\varepsilon\frac{du_1}{dt} = u_1(1-u_1) + (fw_1+\alpha)\frac{q-u_1}{q+u_1} + k(u_2-u_1),$$

$$\frac{dw_1}{dt} = u_1 - w_1.$$

$$\frac{du_2}{dt} = a - bu_2 + u_2^2 w_2 - u_2 + k(u_1 - u_2),$$

$$\frac{dw_2}{dt} = bu_2 - u_2^2 w_2.$$

And lastly, the NOM model was coupled with the Selkov glycolysis mathematical model (Equations 8),

Equations 8

$$\varepsilon \frac{du_1}{dt} = u_1(1 - u_1) + (fw_1 + \alpha)\frac{q - u_1}{q + u_1} + k(u_2 - u_1),$$

$$\frac{dw_1}{dt} = u_1 - w_1.$$

$$\frac{du_2}{dt} = \nu - \frac{u_2 w_2^{\gamma}}{w_2^{\gamma} u_2 + w_2^{\gamma} + 1} + k(u_1 - u_2),$$

$$\frac{dw_2}{dt} = \beta\left(\frac{u_2 w_2^{\gamma}}{w_2^{\gamma} u_2 + w_2^{\gamma} + 1}\right) - \eta w_2.$$

In Figure 4a, the numerical solution of the system of Equations 6 is shown. A full synchronization can be seen between variables u_1 and u_2, i.e., the oscillation rhythms are completely coupled [48] [75]. This type of behavior is common in biochemical processes carried out by cells that share the same microenvironment and can be stimulated either by a chemical or physical mechanism [76] [77]. On the other hand, in Figure 4b the gasf image of the variable u_1 can be seen, while in Figure 4c, the *gadf* image of the variable u_2 is shown. A characteristic pattern of bidirectional coupling between identical oscillators with periodic behavior can be seen in both figures.

In Figure 5a, the numerical solution for the system of Equations 7 is shown. Almost complete synchronization can be seen between the variables u_1, w_1 and u_2 [48] [75]. Anyway, this system of coupled differential equations is very sensitive to the value of the coupling parameter. Also, Figure 5b shows the *gasf* image of the variable u_1, while Figure 5c shows the gadf image of the variable u_2. In both figures, a characteristic pattern for a quasi-periodic system can be seen [78].

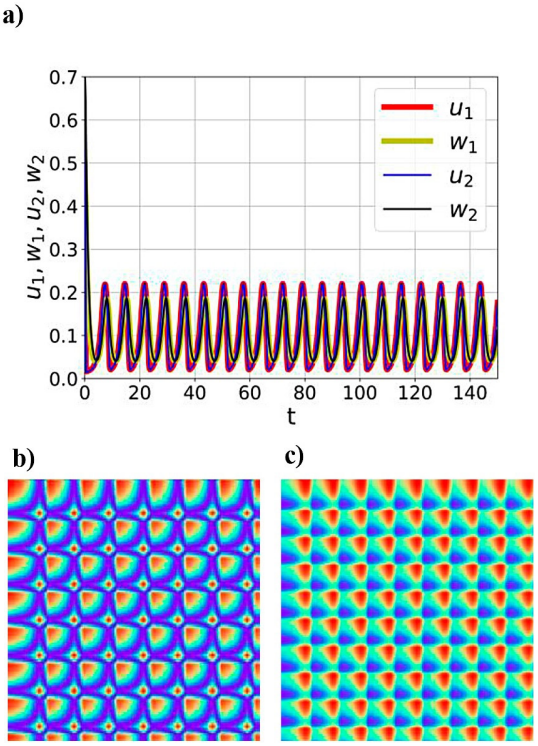

FIGURE 4. a) Numerical solution of the system of Equations 6 with $\varepsilon_1 = \varepsilon_2 = 0.3$, $\alpha_1 = \alpha_2 = 0.03$, $q_1 = q_2 = 0.015$, $f_1 = f_2 = 1.0$ and $k = 1.0$. With $u_1(0) = 0.3$, $w_1(0) = 0.5$, $u_2(0) = 0.8$ and $w_2(0) = 0.7$, tf=150 units of dimensionless time and dt=0.001. An oscillatory behavior is shown for the 4 dynamic variables of the system and full synchronization is observed; b) *gasf* image of the variable u_1; c) *gadf* image of the variable u_2. For both images, a characteristic pattern of periodic systems can be seen.

In Figure 6a, the numerical solution of the system of Equations 8 is shown. The phase synchronization between the variables u_1, u_2 and w_1 [48] [75] can be seen. The NOM model oscillation rhythm causes variable u_2 to enter in-phase synchronization; however, the variable w_2 decays completely to zero. In the Selkov model, the variable u_2 is related to the concentration of ATP (adenosine triphosphate), while the variable w_2 is related to the concentration of ADP (adenosine diphosphate) [51] [52], so when said system is coupled with the NOM model, the synchronization process that could exist between the biochemical mechanism of glycolysis and the Krebs cycle is emulated.

Moreover, in Figure 6b the gasf image of the variable u_1 can be seen, while in Figure 6c the *gadf* image of the variable u_2 is shown. It can be distinguished that the *gasf* field shows the typical oscillatory behavior, while the image of the gadf field does not clearly show a distinct pattern.

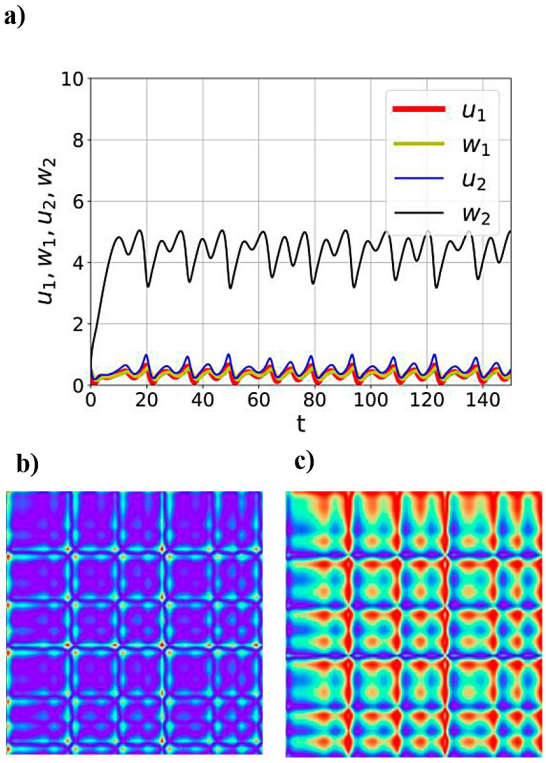

FIGURE 5. a) Numerical solution of the system of Equations 7 with ε= 0.3, α= 0.03, q= 0.015, f= 1.0, a= 1, b= 2.5 and k= 2.5. With u_1 (0)= 0.3, w_1 (0)= 0.5, u_2 (0)= 0.8 and w_2 (0)= 0.7, tf= 150 units of dimensionless time and df=0.001. A quasi-periodic behavior is shown for the 4 dynamic variables of the system and almost complete synchronization is observed between the variables u_1, u_2 and w_1; b) *gasf* image of the variable u_1; c) *gadf* image of the variable u_2. The images reflect the quasi-periodic behavior of the variables u_1 and u_2.

The numerical solution of the equations without coupling can be found in the supplementary material, as well as their respective *gasf* and *gadf* images (see Figures S1, S2 and S3). The coupling of chemical oscillators to emulate the synchronization in biochemical processes, is of vital importance since it allows us to understand the complex dynamics that underlie the feedback processes present in biological systems. Mismatches in the oscillation rhythms of physiological processes can lead to a wide variety of metabolic problems [7], so it is essential to know the type of coupling that can exist between oscillators (unidirectional, bidirectional, linear, nonlinear, etc., [48].) and whether these are coupled or not at any given time.

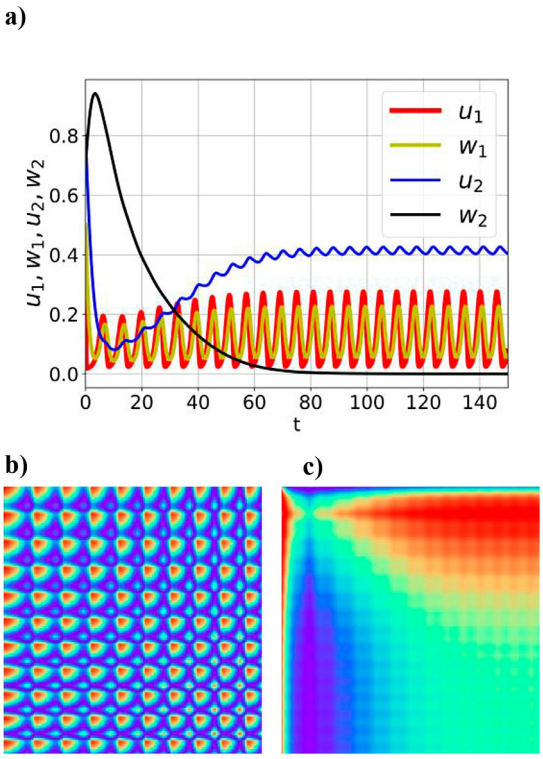

FIGURE 6. Figure 6. a) Numerical solution of the system of Equations 8 with ε= 0.3, α= 0.03, q= 0.015, f= 1.0, v= 0.0285, η= 0.1, β= 1.0, γ= 2 and k= 0.1. With u_1 (0)= 0.3, w_1(0)= 0.5, u_2 (0)= 0.8 and w_2 (0)= 0.7, tf= 150 units of dimensionless time and df= 0.001. Oscillatory behavior is distinguished for the variables u_1, u_2, and w_1, as well as phase synchronization between them. It is recognized that the variable w_2, for this case of the value of the parameters, tends to zero; b) *gasf* image of the variable u_1; c) *gadf* image of the variable u_2. The *gasf* image shows a typical pattern of a periodic oscillatory system. On the other hand, although the variable u_2 shows an oscillatory behavior, it is also coupled with the variable w_2, which is why a well-defined pattern in the *gadf* image is not clearly distinguished.

To determine coupled oscillators type, the coupling parameter was varied between one and ten for the system of Equations 6, between one and ten for the system of Equations 7 and lastly, between 0.1 and 1 for the system of Equations 8 (because this system is highly sensitive to bidirectional coupling), to generate the images of the time series using the *gaf* technique. Once obtained, the images were embedded to subsequently train the supervised learning model using the procedure described in the materials and methods section (see Figure 7). Figure 8 shows the general Orange workflow for this procedure. In the supplementary material (Tables TS-1 and TS-2), the results of the evaluation of different models of supervised learning are shown (Multilayer Perceptron Neural Network (MLP) (Hyperparameters: Optimizer: L-BFGS-B, activation function: Logistics, regularization L2= 1, neurons in one hidden layer: 10, tol= 1E-4, max_iter= 200), K-Nearest-Neighbors (Hyperparameters: Number of nearby neighbors: 5, metric: Euclidean, wight= uniform) and Support Vector Machine (SVM) (Hyperparameters: Cost= 1.0, kernel: RBF, tol= 1E-3, iteration limit= 100)) [33] [68], which were used to classify the type of coupled oscillators using the gaf images, to compare them with those obtained with the logistic regression model. When training the different supervised learning models using the vectors provided by CNN SquezeeNet as image descriptors, the logistic regression model presented the highest CA and F1 values for all evaluation techniques, obtaining the maximum values in the methods A, D, E and F (CA= 0.983 and F1= 0.983). In contrast, the minimum values were obtained from methods B and C (CA= 0.966 and F1= 0.967) (see supplementary Tables ST-1). When using CNN Inception V3 to embed the images, similar values of CA and F1 were obtained for the logistic regression models, MLP and KNN for method A (CA= 0.961, F1= 0.961), methods B, C, D, E and F (CA= 0.950 and F1= 0.949-0.950). The SVM model presents the highest CA and F1 for methods B and C (CA= 0.966 and F1= 0.966). Notwithstanding, for methods D, E and F, the SVM model presents similar CA and F1 than the rest of the models (CA= 0.950 and F1= 0.949) (see supplementary Tables ST-1). Likewise, it is possible to observe that there are no major differences between the results obtained by CNN's Inception V3 and SquezeeNet. Godec et al., use transfer learning to embed biomedical images and mention that this technique allows them to obtain high precision values in classification models using small databases [61]. Godec et al., also found no major differences in the CA and F1 values of the logistic regression classifier when using either the CNN Inception V3 or the CNN SquezeeNet to embed the images [61].

It is worth mentioning that sometimes when the database used for training supervised learning models has a higher number of characteristics or descriptors compared to the sample size (as is often the case in biomedical databases), or is unbalanced, i.e., there is a greater amount of data from one class than from the rest, it is possible to overfit the model, leading to erroneous results [33] [61] [68] [69]. However, it is possible to prevent overfitting essentially through two procedures, the first is to use more data for training, decrease statistical bias and decrease the number of characteristics or descriptors, the second one is to limit the complexity of the model of supervised learning, employ regularization, either penalty L2 (Ridge), L1 (Lasso) or ElasticNet (L1 and L2 simultaneously) and use assessment techniques such as stratified cross-validation or leave-one-out cross-validation [33] [68] [79] [80] [81] [82] [83]. Therefore, we have also implemented a PCA after embedding the images with CNN's to study the effect of the reduction of dimensions in the classification of the type of coupled oscillators, using the same models of supervised learning and the same evaluation methods.

When performing the PCA implementation after embedding the images with CNN SquezeeNet using nine main components, which explain 95% of the total variance, the logistic regression model obtains the

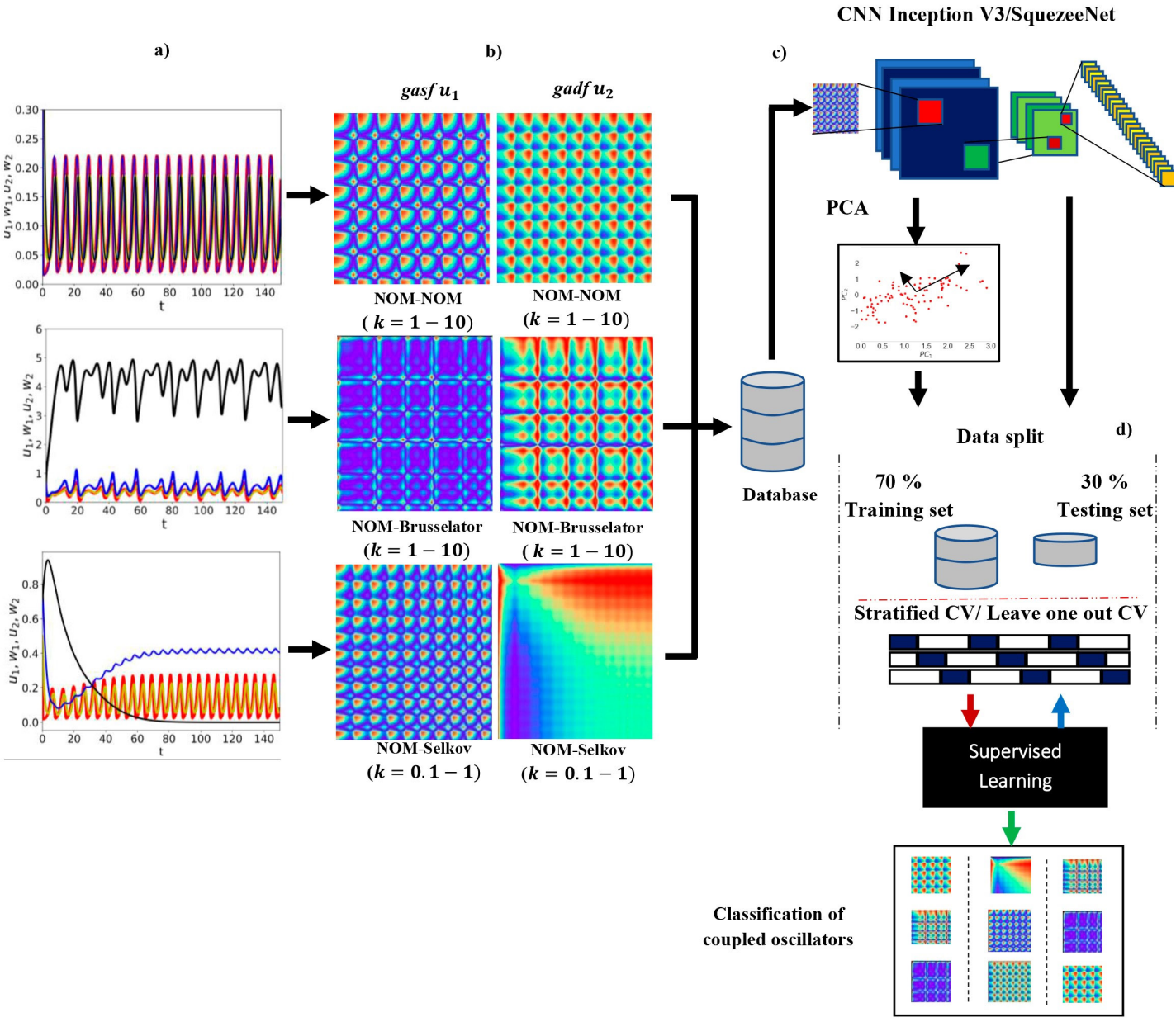

FIGURE 7. **General procedure to obtain the classification model of the type of coupled oscillators using the *gaf* images. a) The numerical solution of the coupled oscillator systems is obtained by setting the parameters of the models and varying the coupling parameter, b) subsequently *gaf* images are obtained from the time series of the numerical solution of the coupled oscillators, c) after building the database, then embedding the images using Google's CNN Inception V3 or SqueezeeNet and using PCA for dimension reduction (optional). Lastly, d) the classification model is evaluated using the techniques: stratified holdout (70% training set / 30% testing set), 3, 5, 10, 20-fold stratified cross-validation, and leave-one-out cross-validation.**

highest CA and F1 value for method A (CA= 0.983 and F1= 0.983) nevertheless, it also shows the best classification metrics for methods C, D, E and F (CA= 0.966 and F1= 0.967), while for method B, the SVM model presents the best classification metrics with a CA= 0.966 and F1= 0.966 (see supplementary material

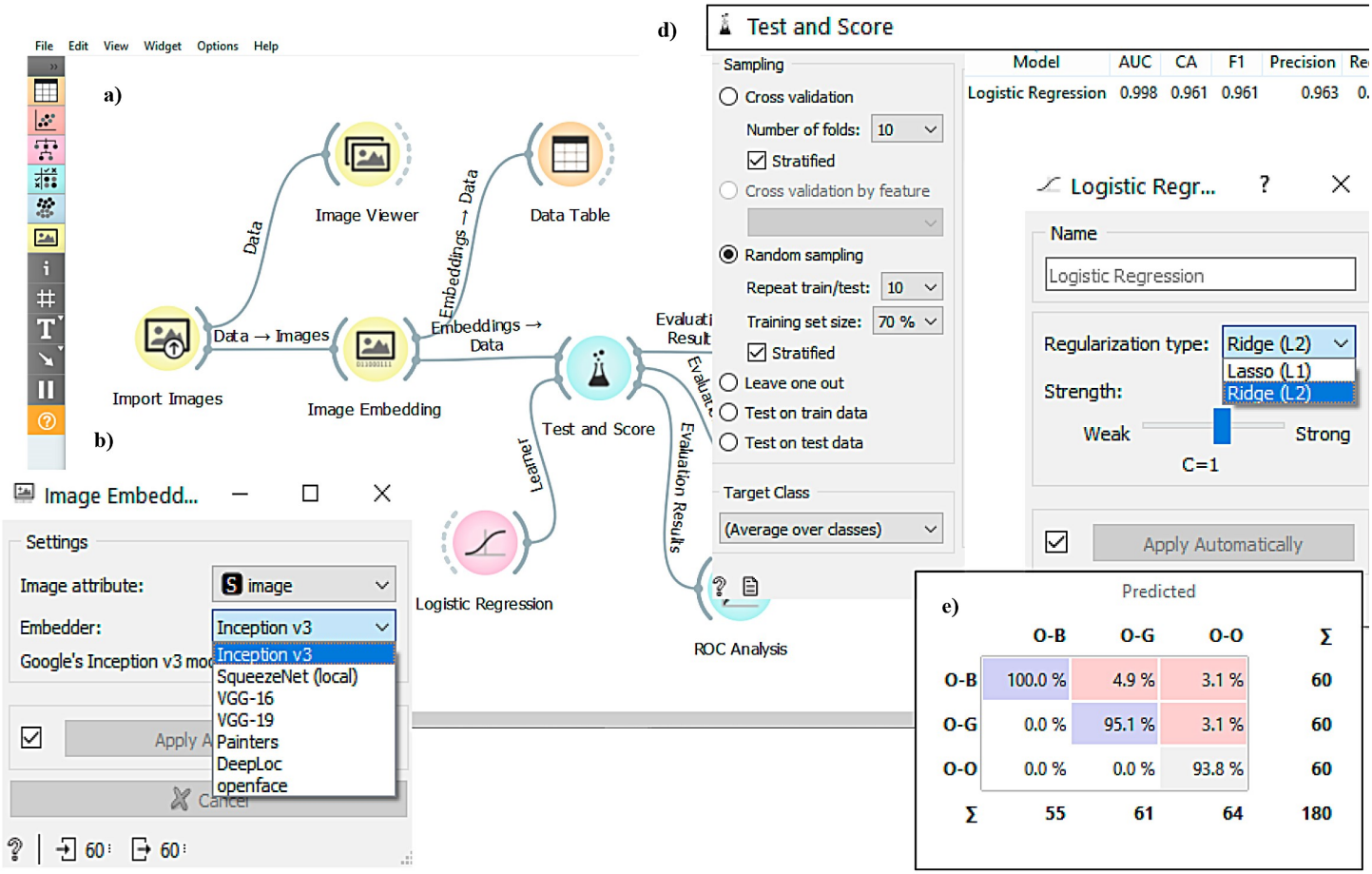

FIGURE 8. Orange workflow example for training the logistic regression model as a *gaf* image classifier. a) In the Orange interface, the images are imported first from a local folder using the "Import images" widget, then the images are embedded using the "Image embedding" widget and finally the training, validation and supervised learning model test. b) Window that shows the "Image Embedding" widget, which shows the CNNs that can be detected to extract the characteristics or descriptors of the images. The CNN of Google Inception V3 is shown by default. c) Window that shows the "Logistic Regression" widget. It is appreciated that it is possible to use the regularization of the sea Lasso (L1) or Ridge (L2). d) Window that shows the widget "Test and score." This widget shows the different evaluation techniques, which are: "k-fold cross-validation", "k-fold stratified cross-validation", "Random sampling", and "Leave-one-out cross-validation". Also, it shows the classification metric by class or average. e) Window that shows the "Confusion matrix" widget, which allows observing the confusion matrix of the supervised learning model. The widget allows displaying the confusion matrix in percentages or the number of images classified correctly and incorrectly.

Tables ST-2). Moreover, when a PCA is implemented after embedding with CNN Inception V3 using 21 main components, which explain 95% of the total variance, the logistic regression model shows the best classification metrics for the evaluation methods A, C, D, E and F, obtaining a value of CA= 0.961 and F1= 0.960 for method A, while for methods C, D, E and F, a CA= 0.950 and F1= 0.949 (see tables of supplementary material ST-2) were obtained. Regardless, the SVM model presents the highest values of CA and F1 for method B (CA= 0.966 and F1= 0.966). Having said that, it is possible to note that there are no major differences in the

classification metrics when using either the CNN SquezeeNet or the CNN Inception V3 to embed the images and, at the same time, there are no major differences in the metrics of classification when using the descriptors connected directly from CNN or when the main components are extracted from them. However, the computational time required for the evaluation of the models when using PCA is shorter. The supervised learning models present similar values in the classification metrics; nevertheless, the logistic regression model has the least complexity because it only uses one hyperparameter, which is used as a regularization or penalization [33] [67] [84] [85]. Therefore, logistic regression can be used as a classification model for the type of coupled oscillators. Table 2 shows the classification metrics for the logistic regression model for each of the evaluation methods, using descriptors obtained directly from CNN's as training data.

TABLE 2. Classification metrics for the logistic regression model using the characteristics obtained directly from the CNN for the evaluation.

Evaluation Technique	CNN							
	Inception V3				SquezeeNet			
A	CA	F1	P	R	CA	F1	P	R
B	0.961	0.961	0.963	0.961	0.983	0.983	0.984	0.983
C	0.950	0.949	0.953	0.950	0.966	0.967	0.969	0.966
D	0.950	0.949	0.953	0.950	0.966	0.967	0.969	0.966
E	0.950	0.949	0.953	0.950	0.983	0.983	0.984	0.983
F	0.950	0.949	0.953	0.950	0.983	0.983	0.984	0.983
A	0.950	0.949	0.953	0.950	0.983	0.983	0.984	0.983

Likewise, Table 3 shows the classification metrics for the same model, using the descriptors obtained from the PCA as training data. At this point, it is natural to ask what evaluation method should be used if all methods have similar ranking metrics. For this work, we chose method D because multiple experiments have been carried out that demonstrate that the best way to obtain high values in the metrics, be it classification or regression, is using stratified 10-fold cross-validation, even when there is the possibility of computation to increase fold number in the evaluation of supervised learning models [33] [86]. In addition, as can be seen in Tables 2 and 3, for method D the same values of the classification metrics are obtained using the descriptors extracted directly from CNN Inception V3 and those obtained from the implementation of the PCA (CA= 950, F1= 0.949-0.950) for training. When using the descriptors extracted directly from CNN SquezeeNet for training, the classification metrics CA= 0.983, and F1= 983 were obtained, while those obtained due to the implementation of the PCA are CA= 0.967 and F1= 0.967, which means that there is no significant difference. In conclusion, there are no major differences between the use of the descriptors extracted from the implementation of the PCA after embedding the images with one or the other CNN. This shows that the dimensions reduction does not substantially affect the precision of the supervised learning model and, conversely, allows for a better generalization of it [61].

TABLE 3. Classification metrics of the logistic regression model using the characteristics obtained from the application of the PCA.

Evaluation Technique	CNN							
	Inception V3 (21 PC, explained variance: 95%)				SquezeeNet (9 PC, explained variance: 95%)			
A	CA	F1	P	R	CA	F1	P	R
B	0.961	0.961	0.963	0.961	0.983	0.983	0.984	0.983
C	0.950	0.950	0.953	0.950	0.950	0.951	0.957	0.950
D	0.950	0.950	0.953	0.950	0.967	0.967	0.970	0.967
E	0.950	0.950	0.953	0.950	0.967	0.967	0.970	0.967
F	0.950	0.950	0.953	0.950	0.967	0.967	0.970	0.967
A	0.950	0.950	0.953	0.950	0.967	0.967	0.970	0.967

Figure 9 shows the confusion matrix of the logistic regression model trained with the descriptors obtained from applying the PCA after being embedded with CNN Inception V3 and using the evaluation method D. 18 of the 20 images of the coupling of the NOM and Brusselator Oscillators (O-B) have been correctly clas-

sified, while two images have been erroneously classified, one as a coupling between the NOM and Silkov (O-G) oscillators and another as a coupling between the identical NOM (O-O) oscillators. Furthermore, 19 of the O-G coupling images have been correctly classified, while one has been erroneously classified as O-O coupling. All O-O coupling images have been correctly classified.

Actual \ Predicted	O-B	O-G	O-O	Σ
O-B	18	1	1	20
O-G	0	19	1	20
O-O	0	0	20	20
Σ	18	20	22	60

FIGURE 9. Confusion matrix of the logistic regression method using the CNN Inception V3 as an image descriptor extractor and applying a reduction of dimensions using the PCA technique (21 PC, explained variance: 95%) (evaluation method D). It is observed that 18 of the 20 images of the O-B coupling have been classified correctly, while two have been erroneously classified, one as the O-G coupling and the other as the O-O coupling. On the other hand, the coupling shows that 19 of the 20 images of the O-G coupling have been correctly classified, while one has been classified as an O-O coupling. All images in the O-O coupling have been correctly classified.

Figure 10 shows the confusion matrix of the same model trained with the descriptors obtained from applying the PCA after being embedded with CNN SquezeeNet and using the evaluation method D. In the confusion matrix, it is possible to observe that 19 of the 20 images of the O-B coupling have been correctly classified, while one has been incorrectly classified as O-O coupling. Similarly, 1 of the 20 images of the O-G coupling has been incorrectly classified as O-O coupling. All images in the O-O coupling have been correctly classified. The decision to use one or the other CNN for embedding the images will depend on whether, as users, we want our images to be sent to an external server for embedding. For privacy and security reasons, we prefer them to be embedded locally [61].

Actual \ Predicted	O-B	O-G	O-O	Σ
O-B	19	0	1	20
O-G	0	19	1	20
O-O	0	0	20	20
Σ	19	19	22	60

FIGURE 10. Confusion matrix of the logistic regression method using as descriptor extractor of CNN SquezeeNet images and applying a reduction of dimensions using the PCA technique (9 PC, explained variance: 95%). It is observed that 19 of the 20 images of the O-B coupling have been correctly classified, while one has been classified as O-O coupling. While, 1 of the 20 images of the O-G coupling has been incorrectly classified as O-O coupling. All images in the O-O coupling have been classified correctly.

CONCLUSIONS

In the framework of Systems Biology, mathematical modeling of biochemical mechanisms involved in different physiological processes is of vital importance because it allows us to understand the non-linear dynamics that underlie these phenomena. This is why the use of mathematical tools and computational systems for the analysis of the complex feedback mechanisms present in living systems is necessary. The CNT is a mathematical tool that allows studying these mechanisms with a holistic approach and provides valuable information on each of the entities that make up the system [26] [87].

When determining the authority structural property of the complex network obtained from the BZ reaction mechanism proposed by Györgyi et al., and using it as the centrality criterion, the variables with the highest relevance were identified, i.e., those chemical species that have the greatest flow of information and that

could participate in the emergence of collective properties of the system. Identification of these variables led to the construction of a nonlinear system of differential equations similar to the reduction of the FKN model proposed by Field and Noyes (Oregonator) and which also explains the phenomenology of the BZ reaction. Hence, this result answers the question of using mathematical tools to reduce complex reaction mechanisms without losing generality. Therefore, it is possible to use this methodology in the study of nonlinear dynamics present in biochemical and physiological processes.

On top of that, by applying this methodology to biological systems, it is possible to translate any biochemical or physiological process to a mathematical model and study the phenomena of synchronization between different regulatory mechanisms [88] to decipher the complex dynamics that underlie living systems with a systemic approach.

The effect of coupling between oscillators of different nature can be clearly seen in the images obtained using the gaf technique, which can be used to train a supervised learning model to classify the type of coupled oscillators. The extraction of descriptors from gaf images through pre-trained CNNs (transfer learning) allows obtaining high precision values in the evaluation of different classification models; however, it is also possible to couple the pre-trained CNNs with the PCA to obtain high values in the classification metrics, comparable with the values of the metrics obtained by using only pre-trained CNNs as a descriptor extraction method. In particular, using the CNN's Inception V3 and SquezeeNet as extractors for descriptors of gaf images and obtaining the principal components of these descriptors, allows training classification models such as logistic regression and obtaining CA and F1-score values above 0.94 for different evaluation methods.

All things considered, the methodology proposed in this work can facilitate the determination of synchronization and desynchronization states in complex real biochemical and physiological mechanisms to recognize a possible correlation between these states and the emergence of different complex diseases.

AUTHOR CONTRIBUTIONS

J.A.A.F., carried out the theoretical-numerical calculation, J.F.R.R. and E.V.R. have supervised and reviewed all the calculations. All authors have contributed to the writing and corrections of the manuscript.

REFERENCES

[1] Draghici, S., Khatri, P., Tarca, A., Amin, K., Done, A., Voichita, C., Georgescu, C. and Romero, R. A systems biology approach for pathway level analysis. Genome Research. 2007;17(10):1537-1545. https://doi.org/10.1101/gr.6202607

[2] Chuang HY, Hofree M, Ideker T. A Decade of Systems Biology. Annual Review of Cell and Developmental Biology. 2010 Oct;26(1):721-44. https://doi.org/10.1146/annurev-cellbio-100109-104122

[3] Kell DB. Systems biology, metabolic modelling and metabolomics in drug discovery and development. Drug Discovery Today. 2006;11(23-24):1085-92. https://doi.org/10.1016/j.drudis.2006.10.004

[4] Emmert-Streib F, Dehmer M. Networks for systems biology: conceptual connection of data and function. IET Systems Biology. 2011 Jan;5(3):185-207. https://doi.org/10.1049/iet-syb.2010.0025

[5] Maeda YT, Sano M. Regulatory Dynamics of Synthetic Gene Networks with Positive Feedback. Journal of Molecular Biology. 2006;359(4):1107-24. https://doi.org/10.1016/j.jmb.2006.03.064

[6] Ferrell JE. Self-perpetuating states in signal transduction: positive feedback, double-negative feedback and bistability. Current Opinion in Cell Biology. 2002;14(2):140-8. https://doi.org/10.1016/S0955-0674(02)00314-9

[7] Mullur R, Liu Y-Y, Brent G. Thyroid Hormone Regulation of Metabolism. Physiological Reviews. 2014 Apr;94(2):355-382. https://doi.org/10.1152/physrev.00030.2013

[8] Porte D, Baskin DG, Schwartz MW. Leptin and Insulin Action in the Central Nervous System. Nutrition Reviews. 2002;60:S20-S29. https://doi.org/10.1301/002966402320634797

[9] Chen WW, Niepel M, Sorger PK. Classic and contemporary approaches to modeling biochemical reactions. Genes & Development. 2010;24(17):1861-75. https://doi.org/10.1101/gad.1945410

[10] Alves R, Antunes F, Salvador A. Tools for kinetic modeling of biochemical networks. Nature Biotechnology. 2006;24(6):667-672. https://doi.org/10.1038/nbt0606-667

[11] Radulescu O, Gorban AN, Zinovyev A, Noel V. Reduction of dynamical biochemical reactions networks in computational biology. Frontiers in Genetics. 2012;3:131. https://dx.doi.org/10.3389%2Ffgene.2012.00131

[12] Zhabotinsky AM. A history of chemical oscillations and waves. Chaos: An Interdisciplinary. Journal of Nonlinear Science. 1991;1(4):379-86. https://doi.org/10.1063/1.165848

[13] Sagues F, Epstein IR. Nonlinear Chemical Dynamics. Dalton Transactions. 2003;32(7):1201-1217. https://doi.org/10.1039/B210932H

[14] Epstein IR, Pojman JA, Steinbock O. Introduction: Self-organization in nonequilibrium chemical systems. Chaos: An Interdisciplinary Journal of Nonlinear Science. 2006;16(3):037101. https://doi.org/10.1063/1.2354477

[15] Noyes RM, Field R, Koros E. Oscillations in chemical systems. I. Detailed mechanism in a system showing temporal oscillations. Journal of the American Chemical Society. 1972;94(4):1394-5. https://doi.org/10.1021/ja00759a080

[16] Field RJ, Koros E, Noyes RM. Oscillations in chemical systems. II. Thorough analysis of temporal oscillation in the bromate-cerium-malonic acid system. Journal of the American Chemical Society. 1972;94(25):8649-64. https://doi.org/10.1021/ja00780a001

[17] Shanks, N. Modeling biological systems: the Belousov-Zhabotinsky reaction. Foundations of Chemistry. 2011; 3(1): 33-53.

[18] Field RJ, Noyes RM. Oscillations in chemical systems. IV. Limit cycle behavior in a model of a real chemical reaction. The Journal of Chemical Physics. 1974;60(5):1877-84. https://doi.org/10.1063/1.1681288

[19] Györgyi L, Turanyi T, Field RJ. Mechanistic details of the oscillatory Belousov-Zhabotinskii reaction. The Journal of Physical Chemistry. 1990;94(18):7162-70. https://doi.org/10.1021/j100381a039

[20] Sayama H. Introduction to the modeling and analysis of complex systems. New York: Open SUNY Textbooks, Milne Library, State University of New York at Geneseo; 2015. 478p.

[21] Lesne A. Complex Networks: from Graph Theory to Biology. Letters in Mathematical Physics. 2006;78(3):235-62. https://doi.org/10.1007/s11005-006-0123-1

[22] Mason O, Verwoerd M. Graph theory and networks in Biology. IET Systems Biology. 2007;1(2):89-119. https://doi.org/10.1049/iet-syb:20060038

[23] Albert R, Barabási A-L. Statistical mechanics of complex networks. Reviews of Modern Physics. 2002;74(1):47-97. https://doi.org/10.1103/RevModPhys.74.47

[24] Costa LDF, Rodrigues FA, Hilgetag CC, Kaiser M. Beyond the average: Detecting global singular nodes from local features in complex networks. EPL (Europhysics Letters). 2009;87(1):18008. https://doi.org/10.1209/0295-5075/87/18008

[25] Loscalzo J, Barabási Albert-László, Silverman EK. Network medicine: complex systems in human disease and therapeutics. Cambridge, MA: Harvard University Press; 2017. 448p.

[26] Costa LDF, Rodrigues FA, Cristino AS. Complex networks: the key to systems biology. Genetics and Molecular Biology. 2008;31(3):591-601. http://dx.doi.org/10.1590/S1415-47572008000400001

[27] Hornberg J, Bruggeman FJ, Westerhoff HV, Lankelma J. Cancer: A Systems Biology disease. Biosystems. 2006;83(2-3):81-90. https://doi.org/10.1016/j.biosystems.2005.05.014

[28] Cardon LR, Bell JI. Association study designs for complex diseases. Nature Reviews Genetics. 2001;2(2):91-99. https://doi.org/10.1038/35052543

[29] DeFronzo RA. Insulin Resistance, Hyperinsulinemia, and Coronary Artery Disease: A Complex Metabolic Web. Journal of Cardiovascular Pharmacology. 1992;20 (Suppl 1):S1-S16. https://doi.org/10.1097/00005344-199200111-00002

[30] Karalliedde J, Gnudi L. Diabetes mellitus, a complex and heterogeneous disease, and the role of insulin resistance as a determinant of diabetic kidney disease. Nephrology Dialysis Transplantation. 2016:31(2):206-13. https://doi.org/10.1093/ndt/gfu405

[31] Upadhyay SK. Chemical kinetics and reaction dynamics. New Delhi: Springer Netherlands; 2006. 256p. https://doi.org/10.1007/978-1-4020-4547-9

[32] Kotsiantis SB, Zaharakis ID, Pintelas PE. Machine learning: a review of classification and combining techniques. Artificial Intelligence Review. 2006;26:159-90. https://doi.org/10.1007/s10462-007-9052-3

[33] Berzal, F. Redes neuronales & deep learning. 1ra. ed. Granada, España: Edición Independiente; 2018. 753p.

[34] Bastian M, Heymann S, Jacomy M. Gephi: an open source software for exploring and manipulating networks. International AAAI Conference on Weblogs and Social Media. 2009;361-362.

[35] Moon FC. Chaotic and fractal dynamics: introduction for applied scientists and engineers. 2nd. ed. New York: Wiley; 1992. 528p.

[36] Afraimovich VS, Lin WW, Rulkov NF. Fractal dimension for poincaré recurrences as an indicator of synchronized chaotic regimes. International Journal of Bifurcation and Chaos. 2000;10(10):2323-2337. https://doi.org/10.1142/S0218127400001456

[37] Liu Z, Lai Y, Matías M. Universal scaling of Lyapunov exponents in coupled chaotic oscillators. Physical Review E. 2003;67(4): 045203. http://dx.doi.org/10.1103/PhysRevE.67.045203

[38] Porta A, Baselli G, Lombardi F, Montano N, Malliani A, Cerutti S. Conditional entropy approach for the evaluation of the coupling strength. Biological Cybernetics. 1999;81:119-129. https://doi.org/10.1007/s004220050549

[39] Eckmann, JP, Kamphorst SO, Ruelle D. Recurrence plots of dynamical systems. Europhysics Letter. 1987; 4(9):973-977. https://doi.org/10.1142/9789812833709_0030

[40] Hernández Sánchez S, Fernández Pozo R, Hernández Gómez LA. Deep Neural Networks for Driver Identification Using Accelerometer Signals from Smartphones. In: Abramowicz W, Corchuelo R. (eds) Business Information Systems. Lecture Notes in Business Information Processing. Switzerland: Springer, Cham; 2019, p. 206-220. https://doi.org/10.1007/978-3-030-20482-2_17

[41] Bode BW. Clinical Utility of the Continuous Glucose Monitoring System. Diabetes Technology & Therapeutics. 2000;2(Suppl 1):S35-41. https://doi.org/10.1089/15209150050214104

[42] Yoo EH, Lee SY. Glucose Biosensors: An Overview of Use in Clinical Practice. Sensors. 2010;10(5):4558-4576. https://doi.org/10.3390/s100504558

[43] Frost MC, Meyerhoff ME. Implantable chemical sensors for real-time clinical monitoring: progress and challenges. Current Opinion in Chemical Biology. 2002;6(5):633-641. https://doi.org/10.1016/s1367-5931(02)00371-x

[44] Frost MC, Meyerhoff ME. Real-Time Monitoring of Critical Care Analytes in the Bloodstream with Chemical Sensors: Progress and Challenges. Annual Review of Analytical Chemistry. 2015;8(1):171-192. https://doi.org/10.1146/annurev-anchem-071114-040443

[45] Coveney PV, Fowler PW. Modelling biological complexity: a physical scientist's perspective. Journal of The Royal Society Interface. 2005;2(4):267-280. https://doi.org/10.1098/rsif.2005.0045

[46] Kleinberg JM. Authoritative sources in a hyperlinked environment. Journal of the ACM. 1999;46(5): 604-632. https://doi.org/10.1145/324133.324140

[47] Aton SJ, Herzog ED. Come Together, Right...Now: Synchronization of Rhythms in a Mammalian Circadian Clock. Neuron. 2005;48(4): 531-534. https://dx.doi.org/10.1016%2Fj.neuron.2005.11.001

[48] Lorenzo González MN. Influencia del Ruido Gaussiano Correlacionado en la Sincronización de Sistemas Caóticos [Ph.D.'s thesis]. [Santiago de Compostela]:Universidad de Santiago de Compostela, 2000.161p. Spanish.

[49] Lefever R, Nicolis G, Borckmans P. The brusselator: it does oscillate all the same. Journal of the Chemical Society, Faraday Transactions 1: Physical Chemistry in Condensed Phases. 1988;84(4):1013-1023. https://doi.org/10.1039/F19888401013

[50] Vaidyanathan, S. Anti-synchronization of Brusselator chemical reaction systems via adaptive control. International Journal of ChemTech Research. 2015;8(6):759-68.

[51] Sel'kov EE. Self-Oscillations in glycolysis. 1. A Simple Kinetic Model. European Journal of Biochemistry. 1968;4(1):79-86. https://doi.org/10.1111/j.1432-1033.1968.tb00175.x

[52] Keener JP, Sneyd J. Mathematical physiology. 2nd. Ed. New York: Springer; 2009. 470p. https://doi.org/10.1007/978-0-387-75847-3

[53] Butcher J. Numerical methods for ordinary differential equations in the 20th century. In: Brezinski C, Wuytack, L. (eds). Numerical Analysis: Historical Developments in the 20th Century. Amsterdam: Elsevier; 2001.449-77p. https://doi.org/10.1016/B978-0-444-50617-7.50018-5

[54] Faouzi J, Janati H. pyts: A python package for time series classification. Journal of Machine Learning Research. 2020; 21(46):1–6.

[55] Wang Z, Oates T. Imaging time-series to improve classification and imputation. Proceedings of the 24th International Joint Conference on Artificial Intelligence. 2015;3939-45.

[56] Брагин, АВ, Bragin A, Спицын ВГ, Spicyn, V.Electroencephalogram Analysis Based on Gramian Angular Field Transformation. Proceedings of the 29th International Conference on Computer Graphics and Vision. 2019;2485:273-75. https://doi.org/10.30987/graphicon-2019-2-273-275

[57] Damaševičius R, Maskeliūnas R, Woźniak M, Polap D. Visualization of physiologic signals based on Hjorth parameters and Gramian Angular Fields. 2018 IEEE 16th World Symposium on Applied Machine Intelligence and Informatics (SAMI). 2018; 91-6. https://doi.org/10.1109/sami.2018.8323992

[58] Qin Z, Zhang Y, Meng S, Qin Z, Choo K-KR. Imaging and fusing time series for wearable sensor-based human activity recognition. Information Fusion. 2020;53:80-7. https://doi.org/10.1016/j.inffus.2019.06.014

[59] Demsar J, Curk T, Erjavec A, Gorup C, Hocevar T, Milutinovic M, Mozina M, Polajnar M, Toplak M, Staric A, Stajdohar M, Umek L, Zagar L, Zbontar J, Zitnik M, Zupan B. Orange: Data Mining Toolbox in Python. Journal of Machine Learning Research. 2013; 14(35): 2349−2353.

[60] Demšar J, Zupan B. Orange: Data Mining Fruitful and Fun- A Hystorical Perspective. Informatica 2013;37:55-60.

[61] Godec P, Pančur M, Ilenič N, Čopar A, Stražar M, Erjavec A, Pretnar A, Demšar J, Starič A, Toplak M, Žagar L, Hartman J, Wang H, Bellazzi R, Petrovič U, Garagna S, Zuccotti M, Park D, Shaulsky G, Zupan B. Democratized image analytics by visual programming through integration of deep models and small-scale machine learning. Nature Communications. 2019;10(1):4551. https://doi.org/10.1038/s41467-019-12397-x

[62] Weiss K, Khoshgoftaar T, Wang D. A survey of transfer learning. Journal of Big Data. 2016;3(1):1345-1359. https://doi.org/10.1186/s40537-016-0043-6

[63] Tan C, Sun F, Kong T, Zhang W, Yang C, Liu C. A survey on deep transfer learning. In Kůrková V, Manolopoulos Y, Hammer B, Iliadis L, Maglogiannis I. International conference on artificial neural networks. Rhodes: Springer International Publishing. Cham; 2018. p. 270-279. https://doi.org/10.1007/978-3-030-01424-7_27

[64] Szegedy C, Vanhoucke V, Ioffe S, Shlens J, Wojna Z. Rethinking the inception architecture for computer vision. 2016 IEEE Conference on Computer Vision and Pattern Recognition (CVPR); Las Vegas: IEEE; 2016. 2818-2826p. https://doi.org/10.1109/CVPR.2016.308

[65] Iandola FN, Han S, Moskewicz MW, Ashraf K, Dally WJ, Keutzer K. SqueezeNet: AlexNet-level accuracy with 50x fewer parameters and <0.5MB model size [Internet]. arXiv.org; 2020. Available from: *https://arxiv.org/abs/1602.07360*

[66] Simonyan K, Zisserman A. Very Deep Convolutional Networks for Large-Scale Image Recognition [Internet]. arXiv.org; 2020. Available from: *https://arxiv.org/abs/1409.1556v6*

[67] Almagro Armenteros JJ, Sønderby CK, Sønderby SK, Nielsen H, Winther O. DeepLoc: prediction of protein subcellular localization using deep learning. Bioinformatics. 2017;33(21):3387-3395. https://doi.org/10.1093/bioinformatics/btx431

[68] Müller AC, Guido S. Introduction to machine learning with Python a guide for data scientists. Beijing: OReilly; 2018. p. 251-303.

[69] Hawkins DM. The Problem of Overfitting. Journal of Chemical Information and Computer Sciences. 2004;44(1):1-12. https://doi.org/10.1021/ci0342472

[70] Sokolova M, Japkowicz N, Szpakowicz S. Beyond Accuracy, F-Score and ROC: A Family of Discriminant Measures for Performance Evaluation. In Sattar A, Kang B. (eds). AI 2006: Advances in Artificial Intelligence. Berlin: Springer; 2006. 1015-21p. https://doi.org/10.1007/11941439_114

[71] Pinto CMA, Mendes Lopes A, Tenreiro Machado JA. A review of power laws in real life phenomena. Communications in Nonlinear Science and Numerical Simulation. 2012;17(9):3558-78. https://doi.org/10.1016/j.cnsns.2012.01.013

[72] Gisiger T. Scale invariance in biology: coincidence or footprint of a universal mechanism? Biological Reviews of the Cambridge Philosophical Society. 2001;76(2):161-209. https://doi.org/10.1017/s1464793101005607

[73] Amemiya T, Kádár S, Kettunen P, Showalter K. Spiral Wave Formation in Three-Dimensional Excitable Media. Physical Review Letters. 1996;77(15):3244-7. https://doi.org/10.1103/physrevlett.77.3244

[74] Krug HJ, Pohlmann L, Kuhnert L. Analysis of the modified complete Oregonator accounting for oxygen sensitivity and photosensitivity of Belousov-Zhabotinskii systems. The Journal of Physical Chemistry. 1990;94(12):4862-6. https://doi.org/10.1021/j100375a021

[75] Ma J, Li F, Huang L, Jin W-Y. Complete synchronization, phase synchronization and parameters estimation in a realistic chaotic system. Communications in Nonlinear Science and Numerical Simulation. 2011;16(9):3770-3785. https://doi.org/10.1016/j.cnsns.2010.12.030

[76] Rajesh S, Sinha S, Sinha S. Synchronization in coupled cells with activator-inhibitor pathways. Physical Review E. 2007;75(1): 011906. https://doi.org/10.1103/physreve.75.011906

[77] Belykh I, Lange ED, Hasler M. Synchronization of Bursting Neurons: What Matters in the Network Topology. Physical Review Letters. 2005;94(18):1881011-1881014. https://doi.org/10.1103/physrevlett.94.188101

[78] Belhaq M, Houssni, M. Quasi-periodic oscillations, chaos and suppression of chaos in a nonlinear oscillator driven by parametric and external excitations. Nonlinear Dynamics. 1999;18(1):1-24. https://doi.org/10.1023/A%3A1008315706651

[79] Ng A. Feature selection, L 1 vs. L 2 regularization, and rotational invariance. In Brodley C (ed.). ICML '04: Proceedings of the twenty-first international conference on Machine learning. New York: Association for Computing Machinery; 2004. 78-86p. https://doi.org/10.1145/1015330.1015435

[80] Ng A. Preventing" overfitting" of cross-validation data. In Fisher DH (ed.). ICML '97: Proceedings of the Fourteenth International Conference on Machine Learning. San Francisco: Morgan Kaufmann Publishers Inc; 1997. 245-253p.

[81] Mao W, Mu X, Zheng Y, Yan G. Leave-one-out cross-validation-based model selection for multi-input multi-output support vector machine. Neural Computing and Applications. 2012;24(2):441-451. https://doi.org/10.1007/s00521-012-1234-5

[82] Grünauer A, Vincze M. Using Dimension Reduction to Improve the Classification of High-dimensional Data [Internet]. OAGM Workshop; 2020. Available from: *https://arxiv.org/pdf/1505.06907.pdf*

[83] Azure Machine Learning. Evitar el sobreajuste y los datos desequilibrados con el aprendizaje automático automatizado. Microsoft [Internet]. 2019. Available from: https://docs.microsoft.com/es-es/azure/machine-learning/concept-manage-ml-pitfalls

[84] Christodoulou E, Ma J, Collins GS, Steyerberg EW, Verbakel JY, Calster BV. A systematic review shows no performance benefit of machine learning over logistic regression for clinical prediction models. Journal of Clinical Epidemiology. 2019;110:12-22. https://doi.org/10.1016/j.jclinepi.2019.02.004

[85] Rajagopal S, Hareesha KS, Kundapur PP. Performance analysis of binary and multiclass models using azure machine learning. International Journal of Electrical and Computer Engineering (IJECE). 2020;10(1):978-986. http://doi.org/10.11591/ijece.v10i1.pp978-986

[86] Kohavi R. A study of cross-validation and bootstrap for accuracy estimation and model selection. IJCAI'95: Proceedings of the 14th international joint conference on Artificial intelligence. 1995;14(2):1137-1145

[87] Alducin Castillo J, Yanez Suárez O. Brust Carmona H. Electroencephalographic analysis of the functional conectivity in habituation by graphics theory. Revista Mexicana de Ingeniería Biomédica. 2016;37(3):181-200. https://doi.org/10.17488/RMIB.37.3.3

[88] Glass L. Synchronization and rhythmic processes in physiology. Nature. 2001;410(6825):277-84. https://doi.org/10.1038/35065745

TECHNICAL NOTE

Vol. 41 | No. 3 | **SEPTIEMBRE - DICIEMBRE 2020** | pp 28-39

REVISTA MEXICANA DE Ingeniería Biomédica

dx.doi.org/10.17488/RMIB.41.3.2

E-LOCATION ID: 1059

Set of Simulators of the Electrophysiology of the A-Type Potassium Current (I_A) in Neurons

Conjunto de Simuladores de la Electrofisiología de la Corriente de Potasio Tipo-A (I_A) en Neuronas

María Eugenia Pérez Bonilla, Marleni Reyes Monreal, Miguel Felipe Pérez Escalera, Arturo Reyes Lazalde

Benemérita Universidad Autónoma de Puebla

ABSTRACT

The A-type potassium current (I_A) participates in important brain functions, including neuronal excitability, synaptic integration, and regulation of action potential patterns and firing frequency. Based on the characterization of its electrophysiological properties by current and voltage clamp techniques, mathematical models have been developed that reproduce I_A function. For such models, it is necessary to numerically solve equations and utilize hardware with special speed and performance characteristics. Since specific software for studying I_A is not found on the Internet, the aim of this work was to develop a set of simulators grouped into three computer programs: (1) I_A Current, (2) I_A Constant-V Curves and (3) I_A AP Train. These simulators provide a virtual reproduction of experiments on neurons with the possibility of setting the current and voltage, which allows for the study of the electrophysiological and biophysical characteristics of I_A and its effect on the train of action potentials. The mathematical models employed were derived from the work of Connor *et al.*, giving rise to Hodgkin-Huxley type models. The programs were developed in Visual Basic® and the differential equation systems were simultaneously solved numerically. The resulting system represents a breakthrough in the ability to replicate I_A activity in neurons.

KEYWORDS: A-type potassium current; simulators; virtual experiments.

RESUMEN

La corriente de potasio tipo-A (I_A) tiene importantes funciones cerebrales como: excitabilidad neuronal, integración sináptica y regulación de patrones de potenciales de acción y la frecuencia de disparo. Sus propiedades electrofisiológicas se han caracterizado mediante técnicas de fijación de corriente y de voltaje. A partir de estos conocimientos se desarrollaron modelos matemáticos que reproducen su función. La cantidad de ecuaciones a resolver hace que se requiera de hardware con velocidad y potencia especiales. Un software específico para el estudio propio de la corriente I_A no se ha encontrado en Internet. En este trabajo se presenta un conjunto de simuladores agrupados en tres programas de cómputo: (1) Corriente I_A, (2) Curvas Constante-V y (3) Tren-I_A, que permiten reproducir los experimentos con técnicas de fijación de corriente y de voltaje para estudiar las características electrofisiológicas y biofísicas de la corriente I_A, e investigar el efecto que tiene en el tren de potenciales de acción. Los modelos matemáticos utilizados fueron derivados de los trabajos de Connor *et al*., dando origen a modelos tipo Hodgkin y Huxley. Los programas fueron desarrollados en Visual Basic®. Los sistemas de ecuaciones diferenciales fueron resueltos simultáneamente de forma numérica. Los programas desarrollados contribuyen a solucionar la carencia de este tipo de programas.

PALABRAS CLAVE: Corriente de potasio tipo-A; simuladores; experimentos virtuales.

Corresponding author

TO: Arturo Reyes Lazalde

INSTITUTION: Benemérita Universidad Autónoma de Puebla

ADDRESS: 15 Poniente #1102-A, Col. Álvaro Obregón, C. P. 74260, Atlixco, Puebla, México

E-MAIL: arturoreyeslazalde@gmail.com

Received:

9 May 2020

Accepted:

12 August 2020

INTRODUCTION

The teaching of life sciences is traditionally organized into two parts: theory and lab practice [1] [2]. At the undergraduate level, lab experiments to teach physiology and neurosciences are very expensive. Additionally, it is difficult to carry out experiments for intracellular recording with current and voltage clamp techniques. The need for space, expensive equipment, lab material and experimental animals for educational purposes is out of reach for most universities [3].

Diwakar et al. reported that in India an investment of around 20 million rupees (~267,900 USD) is required for a typical patch clamp configured for lab use, to which other costs such as the animals and facilities must be added [4]. In Mexico, the presence of up to 50 students in each classroom makes this kind of lab practice impossible. One feasible alternative is the development of simulators for teaching. Indeed, simulated patients already form part of the learning environment in different disciplines of the medical field [5] [6] [7] and virtual microscopy practices are employed in histology [8].

Teaching the basic principles of neuroscience is of special interest and can be greatly enhanced by incorporating realistic and interactive simulations of neuronal functioning [9]. Single-neuron computer simulations began with the work of Hodgkin and Huxley [10]. Several simulators are now available to realistically simulate neuronal networks, including GENESIS Simulation System [11], NEURON Simulation Environment [12] and NSL Neural Simulation Language. With the increasing capacity of computational performance, the simulation of the entire brain may ultimately be possible [13].

However, only a few neurosimulators have been adapted to a teaching environment. For example, Hernández and Zurek developed a module of teaching in NEURON, allowing students to examine the properties of biophysics in the axon by using the Hodgkin-Huxley model [14]. A simulator capable of reproducing the classic Hodgkin and Huxley experiments was developed by Reyes-Lazalde *et al.* [15]. The basic study of the passive properties of the axon and dendritic tree can be carried out with an interactive simulator developed for Windows® environment [16]. Brian, a program written in Phyton and found at *http://brian.di.ens.fr*, was developed for quickly coding models of spiking neuronal networks in everyday situations [17]. iCell, an interactive cell modeling tool located at *http://ssd1.bme.memphis.edu/icell/*, integrates research and education for electrophysiology training. It consists of JAVA applets that represent models of a variety of cardiac cells and neurons and provide simulation data on the bioelectric activity of a single cell [18].

Traditional learning media, such as multimedia-based demonstrations, videos, reading and lectures, are passive environments and therefore limit the interactive experience of students [3]. Contrarily, computer simulation enables active learning [3]. The requirements are a computer room, software and an instructor. Several reports have described the pedagogical value of simulators [4]. During a neuroscience course, a comparison was made between traditional teaching and active teaching aided by simulators, finding a greater understanding with the latter [3].

Ribarič and Kordaš tested the effectiveness of a software package for the study of cardiovascular physiology at the undergraduate level of a medical school. The software presented a new approach for teaching physiology, involving active learning and confronting students with multiple ways of simulating basic and clinical physiological phenomena [19]. Reyes-Lazalde *et al.* obtained favorable results when employing software for teaching science [20]. Hence, virtual labs have shown their utility for learning science [21].

During the current pandemic, teaching at a distance has added new relevance to information and communication technology (ICT). In this ICT-induced thrust, there are novel types of teacher-student interactions

and new pedagogical methods. Since all lab practices are now suspended, virtual labs provide an alternative. Due to the high costs of lab practices, the government of India has sponsored an initiative to develop virtual labs, including neurophysiology labs [4].

In the present work, simulators were developed for the teaching and learning of A-type potassium ion current in neurons. They will permit students to perform virtual experiments with a current and voltage clamp. With the help of an instructor, students will be able to appreciate the importance of the A-type potassium current (I_A) and how it modifies the train of action potentials (AP train), and discover other neuronal ion channels in addition to those described in the axon.

In 1961, Hagiwara *et al.* [22] recorded I_A for the first time in cells of the marine mollusk *Onchidium verruculatum* and identified it as a K^+ current. The activation and inactivation of the current produces a characteristic "A" profile, which is the reason for the name [23]. The equilibrium potential of I_A is similar to that of the delayed rectifier and is activated with hyperpolarization. The capacity of I_A to trigger action potentials and excitability in various neurons has been extensively studied. The function of I_A in the AP train is to decrease the firing frequency [24]. Gustafsson *et al.* [25] discovered the existence of I_A in CA3 neurons and found it to be decreased by 4-amonopyridine (4-AP), a convulsant, thus resulting in a marked increase in cellular excitability. In rat upper cervical ganglion neurons, I_A was characterized as being very rapidly activated at -60 mV potential, depending on the concentration of external K^+. This activation was reduced with 4-AP [26]. In neostriatal neurons, Bargas *et al.* [27] demonstrated that I_A is responsible for the delayed appearance of the action potential in response to near threshold depolarizing currents.

I_A has been simulated with the aid of specialized programming languages for neuroscience. For example, it was simulated on a typical laterodorsal tegmental neuron with NEURON software [28]. To examine the role of I_A in excitability, network synchronization and epilepsy, Fransén and Tigerholm adopted a modified version of the model by Migliore et al., downloaded from the ModelDB [29] [30] [31]. However, there is no education simulator, to our knowledge, for I_A (*http://senselab.med.yale.edu/senselab/modeldb/*).

The relevance of I_A is evidenced by its participation in several regulatory mechanisms in neurons. The electrophysiological data reported depends on the recording techniques involved [32].

The aim of the present study was to generate educational software to facilitate the teaching and learning of I_A current in undergraduate and graduate programs. A series of simulators were grouped into three computer programs: I_A Current, I_A Constant-V Curves and I_A AP Train. With electrophysiological techniques, they reproduce I_A and allow for an unlimited number of virtual experiments.

MATERIALS AND METHODS

Three interactive computer programs were designed and developed to study I_A: I_A Current, I_A Constant-V Curves and I_A AP Train. For this purpose, the Visual Basic 6.0 programming language for Windows® environment was adopted. The programs were compiled and made executable for Windows, from Windows 7 to Windows 10.

The programs act as simulators. To simulate a neuron, the Hodgkin-Huxley model [9] [10] [11] [12] [13] [14] [15] was employed (equations 1 and 2) and I_A was added in accordance with the model described by Connor *et al.* [24] (equations 3, 4, 5, 6 and 7).

$$C_m \, dV/dt = - \; I_{Na} - I_K - I_A - I_L \tag{1}$$

$$C_m \, dV/dt = - g_{Na} (V - E_{Na}) - g_K (V - E_K) - g_A (V - E_A) - g_L (V - E_L) \tag{2}$$

Where C_m is the membrane capacity per unit area (assumed constant), V is the membrane voltage, and g_{Na}, g_K, g_A and g_L are Na^+, K^+, I_A and leakage conductance, respectively. E_{Na}, E_K, E_A and E_L are the equilibrium potentials for Na^+, K^+, I_A and leakage, respectively. The equations utilized for Na^+, K^+ and leakage conductance and the corresponding velocities were those proposed by Hodgkin and Huxley [10], (see Hodgkin-Huxley equations for I_{Na}, I_K and I_L in Cronin [33] and Sterratt *et at.* [34]).

The equations for I_A are [24] [34]:

$$g_A = G_A\, a^3\, b \tag{3}$$

Where G_A is the maximum conductance of I_A, a is the activating particle and b is the inactivating particle [34].

The kinetics of the activation curves $a_\infty(V)$ and $b_\infty(V)$ (steady state) and time constants $\tau_a(V)$ and $\tau_b(V)$ are:

$$a_\infty = \{[0.0761 \exp(V+99.22 / 31.84)] / [1+ \exp(V+58.3 / 14.54)]\}^{1/3} \tag{4}$$

$$b_\infty = 1 / [1 + \exp(V+58.3 / 14.54)]^4 \tag{5}$$

$$\tau_a = 0.3632 + \{1.158 / [1 + \exp(V-60.96 / 20.12)]\} \tag{6}$$

$$\tau_b = 1.24 + \{2.678 / [1 + \exp(V-55 / 16.027)]\} \tag{7}$$

The parameters used in the model are: C_m = 1 μF cm^{-2}; E_{Na}, E_K, E_A and E_L = 50, -77, -80 and -22 mV, respectively; g_{Na}, g_K and g_L = 120, 20 and 0.3 mS cm^{-2}, respectively; g_A is variable, being selected by the simulators.

I_A Current program

The I_A Current program was designed to generate macroscopic traces for I_A during the voltage clamp technique. It is comprised of four simulators: (1) I_A Current Traces, (2) I_A Inactivation Protocol, (3) I_A Equilibrium Potential and (4) I_A Activation-Inactivation Plots.

The I_A Current Traces simulator, based on the mathematical model reported by Connor and Stevens [24] [35] [36] [37], reproduces the outward currents (I_A).

The I_A Equilibrium Potential simulator, also based on the Connor-Stevens model, examines the equilibrium potential for I_A.

The I_A Inactivation Protocol simulator involves adjusting the voltage holding (VH) to lower and lower negative potential levels before applying the stimulus pulse (voltage command, Vc). The kinetics of the decrease in the peak was derived with a mathematical fit from the experimental data of Connor and Stevens [35] [36] [37].

The I_A Activation-Inactivation Plots simulator consists of mathematical equations describing the rate constants [35] [36] [37], which were also obtained from the experimental data of Connor and Stevens. By employing these equations, the activation and inactivation currents of I_A can be portrayed.

I_A Constant-V Curves program

Based on the Hodgkin-Huxley model [10], this program replicates the voltage dependence of the speed constants.

I_A AP Train program

This program is designed to reproduce the action potentials of neurons with an inward sodium current (I_{Na}), an outward K^+ current (I_K) that does not inactivate (H-H type, Hodgkin and Huxley [10]), and an outward potassium current that inactivates (I_A) (equation 1).

To start the integration, a fourth-order Runge-Kutta method with a step time of dt = 0.01 was used. An algorithm written in basic to solve differential equations with this method is found in Zill [38].

Figure 1 illustrates the flow chart for the implementation of the models in Visual Basic®.

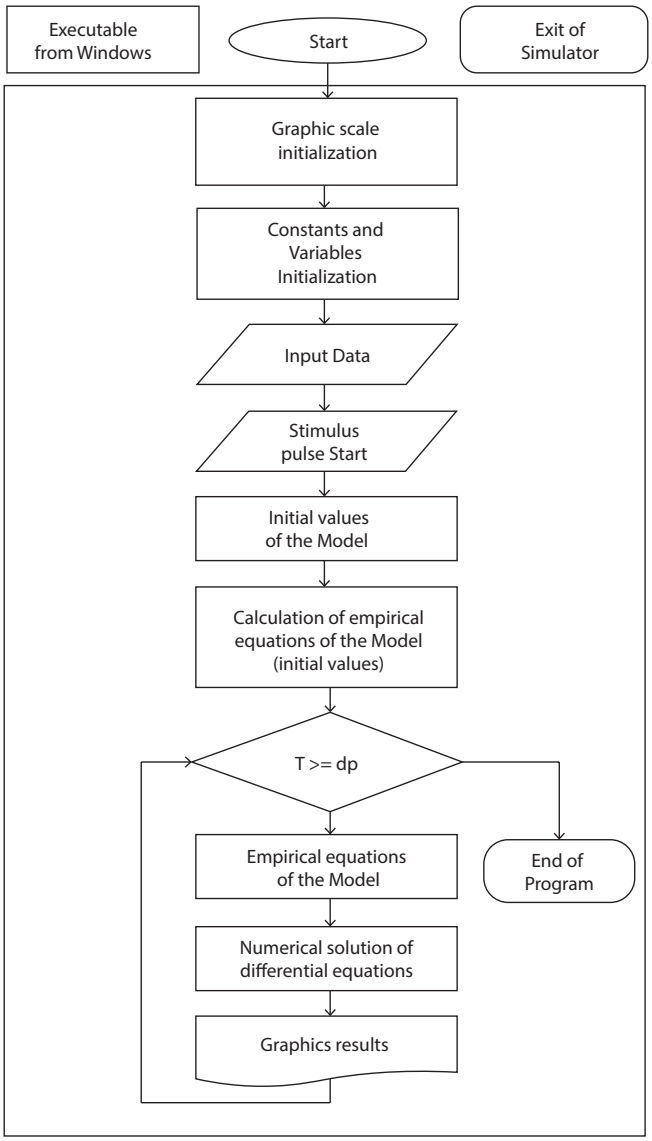

FIGURE 1. Flow chart for implementing the models. For each simulator, the values of the variables and the stimulus pulse are entered. The program initializes the graph scales and the basal values of the model. The differential equations are solved simultaneously, and the results are presented graphically. The iteration time depends on the duration of the stimulus (dp). The user can exit the simulator at any time.

RESULTS AND DISCUSSION

Three interactive computer programs (I_A Current, I_A Constant-V Curves and I_A AP Train) were designed and developed to reproduce the electrophysiology of I_A.

I_A Current program

A-type potassium current simulations

The user interface of the I_A Current simulator has two oscilloscope screens. One shows the macroscopic current traces of the I_A and the other illustrates the stimulus pulse in its voltage clamp mode.

The stimulus voltage to perform the simulations is in the range of -60 to -20 mV, with VH = -93 mV. In the neurons recorded by Connor and Stevens [36], the activation time constant has values from 10-25 ms and the inactivation constant from 220-600 ms. These values vary according to the type of cell. In neurons of the hippocampus of the vertebrate central nervous system, the values are considerably lower. Experimental values from other neurons can also be employed. To simulate and replicate the experimental results in distinct neuronal systems, the user need only enter the time constants of different neurons.

The simulation of the experiments published by Connor and Stevens [35] [36] is depicted in Figure 2.

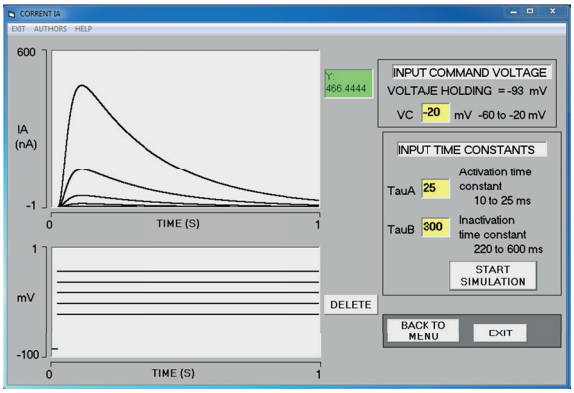

FIGURE 2. The simulation of the experiments carried out by Connor and Stevens were run to study the I_A. The voltage setting pulses are displayed on the lower oscilloscope screen. The upper screen portrays the currents traces corresponding to Vc = -60, -50, -40, -30 and -20 mV (the curves from baseline upwards). The VH was -93 mV and the rise time and decay current constants were 25 and 300 ms, respectively.

Command voltage pulses of -60, -50, -40 and -20 mV were applied. As the command voltage becomes less negative, the amplitude of the current increases [36]. The I_A trace corresponding to each of the stimulus pulses is displayed on the upper oscilloscope screen. For each simulation, the value entered for the time constant was 25 ms for activation and 300 ms for inactivation.

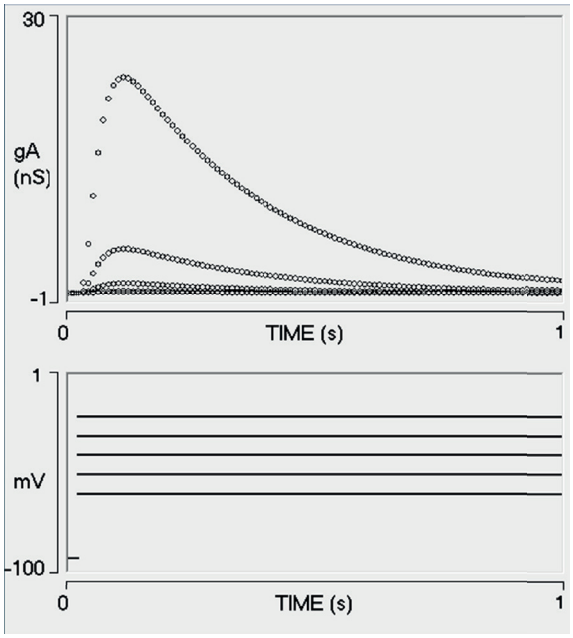

FIGURE 3. Simulations of gA with VH = -93 mV and pulses characterized by a voltage command of -60, -50, -40, -30 and -20 mV. The response is displayed on the upper oscilloscope screen. The trace with the smallest amplitude of conductance corresponds to -60 mV and the highest amplitude to -20 mV.

The simulations generate a classic I_A profile. This is a K^+ output current that starts at hyperpolarized potentials and shows an ascending curve during activation until reaching a maximum, at which point it gradually descends during inactivation. With a new command voltage and VH, there are changes in the channel conductance (g_A) and consequently in the current and peak amplitude of the current. The data correspond to experiments carried out at 5 °C. The currents are very slow in gastropod neurons compared to those in the brain of rats or other vertebrates. I_A is presented directly without considering the total outward potassium current and I_K.

I_A conductance (g_A) simulations

The channel conductance (g_A) is obtained by dividing I_A by the voltage command (V_c). Figure 3 shows the same simulation conditions as Figure 2. The upper oscilloscope screen depicts the g_A value in nS cm^{-2}. The trace duration is 1 s.

Simulation for I_A equilibrium potential

One of the methods to determine the equilibrium potential of an ionic current is to perform voltage clamp experiments and find the command voltage where the current is zero. In the I_A Equilibrium Potential simulator, the equilibrium for the current was -63 mV (Figure 4). The current-voltage relation is not presented.

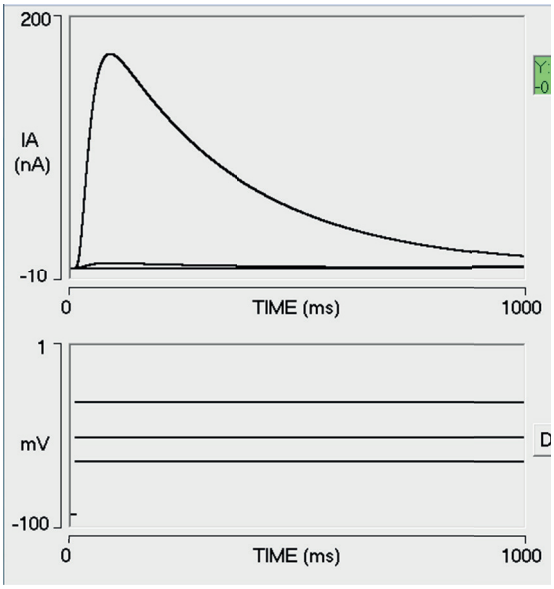

FIGURE 4. Simulation of the equilibrium potential. There was a lack of current at Vc = -63 mV. The upper lines correspond to Vc = -50 and -30 mV.

Inactivation protocol simulation

To simulate the inactivation protocol, the I_A Inactivation Protocol program is provided with the interface depicted in Figure 5. The two oscilloscope

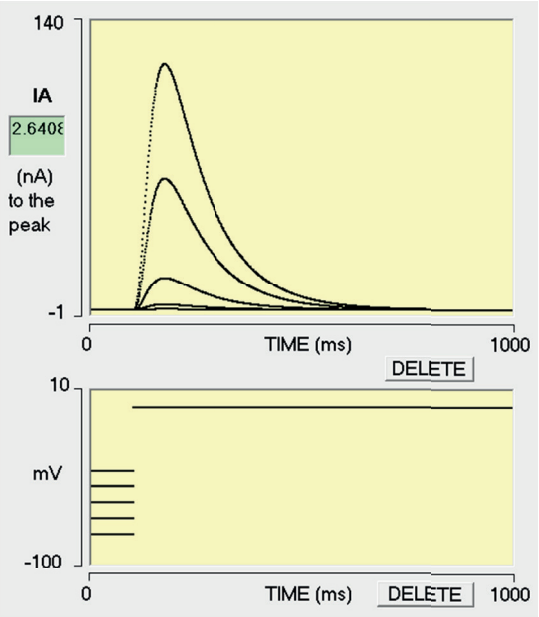

FIGURE 5. Simulations with the inactivation protocol. The voltage holding (VH) was applied at -80, -70, -60, -50 and -40 mV, consecutively. The responses are displayed on the upper oscilloscope screen. The amplitude of the trace was greatest at -80 mV and least (2.6 nA) at -50 mV.

screens on the left side show the current traces of I_A (upper) and the stimulation pulses (lower). The macroscopic I_A current is recorded in a neuron, beginning with a test depolarization at 0 mV and followed by the holding potential that varied from -90 to -50 mV.

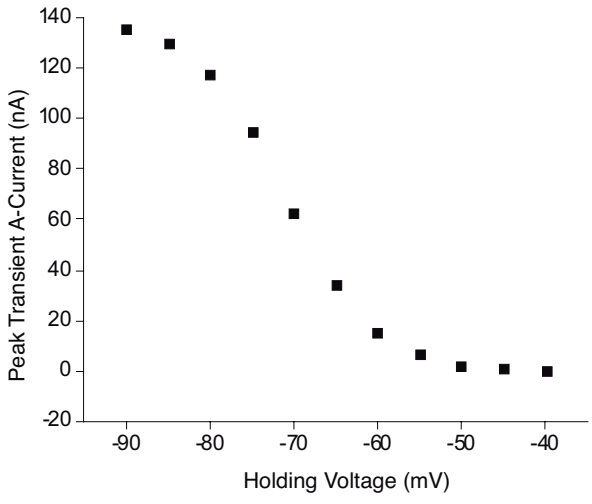

FIGURE 6. Inactivation plot. The peak value of the current decreases as the VH becomes less negative, from -90 to -40, in decremental steps of 5 mV. These results replicate the experimental data [36].

As can be appreciated, the peak value of the current decreases as the holding voltage preceding the stimulus pulse becomes less negative. Figure 6 illustrates how the decline in the peak value follows the pattern of a decreasing curve, as reported by Connor and Stevens [36]. The maximum value of I_A was obtained with a holding potential of -90 mV, and a value near zero was found in the range of -50 to -40 mV.

Simulation of the activation and inactivation curves

Simulations of the activation and inactivation curves are based on the Hodgkin-Huxley model [10]. Figure 7 shows an example of simulation. Curves a(V, ∞) and b(V, ∞) overlap between -30 and -20 mV.

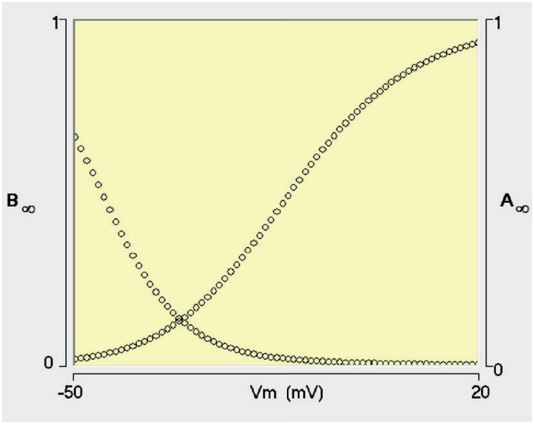

FIGURE 7. Simulation of activation and inactivation curves for the I_A. The decreasing curve corresponds to inactivation and the increasing curve to activation. As the membrane potential becomes less negative, its activation is greater. The simulation is in agreement with the results of Connor *et al.* [37].

I_A Constant-V Curves program

This program allows the user to observe the voltage dependence of the opening and closing speed constants for I_A. In the first simulation, the values entered were those reported for gastropod cells (Figure 8).

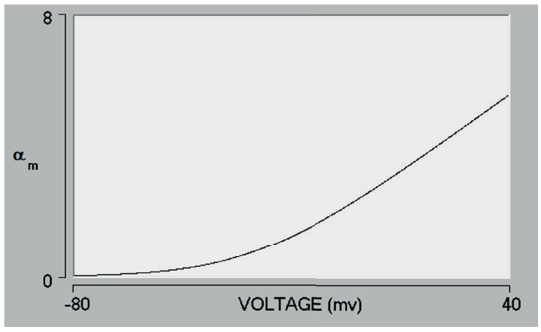

FIGURE 8. Simulation carried out to portray the kinetics of the velocity constant α_m with respect to the voltage.

I_A AP Train program

The Train I_A program simulates a neuron with the sum of the currents I_A, I_{Na} and I_K. It reproduces action potentials when the neuron is stimulated by a current pulse lasting from 50-200 ms at an intensity of 8 nA cm^{-2}. A test simulation to study the effect of I_A on the AP train is shown in Figure 9.

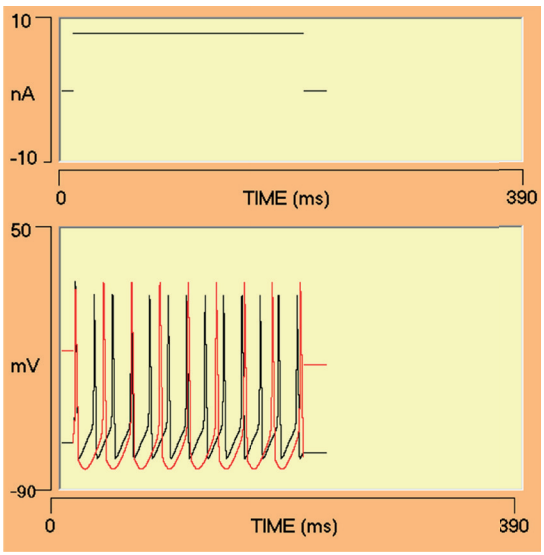

FIGURE 9. Simulation of the effect of I_A on the AP train. With g_A = 50 mS cm^{-2}, it is clearly observed how this current hyperpolarizes the neuron and decreases the AP frequency [39]. Control action potentials (utilizing Na^+ and K^+ channels) in black, I_A action potentials in red.

Two simulations were performed in a row with g_A set at 50 mS cm^{-2}. In the first, the AP was generated in a neuron with only Na^+ and K^+ channels (trace in black). In the second, the AP was triggered in a neuron that also has A-type potassium channels (red line). Note how the time between APs increases in the second. Hence, I_A delays the appearance of the AP and the frequency of the AP train decreases.

The overall model

A-type potassium channels are found in the neurons of mollusk and of the central and peripheral nervous system of mammals. The physiological implications of this type of channel reveal its importance for the appropriate functioning of neurons and the brain as a whole.

Programs for simulating I_A, such as NEURON and GENESIS, are freely accessible (*https://www.neuron.yale.edu/neuron/download*; *http://genesis-sim.org/*). For their proper use, however, it is necessary for the operator to undergo specialized training. Moreover, a high-speed, high-performance computer may be required, depending on the number of compartments simulated and the complexity of the model. Examples of special equipment with these specifications are a workstation or parallel supercomputer system.

Simulations of I_A have been carried out for research purposes. For example, Huguenard and McCornick [40] reported simulating I_A in the rhythmic oscillation of thalamic neurons.

Nevertheless, the tools employed imply considerable drawbacks for teaching purposes. They are very large and a substantial investment of time is required to learn how to manage them [15].

Due to the pandemic affecting us today and in the near future, online education has assumed increasing importance. The development of simulators with limited extension facilitates their usage, handling and transport. Furthermore, they can be easily adapted to remotely support teaching practices [15].

In the present work, a series of educational simulators were combined to reproduce the fundamental electrophysiology of I_A under experimental conditions of current and voltage clamp. The simulators were validated with the mathematical models developed by the experiments of Connor and Stevens [35] [36] [37]. The programs that group the simulators are compatible with on any personal computer having the minimum characteristics to run Windows® 7 to Windows® 10.

Thus, the software package developed presently will allow students to perform the experiments of Connor *et al.* [35] [36] [37]. The results and implications of I_A in the electrophysiology of the neuron can then be discussed with the instructor. The mathematical model currently employed for I_A was the one published by Connor *et al.* [24]. A description of the mathematical models proposed for I_A is found in Rush and Rinzel [39]. The numerical solution of differential equations enabled the reproduction of reported experimental data. Operation of the programs does not require specialized training. The user need only rely on scientific articles or on an instructor for an explanation of the biophysics and electrophysiology of I_A.

Since experiments involving organic tissue remain costly, despite efforts to decrease the cost of electrophysiological recording [32], simulators provide a practical alternative for study and research in neuroscience. They have the advantage of permitting changes in the biophysical factors of the neuron in order to observe their influence on neuronal functioning, a capacity not shared by experimental animal models. In the case of the model described herein, the simulators enable students and teachers to vary the conductance of the A-type potassium channel or the time constants for the generation and decline of I_A.

The development of simulators requires validation with experimental data. In regard to the simulators developed in the current investigation, real experimental values were entered for the variables, finding that the model reproduced the experimental results. Hence, the variables can be modified to analyze their consequences in a reliable model.

CONCLUSIONS

The three interactive computer programs described herein were able to replicate the biophysical characteristics of I_A and provide a virtual reproduction of the electrophysiological processes involved in activating and inactivating an ion current.

The corresponding oscilloscope screens showed voltage-dependent curves. The I_A AP Train program simulates the influence of I_A on an AP train, revealing how it decreases the AP trip frequency in the trace. With this simulator, the effect can be observed of increasing or decreasing g_A (channel conductance), modifying time constants, and altering the kinetics of the speed constants, among other phenomena. The simulators should be considered a teaching tool and do not replace the professor.

AUTHOR CONTRIBUTIONS

A.R.L. provided advice in neurosciences and programming, he was in charge in mathematical modeling and its numerical solution. M.E.P.B. provided advice in physiology and oversaw simulations and validation of the model. M.R.M. provided advice in education and oversaw programming, interface design and figures. M.F.P.E. oversaw the programming and compilation of the simulators. All authors participated in the structural analysis, review, and correction of the work.

REFERENCES

[1] Randall C, Burkholder T. Hands-on laboratory experience in teaching-learning physiology. Adv Physiol Educ. 1990;259(4):S4-7. https://doi.org/10.1152/advances.1990.259.6.S4

[2] Woodhull-McNeal AP. Project labs in physiology. Adv Physiol Educ. 1992;263(6):S29-32. https://doi.org/10.1152/advances.1992.263.6.S29

[3] Bish JP, Schleidt S. Effective use of computer simulations in an introductory neuroscience laboratory. J Undergrad Neurosci Educ. 2008;6(2):64-7.

[4] Diwakar S, Parasuram H, Medini C, Raman R, Nedungadi P, Wiertelak E, et al. Complementing Neurophysiology Education for Developing Countries via Cost-Effective Virtual Labs: Case studies and Classroom Scenarios. J Undergrad Neurosci Educ. 2014;12(2):130-9.

[5] Maran NJ, Glavin RJ. Low to high-fidelity simulation - A continuum of medical education? Med Educ Suppl. 2003;37(1):22-8. https://doi.org/10.1046/j.1365-2923.37.s1.9.x

[6] Oriol NE, Hayden EM, Joyal-Mowschenson J, Muret-Wagstaff S, Faux R, Gordon JA. Using immersive healthcare simulation for physiology education: Initial experience in high school, college, and graduate school curricula. Am J Physiol - Adv Physiol Educ. 2011;35(3):252-9. https://doi.org/10.1152/advan.00043.2011

[7] Harris DM, Ryan K, Rabuck C. Using a high-fidelity patient simulator with first-year medical students to facilitate learning of cardiovascular function curves. Am J Physiol - Adv Physiol Educ. 2012;36(3):213-9. https://doi.org/10.1152/advan.00058.2012

[8] Anyanwu GE, Agu AU, Anyaehie UB. Enhancing learning objectives by use of simple virtual microscopic slides in cellular physiology and histology: Impact and attitudes. Am J Physiol - Adv Physiol Educ. 2012;36(2):158-63. https://doi.org/10.1152/advan.00008.2012

[9] Av-Ron E, Byrne JH, Baxter DA. Teaching basic principles of neuroscience with computer simulations. J Undergrad Neurosci Educ. 2006;4(2):40-52.

[10] Hodgkin AL, Huxley AF. A quantitative description of membrane current and its application to conduction and excitation in Nerve. J Physiol. 1952;117(4):500-44. https://doi.org/10.1113/jphysiol.1952.sp004764

[11] Segev I. Temporal Interactions Between Post-Synaptic Potentials. In Bower J, Beeman D (eds.). The book of GENESIS, 2nd ed. New York: Springer-Verlag; 1998. 79-96p. https://doi.org/10.1007/978-1-4612-1634-6_6

[12] Carnevale NT, Hines ML. The NEURON Book. Cambridge: Cambridge University Press; 2006. 480 p.

[13] Izhikevich EM, Edelman GM. Large-scale model of mammalian thalamocortical systems. PNAS. 2008;105(9):3593-8. https://doi.org/10.1073/pnas.0712231105

[14] Hernández OE, Zurek EE. Teaching and learning the Hodgkin-Huxley model based on software developed in NEURON's programming language hoc. BMC Med Educ. 2013;13(70):1-9. https://doi.org/10.1186/1472-6920-13-70

[15] Reyes-Lazalde A, Reyes-Monreal M, Pérez-Bonilla ME. Desarrollo de un simulador de los experimentos clásicos y actualizados de fijación de Voltaje de Hodgkin y Huxley. Rev Mex Ing Biomed. 2016;37(2):135-48. https://doi.org/10.17488/rmib.37.2.1

[16] Reyes Lazalde A, Pérez-Bonilla ME, Funchs-Gómez OL, Reyes-Monreal M. Interactive simulators to study the passive properties of the axon and the dendritic tree. Rev Mex Ing Biomed [Internet]. 2012;33(1):29-40. Available from: http://www.rmib.mx/index.php/rmib/article/view/226

[17] Goodman D, Brette R. Brian: a simulator for spiking neural networks in Python. Front Neuroinform. 2008;2(NOV):1-10. https://doi.org/10.3389/neuro.11.005.2008

[18] Demir SS. Simulation-Based Training In Electrophysiology By iCELL. In 2005 IEEE Engineering in Medicine and Biology 27th Annual Conference. Shangai: IEEE-EMBS;2005:851-4. https://doi.org/10.1109/IEMBS.2005.1616549

[19] Ribarič S, Kordaš M. Teaching cardiovascular physiology with equivalent electronic circuits in a practically oriented teaching module. Am J Physiol - Adv Physiol Educ. 2011;35(2):149-60. https://doi.org/10.1152/advan.00072.2010

[20] Reyes Lazalde A, Reyes Monreal M, Pérez Bonilla ME. Experimentación virtual con el simulador dosis-respuesta como herramienta docente en biología. Apertura. 2016;8(2):22-37. http://dx.doi.org/10.32870/Ap.v8n2.855

[21] Vega OA, Londoño-Hincapié SM, Toro-Villa S. Laboratorios virtuales para la enseñanza de las ciencias. Informática. 2016;(35):97-110. https://doi.org/10.30554/ventanainform.35.1849.2016

[22] Hagiwara S, Kusano K, Saito N. Membrane changes of *Onchidium* nerve cell in potassium-rich media. J Physiol. 1961;155(3):470-89. https://doi.org/10.1113/jphysiol.1961.sp006640

[23] Cai S-Q, Li W, Sesti F. Multiple modes of A-type potassium current regulation. Curr Pharm Des. 2007;13(31):3178-84. https://doi.org/10.2174/138161207782341286

[24] Connor JA, Walter D, McKown R. Neural repetitive firing: modifications of the Hodgkin-Huxley axon suggested by experimental results from crustacean axons. Biophys J. 1977;18(1):81-102. https://dx.doi.org/10.1016%2FS0006-3495(77)85598-7

[25] Gustafsson B, Galvan M, Grafe P, Wigström H. A transient outward current in a mammalian central neurone blocked by 4-aminopyridine. Nature. 1982;299(5880):252-4. https://doi.org/10.1038/299252a0

[26] Galvan M, Sedlmeir C. Outward currents in voltage-clamped rat sympathetic neurones. J Physiol. 1984;356(1):115-33. https://doi.org/10.1113/jphysiol.1984.sp015456

[27] Bargas J, Galarraga E, Aceves J. An early outward conductance modulates the firing latency and frequency of neostriatal neurons of the rat brain. Exp Brain Res. 1989;75(1):146-56. https://doi.org/10.1007/BF00248538

[28] Sanchez RM, Surkis A, Leonard CS. Voltage-clamp analysis and computer simulation of a novel cesium- resistant a-current in guinea pig laterodorsal tegmental neurons. J Neurophysiol. 1998;79(6):3111-26. https://doi.org/10.1152/jn.1998.79.6.3111

[29] Fransén E, Tigerholm J. Role of A-type potassium currents in excitability, network synchronicity, and epilepsy. Hippocampus. 2010;20(7):877-87. https://doi.org/10.1002/hipo.20694

[30] Migliore M, Hoffman DA, Magee JC, Johnston D. Role of an A-type K^+ conductance in the back-propagation of action potentials in the dendrites of hippocampal pyramidal neurons. J Comput Neurosci. 1999;7(1):5-15. https://doi.org/10.1023/A:1008906225285

[31] Hines ML, Morse T, Migliore M, Carnevale NT, Shepherd GM. ModelDB: A Database to Support Computational Neuroscience. J Comput Neurosci. 2004;17(1):7-11. https://doi.org/10.1023/B:JCNS.0000023869.22017.2e

[32] Lemus-Aguilar I, Bargas J, Tecuapetla F, Galárraga E, Carrillo-Reid L. Diseño modular de instrumentación virtual para la manipulación y el análisis de señales electrofisiológicas. Rev Mex Ing Biomédica [Internet]. 2006;27(2):82-92. Available from: http://www.rmib.mx/index.php/rmib/article/view/359

[33] Cronin J. Mathematical Aspects of Hodgkin-Huxley Neural Theory. Cambridge: Cambridge University Press; 1987. 261p.

[34] Sterratt D, Graham B, Gillies A, Willshaw D. Principles of Computational Modelling in Neuroscience. Cambridge: Cambridge University Press; 2011. 300 p.

[35] Connor JA, Stevens CF. Inward and delayed outward membrane currents in isolated neural somata under voltage clamp. J Physiol. 1971;213(1):1-19. https://doi.org/10.1113/jphysiol.1971.sp009364

[36] Connor JA, Stevens CF. Voltage clamp studies of a transient outward membrane current in gastropod neural somata. J Physiol. 1971;213(1):21-30. https://doi.org/10.1113/jphysiol.1971.sp009365

[37] Connor JA, Stevens CF. Prediction of repetitive firing behaviour from voltage clamp data on an isolated neurone soma. J Physiol. 1971;213(1):31-53. https://doi.org/10.1113/jphysiol.1971.sp009366

[38] Zill DG. Ecuaciones diferenciales con aplicaciones. 2nd Ed. México: Grupo Editorial Iberoamérica; 1988. 516 p.

[39] Rush ME, Rinzel J. The potassium A-current, low firing rates and rebound excitation in Hodgkin-Huxley models. Bull Math Biol. 1995;57(6):899-929. https://doi.org/10.1007/BF02458299

[40] Huguenard JR, McCormick DA. Simulation of the currents involved in rhythmic oscillations in thalamic relay neurons. J Neurophysiol. 1992;68(4):1373-83. https://doi.org/10.1152/jn.1992.68.4.1373

COMPLEMENTARY MATERIAL

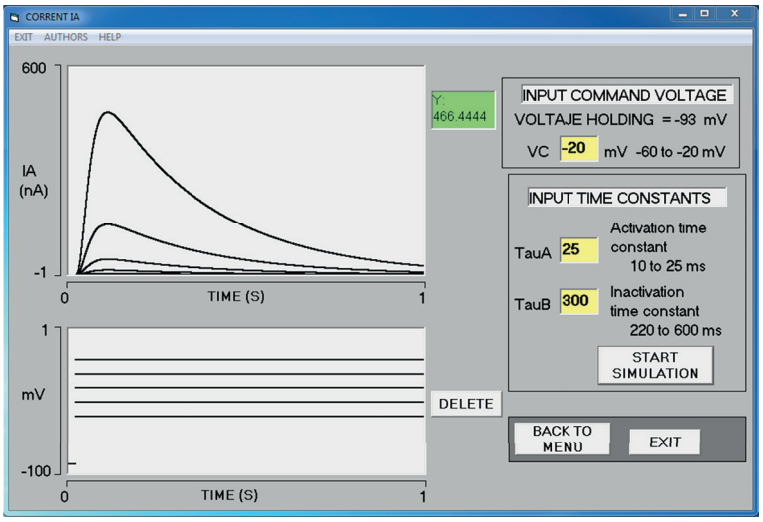

FIGURE 1. User interface of the I_A Current Traces simulator. The variable input module is shown on the right side: command voltage (-60 to -20 mV), activation time constant (10-25 ms) and inactivation time constant (220-600 ms). On the left side, the I_A macroscopic current is depicted on the upper monitorand the command voltage on the lower monitor.

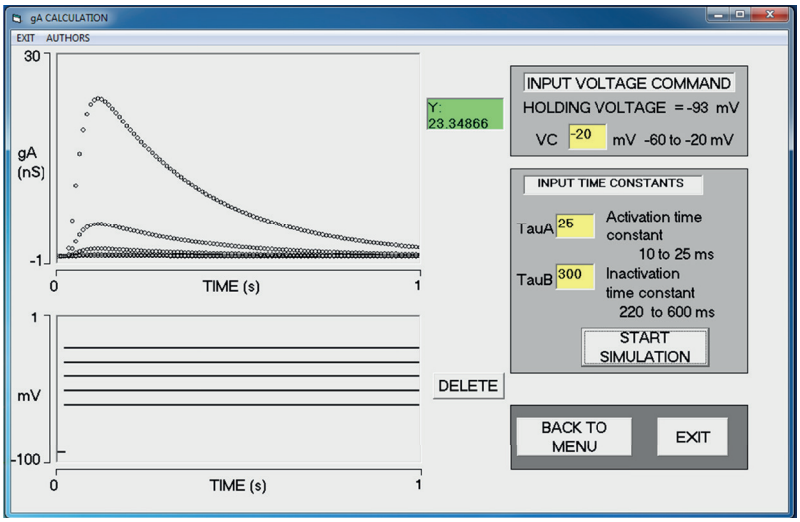

FIGURE 2. User interface for the g_A conductance simulation. The user enters the value of the variables and starts the simulation. The maximum amplitude of the conductance is measured with the cursor inside the upper monitor display and the value appears in the green box.

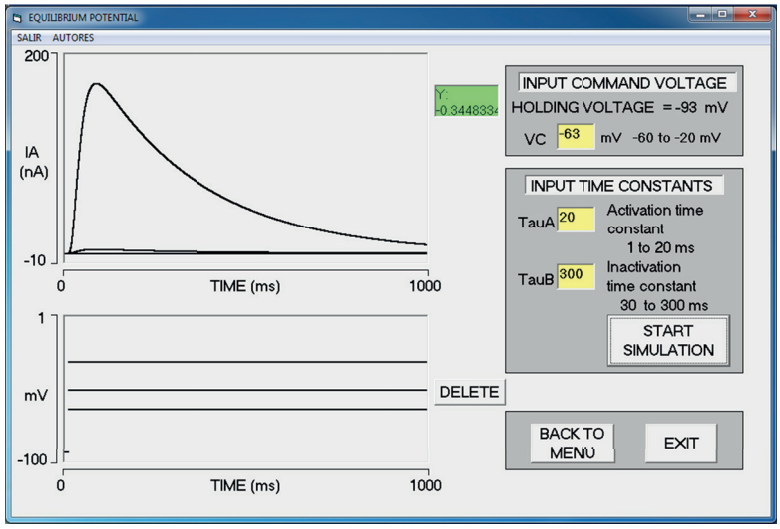

FIGURE 3. User interface of the I_A Equilibrium Potential simulator. The user enters the value of the time constants. Several simulations are performed with different values of the command voltage until the voltage that produces zero I_A current is found. The current is measured with the cursor and its value appears in the green box.

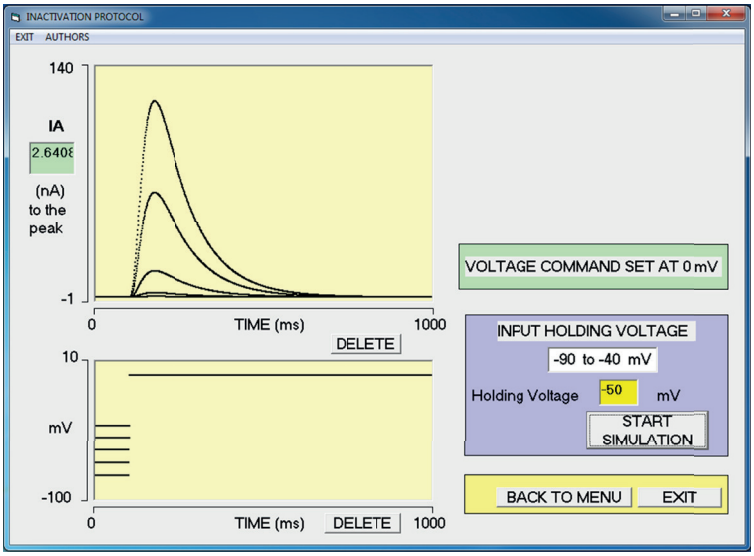

FIGURE 4. User interface of the I^A Inactivation Protocol simulator. Enter the holding voltage (prepulse) (-90 to -40 mV) on the right side. The macroscopic I_A current is displayed on the upper monitor. The peak value of the current appears in the green box. The stimulation protocol is shown on the bottom monitor.

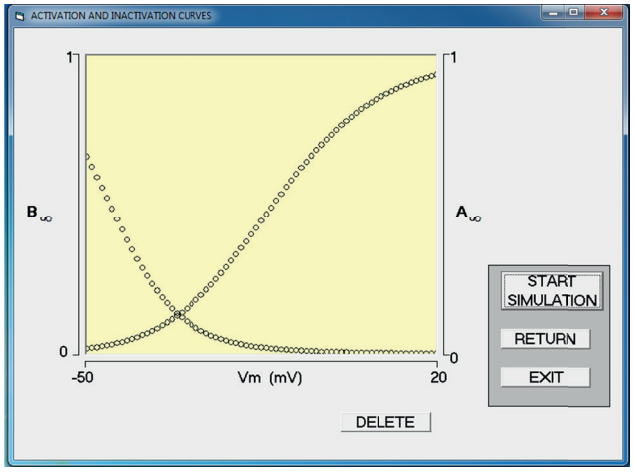

FIGURE 5. User interface of the I_A Activation-Inactivation Plots. The monitor portrays the activation curve (ascending trace) and the inactivation curve (descending trace).

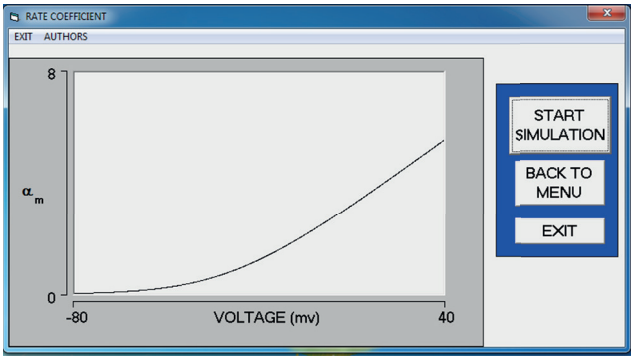

FIGURE 6. User interface of the I_A Constant-V Curves program. The monitor illustrates α_m.

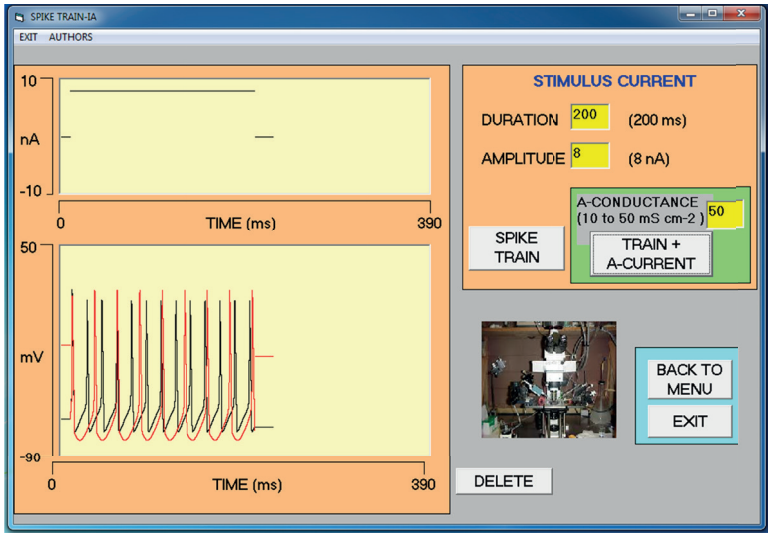

FIGURE 7. **User interface of the I_A AP Train program. The duration and amplitude of the stimulus current pulse and the value of conductance g_A (10-50 mS/cm^2) are entered on the right side. The stimulus pulse is depicted on the upper monitor and the train of action potentials on the lower monitor. The << Spike Train >> button produces the control simulation (black line). The << Train + A-Current >> button produces the simulation of a neuron that has type-A potassium channels (red line).**

RESEARCH ARTICLE

Vol. 41 | No. 3 | **SEPTIEMBRE - DICIEMBRE 2020** | pp 40-55

REVISTA MEXICANA DE Ingeniería Biomédica

dx.doi.org/10.17488/RMIB.41.3.3

E-LOCATION ID: 1050

Probabilistic Multiple Sclerosis Lesion Detection using Superpixels and Markov Random Fields

Detección Probabilística de Lesiones de Esclerosis Múltiple usando Superpixeles y Campos Aleatorios de Markov

Alejandro Reyes, Alfonso Alba, Martín O. Méndez, Edgar R. Arce-Santana, Ildefonso Rodríguez-Leyva

Universidad Autónoma de San Luis Potosí

ABSTRACT

Multiple Sclerosis (MS) is the most common neurodegenerative disease among young adults. Diagnosis and monitoring of MS is performed with T2-weighted or T2 FLAIR magnetic resonance imaging, where MS lesions appear as hyperintense spots in the white matter. In recent years, multiple algorithms have been proposed to detect these lesions with varying success rates, which greatly depend on the amount of a priori information required by each algorithm, such as the use of an atlas or the involvement of an expert to guide the segmentation process. In this work, a fully automatic method that does not rely on a priori anatomical information is proposed and evaluated. The proposed algorithm is based on an over-segmentation in superpixels and their classification by means of Gauss-Markov Measure Fields (GMMF). The main advantage of the over-segmentation is that it preserves the borders between tissues, while the GMMF classifier is robust to noise and computationally efficient. The proposed segmentation is then applied in two stages: first to segment the brain region and then to detect hyperintense spots within the brain. The proposed method is evaluated with synthetic images from BrainWeb, as well as real images from MS patients. The proposed method produces competitive results with respect to other algorithms in the state of the art, without requiring user assistance nor anatomical prior information.

KEYWORDS: Multiple Sclerosis; Lesion Detection; Superpixels; GMMF, Image Segmentation

RESUMEN

La Esclerosis Múltiple (MS) es una de las enfermedades neurodegenerativas más comunes en adultos jóvenes. El diagnóstico y su monitoreo se realiza generalmente mediante imágenes de resonancia magnética T2 o T2 FLAIR, donde se observan regiones hiperintensas relacionadas a lesiones cerebrales causadas por la MS. En años recientes, múltiples algoritmos han sido propuestos para detectar estas lesiones con diferentes tasas de éxito las cuales dependen en gran medida de la cantidad de información a priori que requiere cada algoritmo, como el uso de un atlas o el involucramiento de un experto que guíe el proceso de segmentación. En este trabajo, se propone un método automático independiente de información anatómica. El algoritmo propuesto está basado en una sobresegmentación en superpixeles y su clasificación mediante un proceso de Campos Aleatorios de Markov de Medidas Gaussianas (GMMF). La principal ventaja de la sobresegmentación es que preserva bordes entre tejidos, además que tiene un costo reducido en tiempo de ejecución, mientras que el clasificador GMMF es robusto a ruido y computacionalmente eficiente. La segmentación propuesta es aplicada en dos etapas: primero para segmentar el cerebro y después para detectar las lesiones en él. El método propuesto es evaluado usando imágenes sintéticas de BrainWeb, así como también imágenes reales de pacientes con MS. Con respecto a los resultados, el método propuesto muestra un desempeño competitivo respecto a otros métodos en el estado del arte, tomando en cuenta que éste no requiere de asistencia o información a priori.

PALABRAS CLAVE: Esclerosis Múltiple; Detección de Lesiones; Superpixeles; GMMF; Segmentación de Imágenes

Corresponding author

TO: Alfonso Alba

INSTITUTION: Universidad Autónoma de San Luis Potosí

ADDRESS: Facultad de Ciencias, UASLP.

Av. Chapultepec #1570, Col. Privadas del Pedregal,

C. P. 78295, San Luis Potosí, San Luis Potosí, México

E-MAIL: alfonso.alba@uaslp.mx

Received:

28 March 2020

Accepted:

23 August 2020

INTRODUCTION

Neurodegenerative diseases are one of the most critical issues for the health sector. Not only elderly people are the most affected by neurodegenerative diseases, but also young people can suffer from them. Multiple sclerosis (MS) is a neurodegenerative disease that mainly affects people between 20 and 40 years old, with high incidence in the general population. In fact, it is the second in incidence, epilepsy being the first [1]. The cause of MS is controversial but seems to depend on genetic and environmental factors and may also have a strong auto-immune component. The diagnosis and prognosis are well established nowadays by neurologists. The symptoms are described by the patient, and evidence is found through physical examination. In clinics, the neurologist verifies the symptoms of the patient (for example weakness, blurred vision, ataxia, etc.), and then requests a brain imaging study. Magnetic resonance imaging (MRI) is highly recommended in this case, with the most common protocols for this purpose being: T1-w, T2-w, Proton Density (PD) and Fluid Attenuated Inversion Recovery (FLAIR). In brain images, the neurologist manually annotates MS lesions, which in FLAIR images are shown as high-intensity spots on the white matter. It is important to mention that manual annotation and counting of hyper-intense spots is often an extensive and tedious process because the clinician needs to check dozens of images and may find several spots for a single patient. Hence, there is a large interest in designing algorithms that can automatically detect MS lesions or assist the expert during the process [2] [3]. In the past decades, various methods to segment MS lesions in MRI images have been published; however, some of these methods suffer from low accuracy or have such a large number of parameters to tune that they are not user-friendly. Other approaches rely heavily on the user's participation, or need atlas databases, requiring additional preprocessing time (for instance, to align the atlas with the input images). For these reasons, it is interesting to develop fully automatic and user-friendly methods to aid in the detection of MS lesions.

There are a few reviews of methods for MS lesion segmentation in the literature [4] [5]. Some of those methods are based on probabilistic approaches [6] [7], support vector machines (SVM) [8], region growing [9], K-Nearest Neighbors [10] or neural networks [11], while some methods may also use additional prior information such as atlases [12] or clinical information [13]. Many of these methods use pre-processing steps to prepare the input images for MS lesion detection, such as image denoising and non-uniformity correction. Also, since some non-brain tissues such as scalp and optic nerve are also shown with high intensity on T2-w images, a skull stripping step is often required; to this end, several methods use the Brain Extraction Tool (BET) [3]. Among the algorithms for MS lesion detection, several methods are based on Expectation-Maximization (EM) to segment MS lesions [14] [15] due to its good accuracy and easy implementation. In the EM-based method proposed by Garcia-Lorenzo *et al.* [15], the algorithm is divided in three steps. In the first and second steps, there is a non-uniformity correction of the input image, followed by a skull stripping process. Finally, in the last step, the MS lesion detection is applied using clinical rules to select potential regions with good results (reported Specificity of 0.9954). Another interesting method, which uses Markov Random Fields (MRF), is proposed by Khayati *et al.* [6] [7]. They developed an MS lesion detector by estimating a conditional probability density function for each class, which was trained using the adaptive mixtures method (AMM). For validating their results, in [6] they use a cross-validation approach where the first MS reader was used as the gold standard, leading to very accurate results since they achieved an average Dice Similarity Coefficient (DSC) of 0.75 [16] [17]. Other proposal was developed by Lao *et al.* [18], where they first perform affine registration of T1-w, T2-w PD and FLAIR images by maximization of the mutual information [19] and skull stripping based on affine registration using the BET algorithm [3]. In the training process, the proposed method combines T1-w, T2-w, PD and FLAIR in an

attribute vector (AV) for each voxel, along with the information of the neighboring voxels. A set of manually segmented scans is used to train a support vector machine (SVM) using the AdaBoost method [8] [20]; once trained, the SVM outputs, for each voxel, a scalar measure of abnormality that is binarized by applying a tuned threshold to discriminate lesions from normal tissue. Although similarity values (e.g., Dice index) were not reported, specificity and sensitivity look very promising which are also complemented by good visual results. Finally, in [21] the proposed method is based on Artificial Neural Networks (ANN), and the implemented software is freely available online at *https://med.inria.fr/the-app/downloads*. After selecting the segmentation option in this interface, the user can upload data and interactively click on the MS lesion to enhance them. One disadvantage of this software is that sometimes the algorithm segments the entire white matter region, particularly when MS lesions have blurred borders. Despite the diversity of algorithms for MS lesion detection, it is difficult to find one that fulfills the requirements of public health institutions, particularly when images are acquired with low resolution, few slices, and using a single modality to reduce costs. These requirements include border preservation, robustness to noise and blurred borders, good accuracy with single-modality (T2-w or T2-FLAIR) images, a reduced number of tuning parameters, and an implementation that does not rely on atlases or databases.

In this paper, a new method for automatic MS lesion segmentation is proposed. The method works with single-modality low resolution images, it does not need prior information related to anatomical structures or user annotations, and it only requires a few parameters to be tuned. In order to achieve good border preservation and robustness, an over-segmentation in superpixels (SPs) is performed as the first step [22], followed by a post-processing stage to achieve connectedness and eliminate spurious SPs produced by noise. Each SP is then classified by means of a Gauss-Markov Measure Field (GMMF) model [23]. This segmentation approach is applied twice: first to isolate the brain region, and a second time to segment MS lesions in the brain. This paper is organized as follows: Section 1 contains the introduction and a description of the goals of this work. Section 2 presents the details of the proposed segmentation algorithm, which is called SP-GMMF, and the methodology for MS lesion segmentation. Results from applying the proposed method to the analysis of synthetic and real MR images are shown in Section 3, with a comparison against a state-of-the-art algorithm based on Expectation Maximization (EM). Finally, the conclusions of this work are presented in Section 4.

MATERIALS AND METHODS

In this proposal, segmentation of MS lesions is achieved in two stages: the first stage is to isolate the region of interest (in this case, the brain) from the rest of the image (skull, meninges, or bone cavities); then, in the second stage, MS lesions within the brain region are detected. Each stage employs a segmentation algorithm. The segmentation method proposed here is a combination of an over-segmentation of the image in superpixels using the Simple Linear Iterative Clustering (SLIC) [22] and a probabilistic labeling of the superpixels by means of the GMMF [23]. Besides the main steps of the segmentation process, there are other pre and post-processing steps that are important for the efficiency of the proposed algorithm. The details of the complete algorithm are described below.

The SLIC method is a clustering algorithm that combines spatial location and intensity information to subdivide an image in a relatively small number of groups of pixels that have similar color and are spatially coherent, commonly called superpixels [22] [24] [25]. This algorithm is a variant of the k-means algorithm that uses a reduced search space to form each SP, and whose main advantages are high computational speed

and border-preserving SPs. The SLIC method works as follows: let us define $l(\vec{r})$ as the image over the lattice L (that is, $l(r) \in L$), and each superpixel is defined as $S_k = [C_k, D_k]$ where C_k and D_k are the average intensity and the geometric center of the superpixel, respectively. Indexes of superpixels are denoted by k, that is $k = 1, 2, \ldots, K$, with K as the number of superpixels over L. The initialization of each D_k is given by a regular hexagonal grid in L, and C_k as the intensity at pixel site C_k. For each superpixel S_k, a square neighborhood of size $2M \times 2M$ is defined with center at D_k and $M = \sqrt{|L|/K'}$, where K' is the desired number of SPs given by the user; as a rule of thumb, this parameter can be defined as the total number of pixels in the image divided by the area (in pixels) of the smallest lesion that is observed; for instance, we are using $K' = 3000$ SPs for all images in this study. The actual number of superpixels K will vary across all the steps in the algorithm. Only those pixels that belong to the neighborhood of D_k can be assigned to S_k according to the distance measure:

$$\delta_k(\vec{r}) = \sqrt{m^{-2}\left(C_k - l(\vec{r})\right)^2 + \left(\frac{\gamma^2}{M^2}\right)\|D_k - \vec{r}\|^2} \quad (1)$$

where the first term measures the intensity distance, and it is normalized by the dynamic range of the data m, which can be computed as $m = max\ (l\ (\vec{r})) - min\ (l\ (\vec{r}))$. The second term is the spatial distance term and it is normalized by the size of the neighborhood. Finally, γ is a hyperparameter that weighs the importance between both terms. Once every pixel is assigned to some S_k, C_k and D_k are updated with the average intensity and spatial position of the pixels that belong to the k-th SP, and δ_k is computed again; this process is iterated until convergence. In our experience, the algorithm converges in 5 to 10 iterations. Although SPs adhere well to borders, for an adequate choice of γ, the SLIC algorithm can sometimes produce fragmented superpixels, which may lead to unconventional neighborhoods for the Markovian Fields process [23]. For that reason, a relabeling process by means of connected component algorithm is applied [26], so that each connected fragment of a fragmented SP is considered as a new, individual superpixel. Once the relabeled field has been obtained, small SPs which are often due to noise, are fused to the most similar (in terms of average intensity) neighboring superpixel. In our case, a superpixel is considered too small when its area is less that 3% of the SP average area M^2; the 3% threshold was found experimentally as the percentage for which the number of SPs after fusion approximates better the number of desired SPs K'. With this fusion, not only the number of variables, but also the noise was reduced. Once the SPs are obtained, the next step for the segmentation process is to classify them with respect to their intensity. For that purpose, we consider that each class is defined by a Gaussian distribution of pixel intensities with a given mean and variance. Note that, although we aim for a binary classification at each stage (brain vs non-brain in the first stage, lesion vs non-lesion in the second stage), there are several types of tissues represented in the images; for this reason, multiple classes must be considered using the GMMF model [23], the goal is to estimate, for each SP S_k, the probability $p_j(S_k)$ that it belongs to class j, for each $j = 1, \ldots, C$, where C is the number of classes. Under this model, one can obtain the probability field for each class j by minimizing the following energy function U given by:

$$U(p_j) = \sum_{k=1}^{K}\left(p_j(k) - g_j(k)\right)^2 + \lambda \sum_{k=1}^{K}\sum_{i \in S_k}\left(p_j(k) - p_j(i)\right)^2 \quad (2)$$

where the first term is a data term which enforces $p_j(k)$ to be similar to the normalized likelihood between the k-th superpixel and the j-th class, which is given by $g_j(k) = (v_j(k))/\sum_i v_i(k)$, where $v_j(k)$ is a likelihood function which measures how well the k-th SP fits in class j. Assuming that classes follow a Gaussian distribution, the likelihood can be obtained as:

$$v_j(k) = \frac{1}{\sqrt{2\pi}\,\sigma_j} \exp\left\{-\kappa\left(C_k - \mu_j\right)^2 / 2\sigma_j^2\right\} \quad (3)$$

where μ_j and σ_j are the mean and variance of the j-th class, respectively. Notice that the μ can be automatically initialized by the k-means method. Additionally, there is a hyper-parameter κ which controls the overall variance of all classes. The second term is a regularization term that promotes the similarity in the neighborhood. The neighborhood N_k for the k-th superpixel can be obtained, first, inspecting the borders of the image of superpixel labels and then inspecting the image of labels; i.e., when a border is detected, the labels in that point (SP) are added to its SP neighborhood. Finally, λ is a hyper-parameter that weighs the importance between terms. To solve (2), one can calculate its derivative and equal it to zero to obtain a linear equation system, which can be iteratively solved by the Gauss-Seidel method where the solution of p_j (k) is given by:

$$p_j(k) = \frac{g_j(k) - \lambda \sum_{i \in N_k} p_j(i)}{1 + \lambda |N_k|} \quad (4)$$

After each Gauss-Seidel iteration, the means and variances of all classes are updated with a forgetting factor α = 0.2 (i.e. $\mu_t \rightarrow (1\text{-}\alpha)\ \mu_{t\text{-}1} + \alpha\mu_t$, where t is the current iteration). This method generally stops until convergence is obtained, but in our experience, it converges from 5 to 10 iterations. Once convergence is achieved, each superpixel S_k is assigned to the class given by: $c(S_k) = \arg\max_j p_j(k)$. Figure 1 shows the flow chart of the SP-GMMF Segmentation proposal.

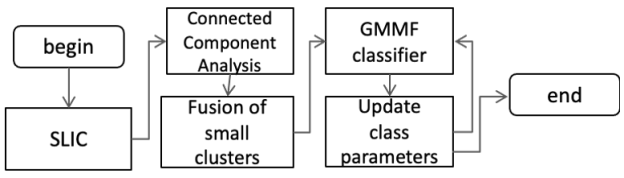

FIGURE 1. **Block diagram of the proposed method SP-GMMF.**

MS Lesion Classification

The SP-GMMF segmentation proposal takes advantages from SLIC and GMMF methods to implement a general-purpose segmentation method. In the proposed two-stage algorithm for MS lesion detection, which is illustrated in Figure 2, the first stage is oriented to automatically isolate the parenchyma region from the rest of the image. For that purpose, this proposal takes the SP-GMMF segmentation $c(S_k)$ of a T2-weighted or T2-FLAIR MR brain image (Figures 2a and 2b) to obtain a binary mask that represents the isolated brain. The fusion of small superpixels into bigger ones is depicted in Figure 2c, where some of the smaller SPs (circled in green) were fused with a neighboring larger SP, and the final segmentation is shown in Figure 2d.

It is well known that in several slices of an MRI sequence, the brain region and the background have the largest regions in almost every MRI slice. Under this assumption and knowing that the background has the lowest intensity in the MRI image, the brain mask will be obtained by choosing the largest area that does not belong to the lowest-intensity class. Notice that, in the case of the axial images, this does not always occur because the hemispheres might appear disconnected from each other. For example, in some supratentorial MRI Axial images the ratio of areas between hemispheres will be closest to one because their areas are similar (i.e. a ratio threshold above 0.7 may indicate that areas are similar). On the other hand, in some supratentorial and most infratentorial MRI images where the hemispheres are joined into a single region, the next largest region will be another structure whose area will be significantly smaller than the largest one (with a ratio less than 0.7), and thus the algorithm will consider it as part of the brain. Once the brain area mask has been obtained, a hole-filling algorithm is applied to it in order to recover any dark structure within the brain that might have been discarded by the previous operation.

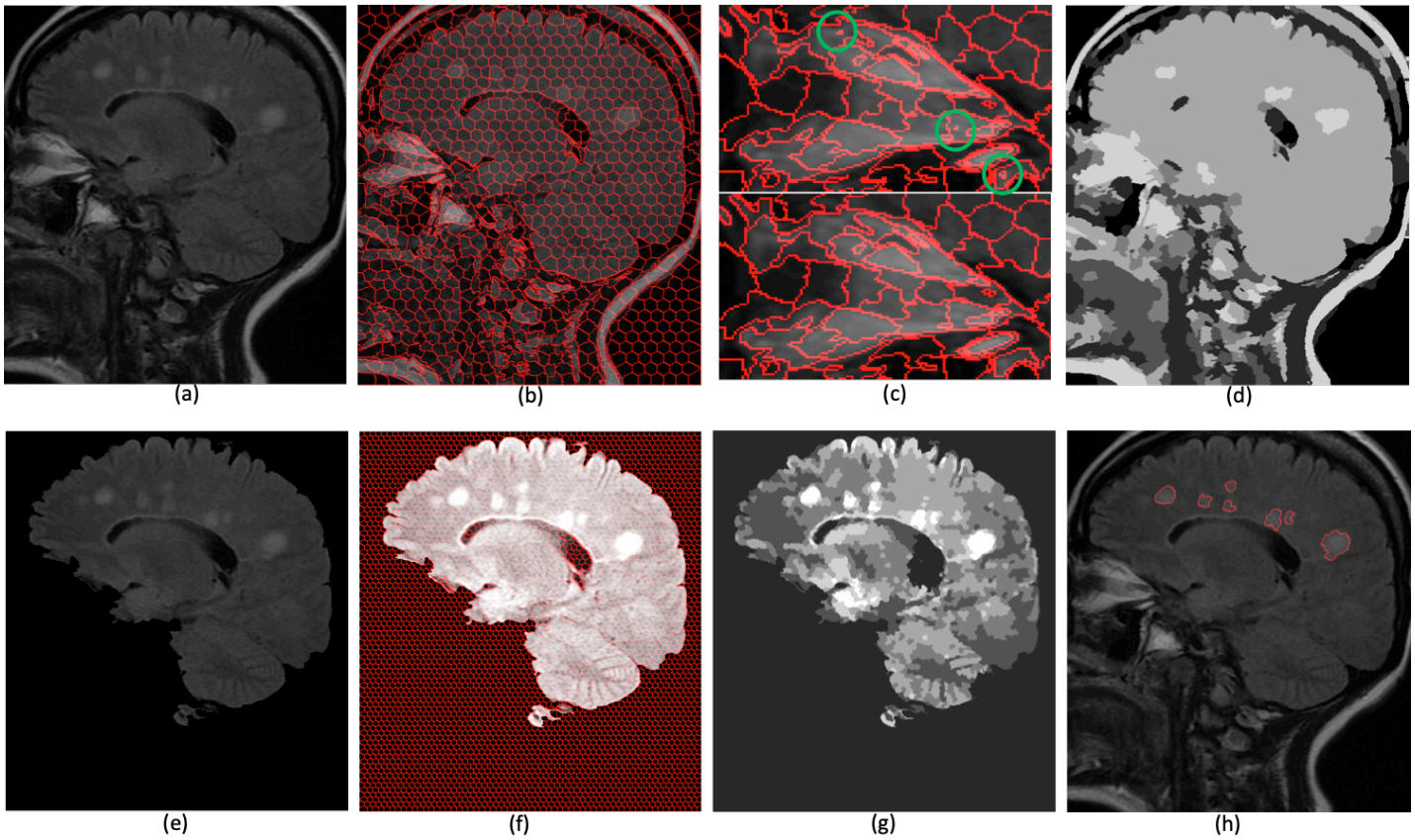

FIGURE 2. Complete process for detection of lesions in the brain. (a) Sagittal MRI input image of 520x459 pixels, (b) image segmented in superpixels with γ = 0.1 and 1000 desired clusters (resulting in K = 972 clusters), (c) Zoomed region where small clusters are shown circled in green (top), result of the fusion process where small regions were merged (bottom), (d) Result of GMMF segmentation with 10 iterations, λ = 0.1 and k = 0.1, (e) Isolated brain area, (f) Segmentation of the intensity-adjusted brain region in 5000 super-pixels, resulting in K = 5453 clusters after connected component were found, (g) GMMF segmentation of the brain region, (h) final result detecting 7 lesions in the white matter with eccentricity less than 0.9 and area of at least 80.

This mask, applied to the MRI image, automatically isolates the brain for the rest of the image (Figure 2e). On the other hand, MS lesions appear in T2 images as hyperintense spots; for this reason, an intermediate step is to apply a contrast-enhancing intensity adjustment to the isolated brain image to saturate the hyperintensities. This operation scales the voxel intensities by a factor such that the lowest 3% percentile will be saturated to zero, and the highest 3% percentile will be saturated to 255 (in an 8-bit grayscale image), which will facilitate the MS lesion detection for the next segmentation procedure.

In the second stage, the SP-GMMF segmentation is applied to the intensity adjusted brain image with a finer resolution of the SPs; that is, a larger desired number of SPs K' (Figures 2f and 2g). To obtain the binary mask that contains the MS lesions, the algorithm now isolates the regions that correspond to the highest intensity class on the segmentation and labels them using a connected component analysis, from which the area and eccentricity of each spot can be also obtained, as well as the number of potential lesions found in the image. Finally, a filtering procedure designed to reduce the number of false-positives

is applied, in which hyper-intense spots are reported as MS lesions (Figure 2g) only if they fulfill the following criteria: they must not be located in the external border of the brain (which corresponds to gray matter), their area must be sufficiently large (approximately 30 pixels) and they must not to be too eccentric (maximum eccentricity of 0.85).

Roughly speaking, each stage of the process performs a binary segmentation of the image: in the first stage (brain peeling) the interest is to distinguish between background/non-background pixels, whereas in the second stage the interest is to distinguish between lesion and non-lesion pixels. However, at each stage a larger number of classes is considered so that a multimodal distribution of one of the binary classes (in this case non-background and non-lesion) can be modeled as the superposition of multiple classes.

EM* Classification

A revision of the state-of-the-art algorithms for MS lesion detection shows that a number of methods are based on the popular Expectation Maximization (EM) algorithm [4]. The main reason for choosing EM is due to a good balance between simplicity, popularity and good results in this task. In general, this approach assumes that intensities belonging to the structures on MRI images follow a Rician distribution that can be fairly approximated by a Gaussian distribution [13] [14].

Therefore, each image contains a finite mixture of Gaussian distributions and thus the goal is to find the parameters that define these distributions and their proportions in the mixture. Given the number of Gaussian mixture components T, and their respective parameters $\theta_j = (\mu_j, \sigma_j)$ as well as their weight in the mixture β_j, for each class $j = 1, \ldots, T$, the intensity distribution for any pixel in the image can be expressed as:

$$p(l(\vec{r})|\theta) = \sum_{j=1}^{T} \beta_j \frac{1}{\sqrt{2\pi}\sigma_j} \exp\left\{-\frac{(l(\vec{r}) - \mu_j)^2}{2\sigma_j^2}\right\} \qquad (5)$$

In the first step, all the proportions β_j are equal to $1/T$, corresponding to a uniform distribution of classes; then, the parameters of the distributions θ_j are computed, which is called the Expectation step. After that, the Maximization step is applied, which consists in fixing the θ_j and then estimating the weights β_j. Both steps compose a single Expectation-Maximization iteration, and the EM method stops until convergence is achieved. Once the algorithm has converged, each pixel is classified with the class label which minimizes the Mahalanobis distance between the pixel intensity and the corresponding Gaussian component. That is, $c(\vec{r}) = \arg\min_j\{(l(\vec{r}) - \mu_j)^2/(2\sigma_j^2)\}$.

This popular EM classifier can be used to segment MS lesions within the proposed two-step framework for comparison purposes against the SP-GMMF classifier. Additionally, another proposal for MS lesion segmentation based on EM is presented here. Specifically, the two-step algorithm can be implemented, first using SP-GMMF to segment the brain, and then using EM at pixel level classification to segment MS lesions. For simplicity, this algorithm will be called EM*. Notice that, both EM* and EM methods follow the same MS lesion classification of the proposed SP-GMMF method. In other words, EM* and EM methods, in the first step of the algorithm obtain a mask of the brain, then an intensity adjustment operation is applied to the masked region, and finally in the second step, the EM algorithm is applied to the intensity-adjusted brain, and the same discrimination criteria is applied to obtain the MS lesions.

RESULTS AND DISCUSSION

For comparison purposes, both SP-GMMF and EM* were tested and compared against EM using both synthetic and real brain MRI images. A brief summary of the details for each algorithm is shown in Table 1. Experimental results were obtained using the BrainWeb dataset [27] and several MRI images (axial and sagittal sequences) from two subjects positively

diagnosed with MS of the Central Hospital in San Luis Potosí, México. Accuracy and reliability of the results were primarily measured using the Dice Similarity Coefficient (DSC) defined as:

$$DSC = 2\,|GT \cap R| / (|GT| + |R|) \quad (6)$$

where R is the estimated set of pixels corresponding to MS lesions obtained from the segmentation process, and GT corresponds to the Ground Truth. In the case of the BrainWeb set the ground truth was available on the BrainWeb site, and for real images, the GTs were manually obtained by one expert MS physician from the Central Hospital and validated by another expert from the same institution. In addition to DSC, the Sensitivity (SEN) and the average absolute difference between the number of lesions (ADNL) were computed as well.

TABLE 1. Block diagram of the proposed method SP-GMMF.

Algorithm	Brain Peeling	WML Detection	Resolution
EM	EM	EM	Pixel
EM*	SP-GMMF	EM	Pixel
SP-GMMF	SP-GMMF	SP-GMMF	Superpixel

The parameters for the first step (brain peeling) with SP-GMMF and EM* methods were: K' = 1000 desired number of SPs, γ = 0.1, κ = 0.1 and λ = 0.1 with 10 Gauss-Seidel iterations. The number of classes was C = 5, and their means were initialized by the k-means algorithm; the class with lowest mean intensity corresponds to the background, while the other classes correspond to the different anatomical structures in the image; however, it is important to recall that in this stage of the process we are interested in the largest connected non-background region, so the non-background classes are merged into a single class for this purpose. For the MS lesion detection stage, the parameters for the SP-GMMF and EM* were K' = 5000 for a finer resolution, κ = 0.1, λ = 2 and γ = 5 , with C = 7, with class means also initialized by the k-means algorithm; here, the class with highest mean intensity is considered to represent MS lesions. With respect to the EM method, the only parameter is the number of the classes, which we set **C** = 5 for the brain peeling stage and C = 7 for the MS lesion detection stage; class means are also initialized by k-means. Finally, in the False-Positive discrimination step, the criteria were a minimum area of 30 pixels and minimum eccentricity of 0.85 for all the algorithms. All parameters, including the number of classes considered at each stage, were optimized experimentally to maximize the DSC for real images from Subject 2 (see below).

Results from synthetic images

Data for these experiments consisted on simulated 181×217×181 T2-weighted MRI volumes from the MS Lesion Brain Database in Brain Web [27] with slice thickness of 1mm, noise levels of 0%, 1%, 3%, 5%, 7% and 9%, and intensity non-uniformity (INU) of 0% and 20%. A total of 12 volumes were used for the experiment. The experiment with synthetic MRI images was designed to test the robustness to noise and INU. For evaluation purposes, experiments were performed selecting only the four slices that contain the highest number of MS lesions, corresponding to slices 31 to 34. BrainWeb does not provide T2-FLAIR images so T2 images were used instead for this experiment; however, the ventricles appear with high intensity in T2 images and are easily confounded with MS lesions; for this reason, only four slices that do not contain the ventricles were used.

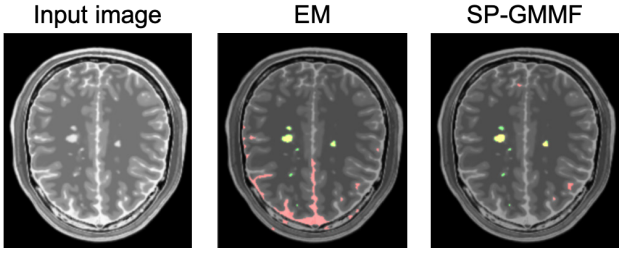

FIGURE 3. Application of the EM and SP-GMMF algorithms to slice 32 of the BrainWeb volume.

For illustration purposes, Figure 3 shows the results from the application of EM and SP-GMMF to slice 32 of the BrainWeb volume, where yellow regions correspond to true positive estimations, green regions correspond to false negatives and red regions correspond to false positives. Average results for these images are summarized in Figure 4.

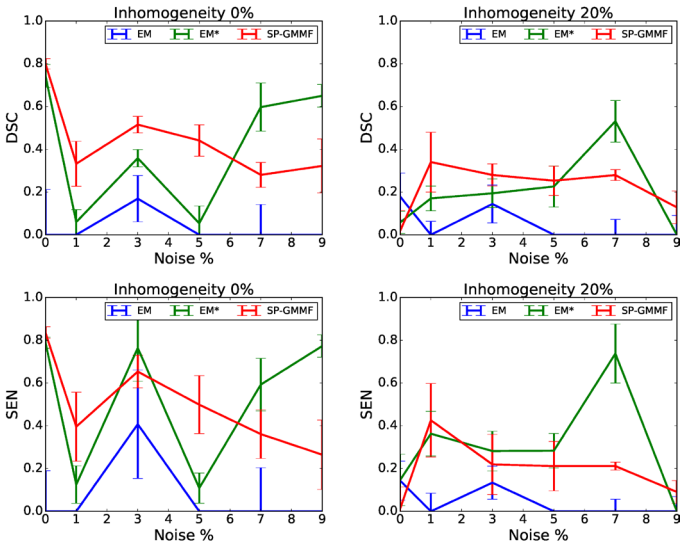

FIGURE 4. Average results of DSC and Sensitivity (SEN) from applying the EM, EM* and SP-GMMF methods on the BrainWeb images (slices 31 to 34).

Under low noise conditions (noise level <= 3%) and uniform intensity levels (INU = 0%), SP-GMMF achieves DSC values between 0.49 and 0.79 in average. However, when INU is increased to 20%, DSC values decrease approximately by a half, except in the case for 1% noise, in which the DSC values are maintained.

Additionally, a statistical analysis has been performed in order to determine if there exist significant differences in the performance indices (DSC and Sensitivity) between the different methods under study.

For this analysis, results for all noise levels were grouped so that each group consists of 24 data points (4 slices with 6 noise levels) for each method and INU level.

First, the Kruskal-Wallis non-parametric test was performed to see if there were differences in DSC or Sensitivity among the three methods for different INU levels; in all cases, significant differences ($p < 0.05$) were found. Post-hoc testing was then performed using the Kolmogorov-Smirnov and Mann-Whitney U tests, in order to determine which methods showed performance differences. The resulting p-values are summarized in Table 2.

TABLE 2. Results (p-values) from the Kruskal-Wallis (KW), Kolmogorov-Smirnov (KS) and Mann-Whitney U (MW) statistical tests to determine the existence of significant differences in performance measures (DSC and Sensitivity) between the methods under study (SP-GMMF, EM and EM*). P-values lower than 0.05 are shown in bold face, indicating significant differences among the methods in the corresponding row.

Dice Similarity Coefficient				
	Methods	All INU	0% INU	20% INU
KW	All methods	**0.0000**	**0.0000**	**0.0390**
KS	SP vs EM	**0.0000**	**0.0000**	**0.0120**
	SP vs EM*	0.1614	0.6860	0.2628
	EM vs EM*	**0.0000**	**0.0000**	0.1398
MW	SP vs EM	**0.0000**	**0.0000**	**0.0089**
	SP vs EM*	0.1479	0.3513	0.1045
	EM vs EM*	**0.0000**	**0.0000**	0.0504
Sensitivity				
	Methods	All INU	0% INU	20% INU
KW	All methods	**0.0000**	**0.0000**	**0.0093**
KS	SP vs EM	**0.0000**	**0.0000**	**0.0120**
	SP vs EM*	0.0996	0.9942	**0.0299**
	EM vs EM*	**0.0000**	**0.0000**	**0.0120**
MW	SP vs EM	**0.0000**	**0.0000**	**0.0100**
	SP vs EM*	0.2743	0.3706	0.2100
	EM vs EM*	**0.0000**	**0.0000**	**0.0017**

Furthermore, in order to determine the effect of intensity non-uniformity, a paired Wilcoxon test was performed to determine if there exist significant differences between INU levels 0% and 20% for each

method. Significant differences in DSC values were found for EM* (p=0.009) and SP-GMMF (p=0.002), and also in Sensitivity for EM* (p=0.036) and SP-GMMF (p=0.002, whereas EM did not show significant differences.

Results from real images

Another set of tests was performed with T2-FLAIR volumes from two MS patients acquired at the Central Hospital in San Luis Potosí, México, with a 1.5T MRI scanner. Images from Subject 1 (S1) were sampled approximately at 6.1 mm per slice, with each slice having a size of 512×512 pixels. For this test, four slices with visible MS lesions were selected: two axial and two sagittal.

The data set from the second subject (S2) is comprised by eight 256×256 axial images (A) and eight 288×288 sagittal images (S). Average results from the segmentation of these images using the methods under testing (EM, EM* and SP-GMMF) are shown in Table 3. Figure 5 shows boxplots of the DSC and SEN results.

TABLE 3. Average results (±standard error of mean) for real T2-FLAIR brain MRI images. Computed indices are: Dice Similarity Coefficient (DSC), Sensitivity (SEN) and Absolute Difference in Number of Lesions (ADNL – with the number of total lesions found shown in parentheses). Best results for each column are shown in bold face.

		S1	S2	
		A&S	A	A
DSC	EM	0.577±0.101	0.476±0.090	0.270±0.091
	EM*	0.610±0.076	0.479±0.084	0.401±0.099
	SP-GMMF	**0.697±0.007**	**0.576±0.081**	**0.454±0.081**
SEN	EM	0.592±0.136	0.576±0.116	0.559±0.115
	EM*	0.593±0.086	0.569±0.091	0.559±0.115
	SP-GMMF	**0.719±0.039**	**0.651±0.099**	**0.574±0.108**
ADNL	EM	3.25±0.48 (44)	1.50±0.46 (21)	2.00±0.63 (19)
	EM*	3.75±1.11 (40)	1.25±0.45 (17)	1.125±0.58 (24)
	SP-GMMF	**2.25±0.63 (30)**	**1.75±0.37 (15)**	**1.5±0.38 (23)**

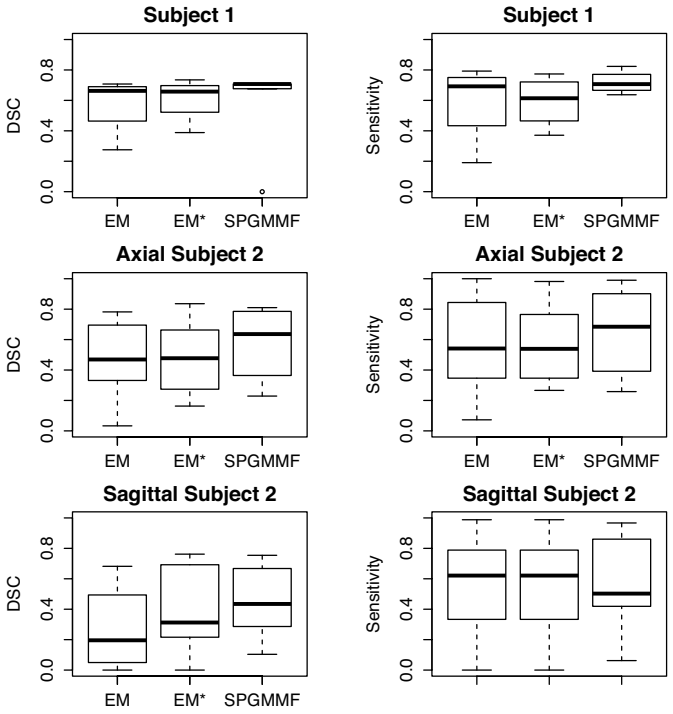

FIGURE 5. DSC and Sensitivity for both test subjects using the EM, EM* and SP-GMMF.

Figure 6 shows the results of the EM* and SP-GMMF algorithms for a few selected slices. Results are shown using the green channel for the true lesions and the red channel for the estimated lesions, so that yellow regions correspond to true positives, and green regions to false negatives. Statistical tests were also performed to determine if significant differences exist in the performance measures (DSC, Sensitivity and ADNL) among the three methods. In this case, however, the Kruskal-Wallis test did not report any evidence of significative differences; therefore, no post-hoc tests were applied.

Discussion

Experiments to test the accuracy of the proposed algorithm were perform using both synthetic and real MRI images of MS. The statistical analysis of the results for synthetic BrainWeb images suggest that INU highly affects the performance of the two proposed methods, SP-GMMF and EM*, since the DSC and sensitivity were strongly reduced when INU was set to 20%.

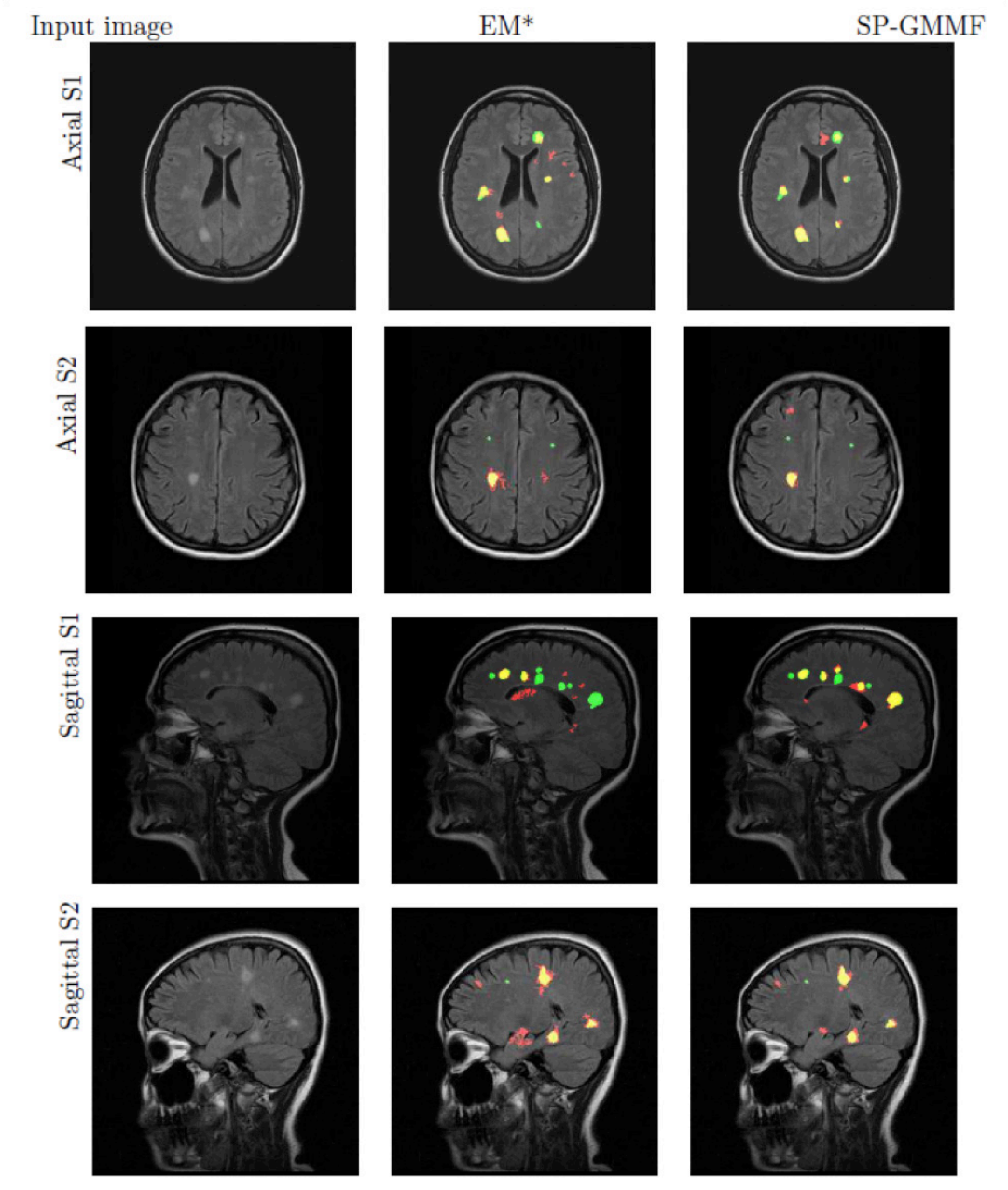

FIGURE 6. **Example of the results obtained with EM* and SP-GMMF. Yellow regions correspond to the true positive estimations, where the automatic segmentation coincides with the expert segmentation. Green regions correspond to false negatives (lesions that the automatic methods did not detect), and Red regions correspond to false positives (regions that the automatic algorithm incorrectly reports as lesions).**

With respect to the noise level, SP-GMMF shows a more consistent behavior with a mild decrease in DSC and Sensitivity as the noise increases, suggesting that the proposed algorithm is fairly robust to noise. On the other hand, it is difficult to characterize the behavior of EM and EM* under noisy conditions as their results are highly variable, but it seems that the pixel-wise approach employed by EM* can be of benefit in the lesion segmentation step under higher noise levels. A statistical analysis of the performance indices, whose

results are summarized in Table 2, shows that, in general, EM has a significantly lower performance than EM* and SP-GMMF, possibly due to errors in the brain peeling stage. On the other hand, no significant differences between EM* and SP-GMMF were found.

In the literature, some methods are applied to the BrainWeb data [24] [28] [29] [30] [31] with a high performance in DSC. However, their good results are not clearly explained, for example, some of them do not mention the slice (or slices) used for the tests. In [29], experiments using T1 and T2 images with 3% and 5% of noise are shown, obtaining a DSC of 0.782 in the best case. These experiments illustrate the main advantage of using prior information from an atlas; in general, using an atlas is a good option, however, algorithms without an atlas could reach similar performance; for instance, in [29] they report a DSC = 0.74 with an atlas and DSC = 0.75 without atlas. Moreover, they do not indicate which atlas is used or how the subject brain is registered to the atlas, which suggests they might have used the healthy BrainWeb data as atlas in order to avoid the registration process; in that case, applying the method proposed in [29] to real images would require further pre-processing steps which could introduce additional errors. In [31], the authors show a methodology based in Gauss-Markov model followed by curve evolution. Experiments were achieved using 61 slices (from the 60th to the 120th) using the T1, T2 and PD images. They obtained very good results since DSC is over 0.78 for 3% to 9% of noise. The results obtained by Garcia-Lorenzo *et al.* [28] present an interesting behavior for INU = 0%. The method yields a lower DSC = 0.24 for low noise levels (1%), increases its performance for 3% and 5% of noise (DSC of 0.65 and 0.79 respectively), and then decreases at 7% and 9% with DSC = 0.6 and DSC = 0.25, respectively. These results, along with our own results from Figure 4, suggest that some algorithms perform better when there is a mild amount of noise in the images. For instance, the EM and EM* algorithms estimate the mean and standard deviation of gray intensities for each class; in the absence of noise, the standard deviation will approach zero, which may cause numerical instabilities; on the other hand, the algorithm in [28] is gradient-based and may also be affected by untextured, noiseless regions. Table 4 summarizes the DSC results for various methods mentioned above, along with SP-GMMF for comparison purposes.

TABLE 4. DSC values reported for different MS lesion detection algorithms for synthetic (BrainWeb) and real MRI images. For each method, it is indicated if the method requires multi-modal images (T1, T2, PD/FLAIR), and if it requires prior information in the form of an atlas or user assistance.

Method	DSC for BrainWeb Images	DSC for Real Images	Requires multiple modality	Requires prior data
TOADS [12]	0.79	0.63	x	x
Graph Cuts [28]	~0.7	0.63	x	
AWEM [30]	0.7		x	
CGMM+CE [31]	0.78		x	x
Khayati [6] [7]		0.75		
SP-GMMF	0.49 - 0.79 (low noise)	~0.6		

Despite the sensitivity to INU and noise, experiments with real images suggest that the proposed methods can be used for a real application with encouraging results. Figure 5 shows the boxplots of the DSC and the sensitivity for the EM, EM* and the SP-GMMF methods. For Subject 1, SP-GMMF shows better DSC and sensitivity than the EM based methods. For Subject 2, the results show a considerable variability between slices; in general, SP-GMMF presents a higher median DSC but a lower sensitivity in the case of the sagittal images. Table 3 summarizes the average DSC, sensitivity and ADNL of the proposed methods, where the best result is highlighted in boldface. In this case, the best DSC performance is obtained by the SP-GMMF method with a competitive average DSC of 0.6968 for Subject 1 and average DSC of 0.5762 and 0.4544 for Subject 2 axial and sagittal images, respectively. SP-GMMF also

presents the highest average sensitivity. Nevertheless, the best ADNL is obtained by the EM* method; this is interesting because the number of lesions is one of the main clinical indices to characterize the progress of the MS disease. To our knowledge, only a few works in the literature report results with real images. In [30], they report results from three different patients for which they can obtain DSC values of 82%, 56%, and 52%, respectively. In [28], experiments with 10 patients yield DSC values between 40% and 75%. Considering that the authors of these works use multi-modal images (combining T1-w, T2-w, FLAIR and PD) with high resolution, we consider our results (DSC between 45% and 69%) to be competitive for low-resolution single modality imaging.

Finally, we discuss the differences in the false positive lesions reported by the proposed methods, as shown in Figure 6. Ideally, the algorithm should report no false negatives while keeping the number of false positives as low as possible. For subject one, SP-GMMF shows more accuracy because there are more yellow regions (true positives) and less red regions (false positives) than the segmentations obtained by the EM*, particularly in the sagittal image. For subject two, the advantage of SP-GMMF versus EM* is not clearly evident as they show almost the same yellow regions. Nevertheless, a detailed inspection of these images suggests that the EM* segmentation tends to generate a higher number of false positive (red regions), possibly due to the lack of regularization, such as the one induced by using superpixels, at the MS lesion detection stage.

CONCLUSIONS

An automatic algorithm to detect and segment Multiple Sclerosis lesions from T2 MR images was presented. The proposed method is based on a segmentation process where the image is subdivided into connected clusters (superpixels) which are then labeled according to their average intensity using Gauss-Markov Measure Field model. The segmentation process is applied two-fold: first to isolate the brain region, and then to detect hyperintense spots within the brain region. Finally, some of the false positives are discarded depending on their area and eccentricity. An experimental test using synthetic images from the BrainWeb database shows that the proposed segmentation has strong advantages against the popular EM method, even under noisy conditions. While SP-GMMF is fairly robust to noise, it is very sensitive to non-uniformity, so additional pre-processing might be required for some images to deal with the spatial intensity variations. In the case of real MRI images, SP-GMMF maintains its advantages against EM, although using EM for detecting hyperintense spots (once the brain region has been isolated) has shown benefits, such as a more accurate lesion count. In brief, the SP-GMMF produces competitive results with single-modality, low-resolution images; it is also fully automatic and does not depend on prior anatomic information. Thus, SP-GMMF and EM* could be adequate image processing tools for low-resource institutions. We are currently working on implementing the proposed algorithms as part of an interactive application that can be used for clinical purposes, where an expert physicist can manually refine the segmentation by setting post-processing parameters in real-time and deleting spurious lesions, and then obtain indices such as the number and volume of lesions.

AUTHOR CONTRIBUTIONS

A.R. Contributed to the implementation of the proposed methodology and in conducting the experiments. A.A. Contributed in the direction of the project and development of the methodology. M.O.M. Contributed in the experimental design, validation of the results, reviewing the manuscript and management activities. E.R.A.S Contributed in the development of the methodology, validation of results and reviewing the manuscript. I.R.L. Contributed in the raise of the problem, development of the methodology, data acquisition and expert validation of the real cases (ground truth).

REFERENCES

[1] Benito-León J, Morales JM, Rivera-Navarro J, Mitchell AJ. A review about the impact of multiple sclerosis on health-related quality of life. Disability and Rehabilitation. 2003;25(23):1291-1303. https://doi.org/10.1080/0963828031000160859 1

[2] Manjón JV, Coupé P. volBrain: An Online MRI Brain Volumetry System. Frontiers in Neuroinformatics. 2016; 10:30. https://doi.org/10.3389/fninf.2016.00030

[3] Smith SM. Fast robust automated brain extraction. Human Brain Mapping. 2002;17(3):143-155. https://doi.org/10.1002/hbm.10062

[4] Mortazavi D, Kouzani AZ, Soltanian-Zadeh H. Segmentation of multiple sclerosis lesions in MR images: a review. Neuroradiology. 2012; 54(4): 299-320. https://doi.org/10.1007/s00234-011-0886-7

[5] Garcia-Lorenzo D, Francis S, Narayanan S, Arnold DL, Collins DL. Review of automatic segmentation methods of multiple sclerosis white matter lesions on conventional magnetic resonance imaging. Medical Image Analysis. 2013;17(1):1-18. https://doi.org/10.1016/j.media.2012.09.004

[6] Khayati R, Vafadust M, TowhidkhahF , Nabavi M. Fully automatic segmentation of multiple sclerosis lesions in brain MR FLAIR images using adaptive mixtures method and markov random field model. Computers in Biolology and Medicine. 2008;38(3): 379-390. https://doi.org/10.1016/j.compbiomed.2007.12.005

[7] Khayati R, Vafadust M, Towhidkhah F, Nabavi M. A novel method for automatic determination of different stages of multiple sclerosis lesions in brain MR FLAIR images. Computerized Medical Imaging and Graphics. 2008;32(2):124-133. https://doi.org/10.1016/j.compmedimag.2007.10.003

[8] Vapnik VN. An overview of statistical learning theory. IEEE Transactions on Neural Networks. 1999;10(5): 988-999. https://doi.org/10.1109/72.788640

[9] Zijdenbos AP, Dawant BM, Margolin RA, Palmer AC. Morphometric analysis of white matter lesion in MR images: method and validation. IEEE Transactions on Medical Imaging. 1994;13(4):716-724. https://doi.org/10.1109/42.363096

[10] de Boer R, van der Lijn F, Vrooman HA, Vernooij MW, Ikram MA, Breteler MMB, Niessen WJ. Automatic segmentation of brain tissue and white matter lesions in MRI. In 4th IEEE International Symposium on Biomedical Imaging: From Nano to Macro. Arlington: IEEE;2007:652-655. https://doi.org/10.1109/ISBI.2007.356936

[11] Awad M, Chehdi K, Nasri A. Multicomponent Image Segmentation Using a Genetic Algorithm and Artificial Neural Network. IEEE Geoscience and Remote Sensing Letters. 2007; 4(4): 571-575. https://doi.org/10.1109/LGRS.2007.903064

[12] Shiee N, Bazin P-L, Ozturk A, Reich DS, Calabresi PA, Pham DL. A topology-preserving approach to the segmentation of brain images with multiple sclerosis lesions. NeuroImage. 2010;49(2):1524-1653. https://doi.org/10.1016/j.neuroimage.2009.09.005

[13] Aït-Ali LS, Prima S, Hellier P, Carsin B, Edan G, Barillot C. STREM: A Robust Multidimensional Parametric Method to Segment MS Lesions in MRI. In Duncan JS, Gerig G (eds.). Medical Image Computing and Computer-Assisted Intervention MICCAI. Berlin: Sprinfer.2005;3749:409-416. https://doi.org/10.1007/11566465_5

[14] Dempster AP, Laird NM, Rubin DB, Maximum Likelihood from Incomplete Data via EM Algorithm. Journal of the Royal Statistical Society. 1977;39(1):1-22. https://doi.org/10.1111/j.2517-6161.1977.tb01600.x

[15] García-Lorenzo D, Prima S, Morrissey SP, Barillot C. A robust Expectation-Maximization algorithm for Multiple Sclerosis lesion segmentation. MICCAI Workshop: 3D Segmentation in the Clinic: A Grand Challenge II, MS lesion segmentation. 2008:1-8.

[16] Bartko JJ. Measurement and Reliability: Statistical Thinking Considerations. Schizophrenia Bulletin. 1991;17(3):483-489. https://doi.org/10.1093/schbul/17.3.483

[17] Powers D. Evaluation: from Precision, Recall and F-measure to ROC, Informedness, Markedness and Correlation. Journal Machine Learning Technologies. 2011;2(1):37-63.

[18] Lao Z, Shen D, Liu D, Jawad AF, Melhem ER, Launer LJ, Bryan RN, Davatzikos C. Computer-Assisted Segmentation of White Matter Lesions in 3D MR images using Support Vector Machine. Academic Radiology. 2008;15(3):300-313. https://doi.org/10.1016/j.acra.2007.10.012

[19] Viola P, Wells WM. Alignment by Maximization of Mutual Information. International Journal of Computer Vision. 1997;24(2):137-154. https://doi.org/10.1023/A:1007958904918

[20] Wang XY, Wang T, Bu J. Color image segmentation using pixel wise support vector machine classification. Pattern Recognition. 2011;44(4):777-787. https://doi.org/10.1016/j.patcog.2010.08.008

[21] Toussaint N, Souplet JC, Fillard P. MedINRIA: Medical Image Navigation and Research Tool by INRIA. In Proceedings of MICCAI Workshop on Interaction in Medical Image Analysis and Visualization. Brisbane: MICCAI. 2007;4791:1-8.

[22] Achata R, Shaji A, Smith K, Lucchi A, Fua P, Süsstrunk S. SLIC Superpixels Compared to State-of-the-Art Superpixel Methods. IEEE Transactions on Pattern Analysis Machine Intelligence. 2012;34(11):2274-2282. https://doi.org/10.1109/TPAMI.2012.120

[23] Marroquin JL, Velasco FA, Rivera M, Nakamura M. Gauss-Markov measure field models for low-level vision. IEEE Transactions on Pattern Analysis Machine Intelligence. 2001;23(4):337-348. https://doi.org/10.1109/34.917570

[24] Cheng J, Liu J, Xu Y, Yin F, Kee-Wong DW, Tan NM, Tao D, Cheng CY, Aung T, Wong TY. Superpixel Classification Based Optic Disc and Optic Cup Segmentation for Glaucoma Screening. IEEE Transactions on Medical Imaging. 2013;32(6):1019-1032. https://doi.org/10.1109/TMI.2013.2247770

[25] Ren CY, Reid I. gSLIC: a real-time implementation of SLIC superpixel segmentation. Technical Report [Internet]. 201:1-6. Available from: *http://www.carlyuheng.com/pdfs/gSLIC_report.pdf*.

[26] Haralick RM, Shapiro LG. Computer and Robot Vision. Boston, United States: Addison-Wesley Longman Publishing;1992:28-48p.

[27] Cocosco CA, Kollokian V, Kwan KS, Pike GB, Evan AC. BrainWeb: Online Interface to a 3D MRI Simulated Brain Database. NeuroImage. 1997;5:425.

[28] García-Lorenzo D, Lecoeur J, Arnold DL, Collins DL, Barillot C. Multiple Sclerosis Lesion Segmentation Using an Automatic Multimodal Graph Cuts. In Yang G-Z, Hawkes D, Rueckert D, Noble A, Taylor C (eds.). Medical Image Computing and Computer-Assisted Intervention - MICCAI 2009. Berlin, Heidelberg: Springer Berlin Heidelberg; 2009:584-591. https://doi.org/10.1007/978-3-642-04271-3_71

[29] Bricq S, Collet Ch, Armspach JP. Lesions detection on 3D brain MRI using trimmed likelihood estimator and probabilistic atlas. 2008 5th IEEE International Symposium on Biomedical Imaging: From Nano to Macro. Paris; IEEE. 2008:93-96. https://doi.org/10.1109/ISBI.2008.4540940

[30] Forbes F, Doyle S, Garcia-Lorenzo D, Barillot C, Dojat M. Adaptive weigthed fusion of multiple MR sequences for brain lesion segmentation. 2010 IEEE International Symposium on Biomedical Imaging: From Nano to Macro. Rotterdam: IEEE. 2010:69-72. https://doi.org/10.1109/ISBI.2010.5490413

[31] Freifeld O, Greenspan H, Goldberger J. Multiple Sclerosis Lesion Detection Using Constrained GMM and Curve Evolution. International Journal of Biomedical Imaging. 2009: 715124. https://doi.org/10.1155/2009/715124

RESEARCH ARTICLE

Vol. 41 | No. 3 | **SEPTIEMBRE - DICIEMBRE 2020** | pp 56-71

REVISTA MEXICANA DE Ingeniería Biomédica

dx.doi.org/10.17488/RMIB.41.3.4

E-LOCATION ID: 1080

Biped Gait Analysis based on Forward Kinematics Modeling using Quaternions Algebra

J. C. González-Islas[1, 2], *O. A. Domínguez-Ramírez*[1], *O. López-Ortega*[1]

[1]Universidad Autónoma del Estado de Hidalgo

[2]Universidad Tecnológica de Tulancingo

ABSTRACT

Gait is the main locomotion way for human beings as an autonomous decision. Due to the increase in people with walking disabilities, the precision in gait analysis for purposes in clinical diagnosis, sports medicine or biomechanical research for the design of assistive technologies is of special relevance. The literature reports notable contributions in technological developments with diverse applications; and in some cases, algorithms for characterization and gait analysis; however, more studies related to gait kinematics are necessary, such as the solution proposed in this work. In this paper, we focus on studying the forward kinematics of the lower limbs in human gait, using in a novel way quaternions algebra as mathematical tool and comparative analysis with classical methods is established. Gait analysis unlike other works is carried out by evaluating the rotational and tilting movements of the pelvis, flexion-extension of the hip and knee; as well as dorsiflexion and plantarflexion of the ankle. Finally, an assessment of normal, mild crouch and severe crouch gaits in the three anatomical planes is performed; and a metric based on the Euclidean norm in the cartesian space is used to evaluate these gaits.

KEYWORDS: Gait analysis; Forward kinematics of position; Lower limbs; Quaternions algebra; Walking disability

Corresponding author

TO: **Omar Arturo Domínguez Ramírez**

INSTITUTION: **Universidad Autónoma del Estado de Hidalgo**

ADDRESS: **Pachuca-Tulancingo Km. 4.5, Col. Carboneras, C. P. 42184, Pachuca de Soto, Hidalgo, México**

E-MAIL: **omar@uaeh.edu.mx**

Received:

4 June 2020

Accepted:

12 November 2020

INTRODUCTION

Gait analysis has been used to evaluate different conditions in sport sciences, biomechanics and clinical diagnosis [1]. In clinical environments, this assessment tool has been applied to diagnose: hemiplegia [2], Achilles tendinopathy [3], inversion sprains [4], Parkinson's disease [5], hip arthroplasty [6], knee osteoarthritis [7], idiopathic scoliosis [8], cervical myelopathy [9], among others. In the same way, gait analysis has allowed to estimate the progress of patients rehabilitated after a stroke [10]; or simply to determine the joint displacement in the hip, knee and ankle [11] [12]. In this paper, we focus on studying the kinematics of the lower limbs in human gait based on quaternions algebra.

On the other hand, quaternions are useful to perform a rotation of vectors in a 3D space [13]. Today, they are widely used in computer graphics, multirotor tracking and control approaches, and kinematics and dynamics of rigid bodies [14]. Therefore, the free representation of the quaternions in the Euclidian space has also been used in navigation, computer-aided design and computer vision [15].

Recently, interest in robotic developments has been increased. The most well-known methods for robot kinematics are the Denavit-Hartenberg convention [16] and geometric methods [17]. Therefore, most of the work done to model robot kinematics using quaternions continues to follow the D-H approach, wasting quaternions capacity [15]. Some robotic applications have been focused on gait approaches to establish the imitation of human gait. For example, a robotic platform for the kinetics and kinematics characterization during gait has been used [18]. Therefore, mathematical models that associate forward kinematics of position are required [19]. For this reason, in this work we present a theoretical approach for modeling forward kinematics of position of the lower limbs for human gait using quaternions algebra not based on the D-H convention.

Related work

Some methods have been proposed in the literature for the three-dimensional analysis of gait kinematics using wearable sensors and quaternions algebra [20] [21]. In the first work, the initial orientations are computed by quaternions of the inertial sensors placed in pelvis, femur, tibia and foot, which are acquired from the acceleration data, while the angular displacement is defined from the angular velocity. Subsequently, the orientations of the independent body segments are obtained from the sensor's orientation and the calibration rotation matrix, to then synthesize a 3D model of the whole body concerning the global reference frame. Similarly, the algebra-based position of quaternions of the frame of each joint is obtained from the gyroscope and the accelerometer signals [21]. Therefore, in addition to the existence of position estimation error derived from the use of inertial sensors, in both works, there is a low performance in the gait analysis, since anthropometry is not directly considered and, the joint system is handled by an independent structure and not as a serial chain.

On the other hand, in the work [22], a local analysis of the stability of the joints during walking is carried out using a marker-based optical system. This implies that forward kinematics of position is also obtained from the position of the markers and the calibration test [5] [6] [7]. In addition to what has been mentioned in this section in the aforementioned works, only the hip, knee and ankle are analyzed, that is why, to have greater precision in the kinematic calculation of gait, it is necessary to include the rotational and tilting movements of the pelvis.

Problem statement

Generally, the normal gait pattern is established in the joint space [23] and independently from each anatomical movement of each joint structure. Which limits the global perception of the performance of the joint system and the use of well-known metrics such

as speed, cadence and stride length, which are established in the operational space (gait space) and are related to anthropometry of the individual. Therefore, the calculation of direct kinematics is necessary to determine the gait pattern in cartesian space as a function of joint variables.

Although the well-known Denavit-Hartenberg DH [16] convention and geometric [17] methods can solve well the forward kinematics of position in the sagittal plane of the 3 DoF joint system of the lower limbs (Figure 2), if the number of degrees of freedom of analysis in the transversal and frontal planes is increased as in the 8 DoF system (Figure 3), these methods require a more complex mathematical modeling and are less flexible in the description of the evolutions of the system of the extremities with respect to the orthonormal frame of reference. Therefore, a method of lower mathematical complexity, with a low computational cost and that requires little storage capacity [15] is required for the analysis of the gait in cartesian space as the one proposed in this contribution.

Proposed solution

In this work, a method to calculate the forward kinematics of position of the articular system of the lower limbs during gait, using quaternion algebra as a mathematical tool is proposed. To this end, the modeling of the articular system of the lower extremities is established as an open serial chain, which allows obtaining a global performance of the system and a reference pattern of normal gait in the operational space. Also, the analysis in the gait space allows the evaluation of the metrics of that space and some not common metrics for this purpose such as: the Euclidean distance, the areas and the centroid between each reference. Finally, to evaluate abnormal performances in the cartesian space for reference pattern, a comparative analysis is performed in the 3 anatomical planes for a normal gait and 2 types of crouched gaits, of which their forward position kinematics is calculated from the articular anatomical positions related to the rotation and inclination of the pelvis, dorsiflexion of the hips and knees, as well as dorsiflexion and plantarflexion of the ankles.

Paper organization

In this work, the anthropometry and the joint parameters considered as the starting point are adapted to [20] and [24], respectively. Subsequently, mathematical modeling is proposed to calculate the forward kinematics of position of the 3 DoF lower limbs joint system (Figure 2), which directly considers anthropometry, using the methods: i) geometric, ii) Denavit-Hartenberg and iii) quaternions. Later, due to the increase in complexity, the modeling of the forward kinematics 8 DoF system (Figure 3) is developed using quaternions, a simulation of the kinematics is performed and the cartesian coordinates and joint variables of both extremities are visualized. Finally, a metric based on the Euclidean distance between both ends of the feet (big toe), ankles and knees are calculated.

To describe the work done, this paper is organized as follows: Related work, problem statement and proposed solution are described in the introduction section. In the materials and methods section, the mathematical modeling for the calculation of the forward kinematics of position of joint systems and lower limbs using the methods: i) geometric, ii) Denavit-Hartenberg and iii) quaternions algebra, is presented. The analysis and discussion of results is shown in the corresponding section and finally, the last section focuses on the conclusions.

MATERIALS AND METHODS

Kinematics is the study of the motion of mechanical systems without regard to the cause of the motion. The most well-known methods for forward kinematics of position of robots are the Denavit-Hartenberg convention [16] and geometric [17] methods. In this work,

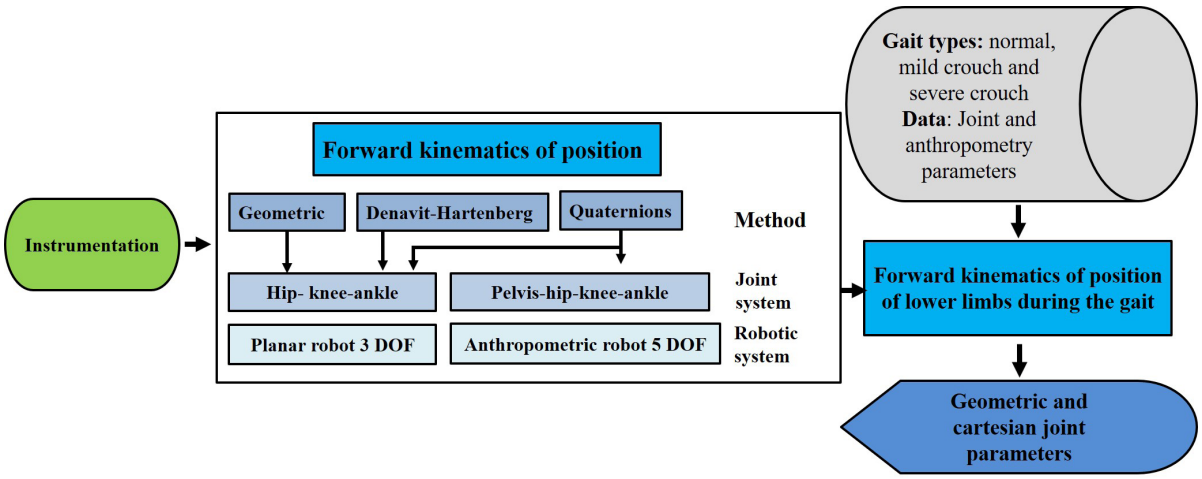

FIGURE 1. Methodology for the modeling and visualization of the forward kinematics of position of the lower limbs during gait using methods: i) geometric, ii) Denavit-Hartenberg and iii) quaternions for joint and anthropometry variables established in [20] and [24], respectively.

the lower limb joint system is considered as a set of rigid links connected together at various joints during the swing phase of the gait cycle. Therefore, the methodologies used in robotics such as: i) geometric method ii) D-H) and iii) quaternions [25], can be used to calculate the forward kinematics of position of the lower limbs during gait, which is described as follows.

Forward kinematics of lower limbs

Hip - knee - ankle system (HAK)

To develop the kinematic analysis in this work, the anatomical terms describing the relationships of the different parts of the body are based on the anatomical positions of sagittal, frontal and transverse planes; and their main directions [23]. Firstly, we develop a synthesis of forward kinematics of position of 3 DoF system as a planar robot, whose home position in (Figure 2) of the first link is on the y_{0R}(-) axis of the origin of the base frame $O\Sigma_{0R}$, and the origins of the orthonormal frames of the robot correspond with the reference points of the joints of the human's lower right limb model (Table 1). In this case, the anatomical sagittal plane corresponds to the *x-y* plane of the robot, while that z_{0R}(+), x_{0R}(+) and y_{0R}(+) axes correspond to the right, front and top directions, respectively [23]. The model features lower limb right joint as 3 rigid-body segment 1) femur, 2) tibia and 3) foot and the anthropometry is adopted from [20]. The relative motion of these segments is defined successively by quaternions algebra.

TABLE 1. Correspondences between the orthonormal frames of the 3 DOF planar robot and the join references of the body (Figure 2).

Orthonormal cartesian frames	Joint references of The right lower limb
$O\Sigma_{0R}(x_{0R}, y_{0R}, z_{0R})$	Hip
$O\Sigma_{1R}(x_{1R}, y_{1R}, z_{1R})$	Knee
$O\Sigma_{2R}(x_{2R}, y_{2R}, z_{2R})$	Ankle
$O\Sigma_{3R}(x_{3R}, y_{3R}, z_{3R})$	Big toe

Let, l_{1R} , l_{2R}, l_{3R}, Q_{1R}, Q_{2R} and Q_{3R} the anatomical length dimesions of femr, tibia and foot, and the flexion-extension angles of the hip and knee, as well as dorsiflexion and plantarflexion of the ankle, of the right lower limb, respectively. Then, if we consider symmetry for the left limb it is possible to apply the methods mentioned in the previous section to get forward kinematics of position for both right (denoted by subscript

R) and left (denoted by subscript L) limbs. Commonly, hip, knee and ankle have only been used to analyze the gait kinematics [11] [12] [20] [26].

In a 3 DoF planar robot, the width of each servomotor and the thickness of the joint bar are determined by β_{1R}, β_{2R} and β_{3R}, for simplicity in this case, these values are equal to 0. The placement of the z_{iR} axes coincide with the axes of rotation of the joints, while the x_{iR} axis is assigned in the direction of the link and the y_{iR} axis according to the right-hand rule. Meanwhile, q_{1R}, q_{2R} and q_{3R} are the hip and knee flexo-extension, and ankle dorsiflexion and plantarflexion, with respect to the z_{0R}, z_{1R} and z_{2R} axis, respectively.

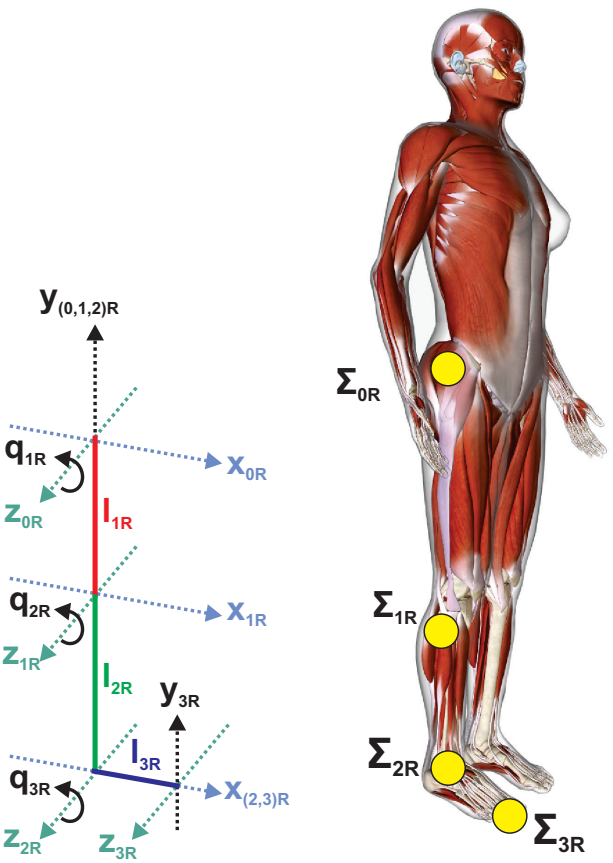

FIGURE 2. a) Open kinematic chain that represents the frames that define joint movements in the sagittal plane. b) Correspondence of the frames to the musculoskeletal reference points in the female model [27].

Geometric method

The position of the right big toe $[x_{3R}, y_{3R}, z_{3R}]^T \epsilon R^{3x1}$ without orientation, could be obtained geometrically adding a link in the x_{0R} axis direction, whose joint is arranged in the Σ_{2R} frame origin (Figure 2) [17], such that, the coordinates of such position are determined as

$$x_{3R} = l_{1R}\, s_{q_{1R}} + l_{2R} s_{q_{1R}+q_{2R}} + l_{3R} c_{q_{1R}+q_{2R}+q_{3R}} \quad (1)$$

$$y_{3R} = -l_{1R}\, c_{q_{1R}} - l_{2R} c_{q_{1R}+q_{2R}} + l_{3R} s_{q_{1R}+q_{2R}+q_{3R}} \quad (2)$$

$$z_{3R} = \beta_{1R} + \beta_{2R} + \beta_{3R} = 0 \quad (3)$$

where c_{qiR} and s_{qiR} are the cosine and sine transcendental functions that depend on q_{iR}, respectively.

Similarly, the position of the left big toe could be obtained by the D-H convention.

Denavit - Hartenberg convention

If we assume the same configuration (Figure 2), by means of the D-H convention [16] the parameters of the joints and the links of the right lower limb are shown in (Table 2).

TABLE 2. Denavit-Hartenberg parameters for the HAK system (Figure 2).

$link_i$	θ_i	d_i (β_i)	l_i	α_i
1	$q_{1R} - \frac{\pi}{2}$	β_{1R}	l_{1R}	0
2	q_{2R}	β_{2R}	l_{2R}	0
3	$q_{3R} + \frac{\pi}{2}$	β_{3R}	l_{3R}	0

Thus, the homogeneous transformation matrices for each link can be written as

$$H_{0R}^{1R} = \begin{bmatrix} s_{q_{1R}} & c_{q_{1R}} & 0 & l_{1R} s_{q_{1R}} \\ -c_{q_{1R}} & s_{q_{1R}} & 0 & -l_{1R} c_{q_{1R}} \\ 0 & 0 & 1 & 0 \\ 0 & 0 & 0 & 1 \end{bmatrix} \quad (4)$$

$$\boldsymbol{H}_{\boldsymbol{1R}}^{\boldsymbol{2R}} = \begin{bmatrix} c_{q_{2R}} & -s_{q_{2R}} & 0 & l_{2R}c_{q_{2R}} \\ s_{q_{2R}} & c_{q_{2R}} & 0 & l_{2R}s_{q_{2R}} \\ 0 & 0 & 1 & 0 \\ 0 & 0 & 0 & 1 \end{bmatrix} \quad (5)$$

$$\boldsymbol{H}_{\boldsymbol{2R}}^{\boldsymbol{3R}} = \begin{bmatrix} -s_{q_{3R}} & -c_{q_{3R}} & 0 & -l_{3R}s_{q_{3R}} \\ c_{q_{3R}} & -s_{q_{3R}} & 0 & l_{3R}c_{q_{3R}} \\ 0 & 0 & 1 & 0 \\ 0 & 0 & 0 & 1 \end{bmatrix} \quad (6)$$

Then, applying trigonometric identities D-H procedure [16], the generalized homogeneous transformation matrix results as

$$\boldsymbol{H}_{\boldsymbol{0R}}^{\boldsymbol{3R}} = \begin{bmatrix} c_{q_{1R}+q_{2R}+q_{3R}} & -s_{q_{1R}+q_{2R}+q_{3R}} & 0 & x_{3R} \\ s_{q_{1R}+q_{2R}+q_{3R}} & c_{q_{1R}+q_{2R}+q_{3R}} & 0 & y_{3R} \\ 0 & 0 & 1 & z_{3R} \\ 0 & 0 & 0 & 1 \end{bmatrix} \quad (7)$$

where x_{3R}, y_{3R} and z_{3R} are equivalents to the Equation (1), Equation (2) and Equation (3) of the geometric method. Therefore, the end position of the point $O\Sigma_{3R}$ (x_{3R}, y_{3R}, z_{3R}) is the same using the geometric method and the D-H convention.

Quaternions-based forward kinematics

The four-dimensional space H is formed by the real axis and three orthogonal axis, spanned by the principal imaginaries vectors $\boldsymbol{i}$= (1,0,0), $\boldsymbol{j}$=(0,1,0) and $\boldsymbol{k}$= (0,0,1), which obey Hamilton rules [28]: $\boldsymbol{i^2}$= $\boldsymbol{j^2}$= $\boldsymbol{k^2}$= $\boldsymbol{ijk}$= $\boldsymbol{-1}$. Where multiplication of these imaginaries resembles cross product, such that $\boldsymbol{ij}$= $\boldsymbol{k}$, $\boldsymbol{jk}$= $\boldsymbol{i}$, $\boldsymbol{ki}$= $\boldsymbol{j}$, $\boldsymbol{ji}$= $\boldsymbol{-k}$, $\boldsymbol{kj}$= $\boldsymbol{-i}$, $\boldsymbol{ik}$= $\boldsymbol{-j}$.

A quaternion Q= $r + x\boldsymbol{i} + y\boldsymbol{j} + z\boldsymbol{k}$ consists of a real part r and a pure part $\boldsymbol{v}$= $x\boldsymbol{i} + y\boldsymbol{j} + z\boldsymbol{k}$ [13]. Let Q_1= $a_1 + \boldsymbol{v_1}$ and Q_2= $a_2 + \boldsymbol{v_2}$ two quaternions, then, their product is calculated using the dot product and the cross product as:

$$Q_1Q_2 = a_1a_2 - \boldsymbol{v_1} \cdot \boldsymbol{v_2} + a_1\boldsymbol{v_2} + a_2\boldsymbol{v_1} + \boldsymbol{v_1} \boldsymbol{x} \boldsymbol{v_2} \quad (8)$$

The quaternion Q= a+v also decomposes into a+$b\boldsymbol{u}$, which resembles a complex number, where the imaginary $\boldsymbol{u}$ is a unit-three vector

$$\boldsymbol{u} = \begin{pmatrix} x/_b \\ y/_b \\ z/_b \end{pmatrix} = \frac{x}{||\boldsymbol{v}||}\boldsymbol{i} + \frac{y}{||\boldsymbol{v}||}\boldsymbol{j} + \frac{z}{||v||}\boldsymbol{k} \quad (9)$$

Thus, $|(|\boldsymbol{u}|)|$= 1 and x, y, z are the cartesian coordinates of $\boldsymbol{v}$. Let Q= $a + b\boldsymbol{u}$, so its conjugate is $\bar{Q}$= a - $b\boldsymbol{u}$ [29].

On the other hand, a rotation of θ around axis $\boldsymbol{u}$ is represented as the unit quaternion.

$$Q = \cos\left(\frac{\theta}{2}\right) + \boldsymbol{u}\, sin\, \left(\frac{\theta}{2}\right) \quad (10)$$

Given a unit quaternion Q that represents a rotation, then, the rotation around an arbitrary pure vector $\boldsymbol{v} \in R^3$ is

$$R(Q)\boldsymbol{v} = Q\boldsymbol{v}\bar{Q} \quad (11)$$

where $\bar{Q}$= cos ($\frac{\theta}{2}$) - $\boldsymbol{u}$ sin ($\frac{\theta}{2}$) is the conjugate.

Then, if we represent the HAK system (Figure 2), by quaternions algebra, from Equation (10) the quaternion representation of the rotation around the z_{0R} axis is

$$Q_{1R} = \cos\left(\frac{q_{1R}}{2}\right) + \boldsymbol{u_{1R}}\, sin\, \left(\frac{q_{1R}}{2}\right) \quad (12)$$

Where $\boldsymbol{u}_{\boldsymbol{1R}}$= [0, 0, 0, k] is a unit vector, q_{1R} is the rotation angle around the z_{0R} axis and OΣ is the rotation angle around the z_{0R} axis and $O\Sigma_{1R}$= [0, 0, -$l_{1R}\boldsymbol{j}$, 0] is the representation of the home position of the frame Σ_{1R} origin. Then, the rotated final from $\boldsymbol{O\Sigma_{1R}}$ using Equation (11) is $\boldsymbol{O\Sigma_{1Rf}}$= $Q_{1R}\boldsymbol{O\Sigma_{1R}}\overline{Q_{1R}}$.

Let us

$$Q_{2R} = \cos\left(\frac{q_{2R}}{2}\right) + \boldsymbol{u_{2R}}\, sin\, \left(\frac{q_{2R}}{2}\right) \quad (13)$$

$$Q_{3R} = \cos\left(\frac{q_{3R}}{2}\right) + \boldsymbol{u_{3R}}\, sin\, \left(\frac{q_{3R}}{2}\right) \quad (14)$$

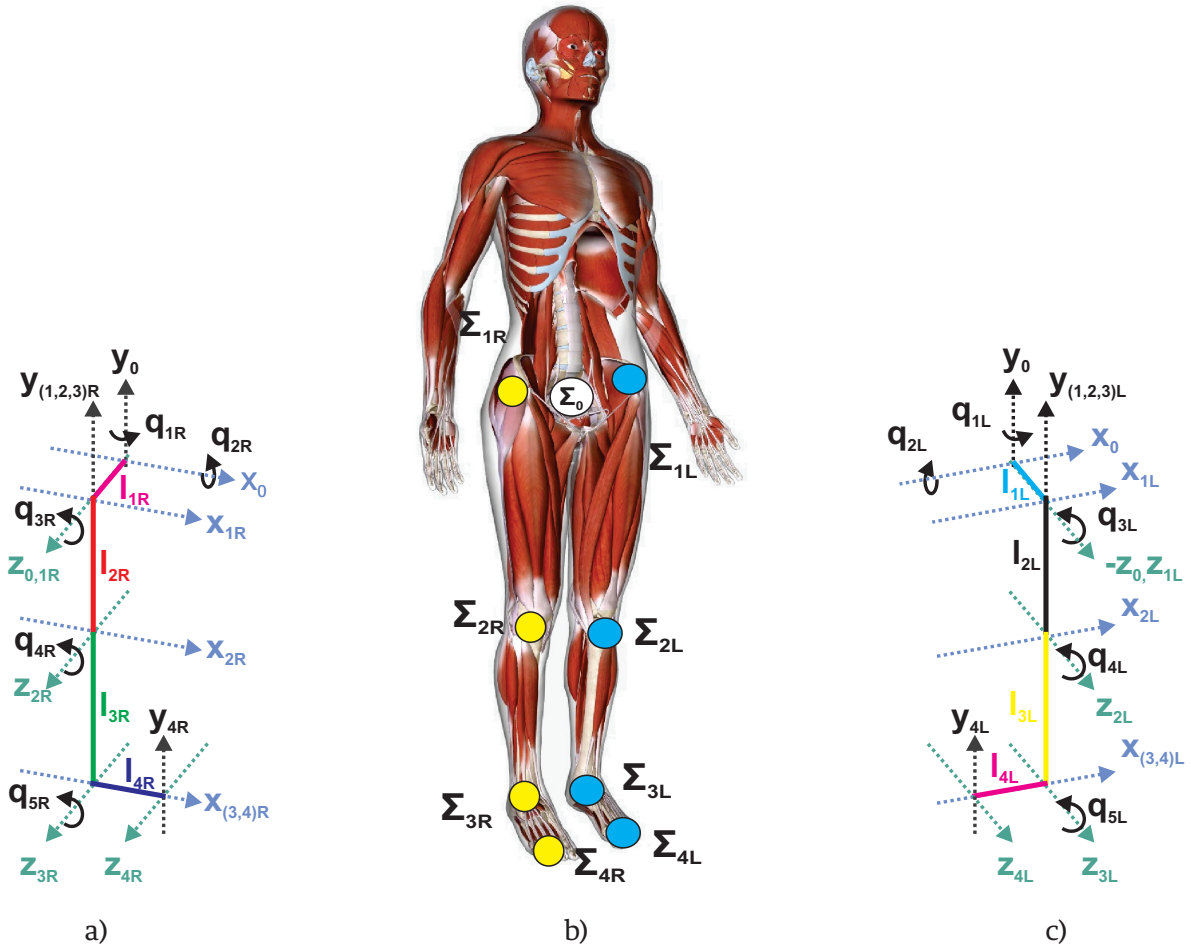

FIGURE 3. Proposed kinematic chain representing the frames that define the movements of the joined system for gait modeling. a) Lower right limb, b) Correspondence of the frames and reference points in the female musculoskeletal model [27] and c) Lower left limb.

the quaternions representing rotations with angles q_{2R} and q_{3R} around z_{1R} and z_{2R} axes, respectively. $\boldsymbol{u_{2R}}$= [0, 0, 0, $\boldsymbol{k}$], $\boldsymbol{u_{3R}}$= [0, $\boldsymbol{i}$, 0, 0], $\boldsymbol{O\Sigma_{2R}}$= [0, 0, $l_{2R}\boldsymbol{j}$, 0] and $\boldsymbol{O\Sigma_{3R}}$= [0, l_{3R} $\boldsymbol{i}$, 0, 0], then, in a recursive form the final position daring the gait cycle of the right could be written as

$$\begin{aligned}\boldsymbol{O\Sigma_{3Rf}} = \; & Q_{1R}\,\boldsymbol{O\Sigma_{1R}}\,\overline{Q_{1R}} \; + \\ & Q_{1R}\,Q_{2R}\,\boldsymbol{O\Sigma_{2R}}\,\overline{Q_{2R}}\,\overline{Q_{1R}} \; + \\ & Q_{1R}\,Q_{2R}\,Q_{3R}\,\boldsymbol{O\Sigma_{3R}}\,\overline{Q_{3R}}\,\overline{Q_{2R}}\,\overline{Q_{1R}}\end{aligned} \tag{15}$$

For example, for a specific case where q_{1R}= q_{2R}= q_{3R}= 0, l_{1R}= l_{2R}= l_{3R}= 1 and β_{1R}= β_{2R}= β_{3R}= 0 we get $\boldsymbol{O\Sigma_{3Rf}}$= [0, 2, -2$\boldsymbol{j}$, 1], which corresponds to the same result though geometric method and D-H convention.

Pelvis - hip - knee - ankle system (PHAK)

In this section, to improve the kinematic gait analysis, in addition to the movements of flexion-extension of hip and knee, as well as dorsiflexion and plantarflexion of ankle [11] [12] [20] [26], rotational and tilting movements of the pelvis are added to the previous model (Figure 2). The two lower limbs are simultaneously considered as open serial kinematic chains and the reference frames are reassigned as shown in (Figure 3). For this reason, it is possible to calculate the forward kinematics of position of the joints and big toes of both lower limbs using the previously described methods. However, geometric methods and classical D-H convention become more complex as degrees of

freedom increase [16] as in this model. While the quaternion-based method presented as following, represents a flexible and precise tool for this approach.

In system PHAK (Figure 3), the model features the lower limbs as 7 rigid-body segments 1) pelvis, 2) right femur, 3) left femur, 4) right tibia, 5) left tibia, 6) right foot and 7) left foot. The relative motion of these segments is defined successively by quaternions algebra. The anthropometry is adopted from [20]. The cartesian frames Σ_0, Σ_1, Σ_2, Σ_3 and Σ_4 correspond to the references placed on pelvis, hip, knee, ankle and big toe, respectively, in both lower limbs. Let us define the origin of the cartesian frames as a quaternion as $\boldsymbol{O\Sigma_{1R}}$= [0, 0, 0, $l_{1R}\boldsymbol{k}$], $\boldsymbol{O\Sigma_{2R}}$= [0, 0, -$l_{2R}\boldsymbol{j}$, 0], $\boldsymbol{O\Sigma_{3R}}$= [0, 0, -$l_{3R}\boldsymbol{j}$, 0], $\boldsymbol{O\Sigma_{4R}}$= [0, $l_{4R}\boldsymbol{i}$, 0, 0]. The quaternions Q_{1R}, Q_{2R}, Q_{3R}, Q_{4R} and Q_{5R} with $\boldsymbol{u_{1R}}$= [0, 0, $\boldsymbol{j}$, 0], $\boldsymbol{u_{2R}}$=[0, $\boldsymbol{i}$, 0, 0], $\boldsymbol{u_{3R}}$= $\boldsymbol{u_{4R}}$= $\boldsymbol{u_{5R}}$= [0, 0, 0, $\boldsymbol{k}$], is the quaternions representation of the rotation and tilting movements of the pelvis, flexo-extension of hip and ankle, as well as dorsiflexion and plantarflexion of ankle, respectively. Finally, l_{1R}, l_{2R}, l_{3R} and l_{4R}, are related with the lengths of pelvis, femur, tibia and foot. Thus, recursively the position of the right big toe is calculated from Equation (11) as

$$\begin{aligned}\mathbf{O\Sigma_{4Rf}} = {} & Q_{1R}\,Q_{2R}\,\mathbf{O\Sigma_{1R}}\,\overline{Q_{2R}}\,\overline{Q_{1R}} + \\ & Q_{1R}\,Q_{2R}\,Q_{3R}\,\mathbf{O\Sigma_{2R}}\,\overline{Q_{3R}}\,\overline{Q_{2R}}\,\overline{Q_{1R}} + \\ & Q_{1R}\,Q_{2R}\,Q_{3R}\,Q_{4R}\,\mathbf{O\Sigma_{3R}}\,\overline{Q_{4R}}\,\overline{Q_{3R}}\,\overline{Q_{2R}}\,\overline{Q_{1R}} + \\ & Q_{1R}\,Q_{2R}\,Q_{3R}\,Q_{4R}\,Q_{5R}\,\mathbf{O\Sigma_{4R}}\,\overline{Q_{5R}}\,\overline{Q_{4R}}\,\overline{Q_{3R}}\,\overline{Q_{4R}}\,\overline{Q_{1R}}\end{aligned} \tag{16}$$

Similarly, the position of the left big toe could be calculated and expressed as:

$$\begin{aligned}\mathbf{O\Sigma_{4Lf}} = {} & Q_{1L}\,Q_{2L}\,\mathbf{O\Sigma_{1L}}\,\overline{Q_{2L}}\,\overline{Q_{1L}} + \\ & Q_{1L}\,Q_{2L}\,Q_{3L}\,\mathbf{O\Sigma_{2L}}\,\overline{Q_{3L}}\,\overline{Q_{2L}}\,\overline{Q_{1L}} + \\ & Q_{1L}\,Q_{2L}\,Q_{3L}\,Q_{4L}\,\mathbf{O\Sigma_{3L}}\,\overline{Q_{4L}}\,\overline{Q_{3L}}\,\overline{Q_{2L}}\,\overline{Q_{1L}} + \\ & Q_{1L}\,Q_{2L}\,Q_{3L}\,Q_{4L}\,Q_{5L}\,\mathbf{O\Sigma_{4L}}\,\overline{Q_{5L}}\,\overline{Q_{4L}}\,\overline{Q_{3L}}\,\overline{Q_{2L}}\,\overline{Q_{1L}}\end{aligned} \tag{17}$$

Once the forward kinematics of the position of both lower limbs has been obtained, a simulation and visualization corresponding to the HAK (Figure 2) and PHAK (Figure 3) systems are carried out for the types of gait: i) normal, ii) mild crouch and iii) severe crouch. The computational implementation on Matlab® of the quaternions method to calculate the forward kinematics of position of the PHAK system is represented in the following flow chart (Figure 4). In the same way. the algorithm is applicable for the HAK system.

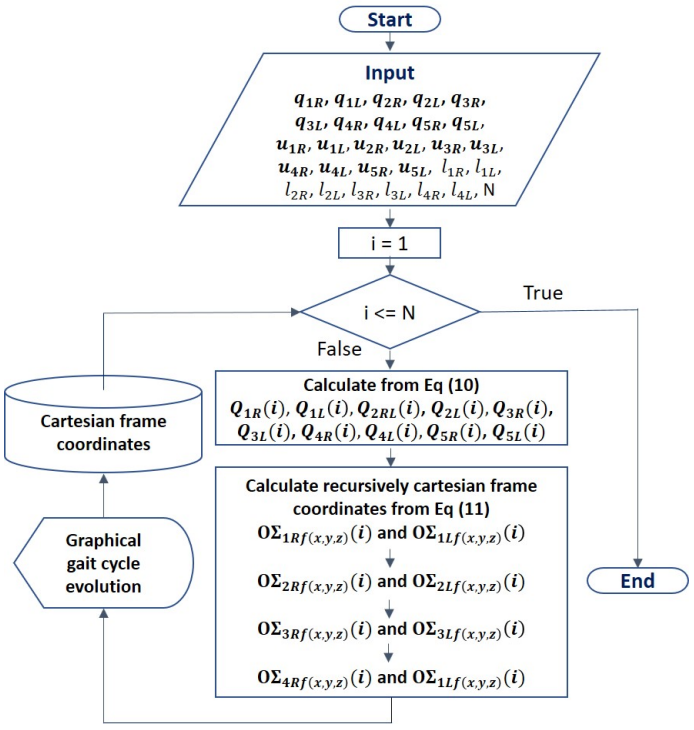

FIGURE 4. Flowchart for the computational implementation for the forward kinematics of position using quaternions algebra.

Where, the input data q_{1R}, q_{1l}, q_{2R}, q_{2L}, q_{3R}, q_{3L}, q_{4R}, q_{4l}, q_{5R}, q_{5l} are the values of the angles for rotation and tilt of the pelvis, flexo-extension of hip and knee, as well as, dorsiflexion and plantarflexion of the ankle, for both extremities, respectively. N is the number of samples per gait cycle. These values were adopted from de gait2392_simbody model [24] for each gait (Table 4). This model is a three-dimensional, 23-degree-of-freedom computer model of the human musculoskeletal system. While, l_{1R}, l_{1L}, l_{2R}, l_{2L}, l_{3R}, l_{3L}, l_{4R}, l_{4L}, pelvis, femur, tibia and foot anthropometry was adopted from [20]. The proposed method in this work allows a flexible and transparent coupling of the joint angles

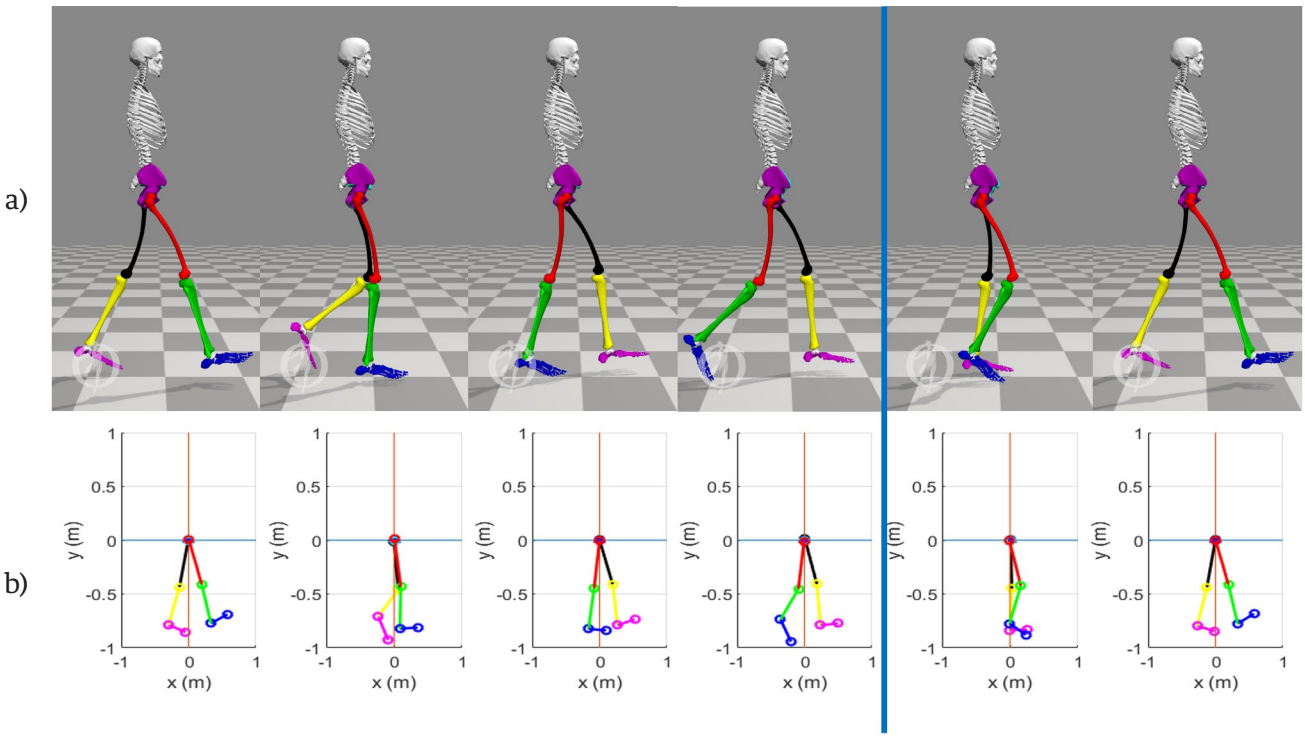

FIGURE 5. View in the sagittal plane of 6 states of the kinematics of the lower limbs in (0, 20, 40, 60, 80 y 100) % of the normal gait cycle. a) Biomechanical simulation platform [24] and b) Quaternions-algebra based platform.

and anthropometry to determine the forward kinematics of position. u_{1R}, u_{1L}, u_{2R}, u_{2L}, u_{3R}, u_{3L}, u_{4R}, u_{4L}, u_{5R}, u_{5L} were proposed according to the configuration of the model in (Figure 3).

Next, iteratively for all the sampled of the gait, based on Equation (10), the quaternions that represent each corresponding movement are calculated. And sequentially from Equation (11), the positions of each joint reference are calculated.

Finally, for each iteration a graphic representation of the pattern of each type of gait in that corresponding sample can be made. The data of the cartesian positions of each joint are stored to be compared later.

RESULTS AND DISCUSSION

In this section, the most relevant results of this work are presented and described. Then, in order to present the movement pattern of the gait model [24]

TABLE 3. Movement models used from gait*2392_simbody.osim* [24].

Gait type	Movement model
Normal (N)	normal
Mild crouch (MC)	crouch1
Severe crouch (SC)	crouch4

(Figure 4a) and the one proposed in this work (Figure 4b), visualizations in the sagittal plane of 6 states (0, 20, 40, 60, 80, and 100) % of a normal gait cycle for both methods are shown. The values of the angles and anthropometry used are those described in the previous section. To highlight part of the contribution of this work, we include the visualization of the same states and conditions for the same gait for the frontal plane (Figure 5) and the superior transverse plane (Figure 6), in which it is possible to appreciate rotating and tilting movements of the pelvis, respectively. These movements have been included in this

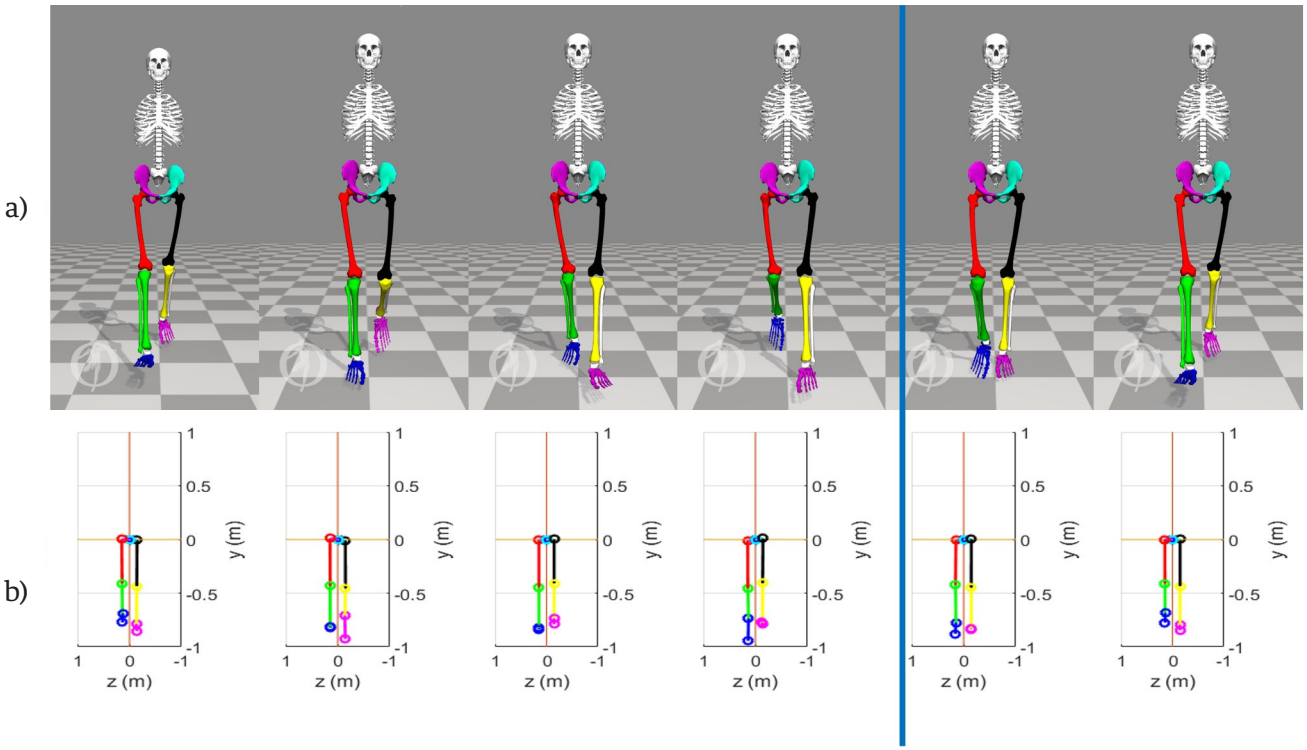

FIGURE 6. **View in the frontal plane of 6 states of the kinematics of the lower limbs in (0,20,40,60,80 y 100) % of the normal gait cycle. a) Biomechanical simulation platform [24] and b) Quaternions-algebra based platform.**

work unlike others that have not, which substantially improves the precision in the calculation of the kinematics of the lower limbs.

For the computational implementation in our approach the base frame Σ_0 is considered in an absolute way, that is, the translational movement of the pelvis has not been considered. The blue vertical line in (Figures 5, 6 and 7) indicates the end of the stance phase (60% of the cycle) and the beginning of the swing phase (40% of the cycle).

In the 3 figures, the gait pattern generated by the mathematical quaternion-based model is similar to the OpenSim® biomechanical model [24], which is very important, since a more practical and less complex implementation can be done with the method based on quaternions than with the D-H convention. Furthermore, as it can be seen, it is possible to approximate the gait pattern of a 23 DoF model [24], with an 8 DoF model like the one proposed in this work, which implies the reduction of orthonormal frames and with it, the instrumentation required for the measurement joint variables are also simplified. In addition to the above, it is possible to model the lower extremities as an analytically open serial chain with quaternion algebra and simplify the fact of modeling each joint independently.

The most widely analyzed joints in the literature are the hip, knee and ankle. In crouched gaits, dorsiflexion and plantarflexion of the ankle are pronounced, on average more than 15° from normal gait. The crouch pattern is generally a problem presented by people with cerebral palsy [30] [31], as well as spastic diplegia and quadriplegia [32] [33]. Disability as a result of a cerebrovascular accident or other types of accident has an evolution that dominates from the stroke phase, immediately after the accident, to a phase of low to severe spasticity, due to the inattention of the patient

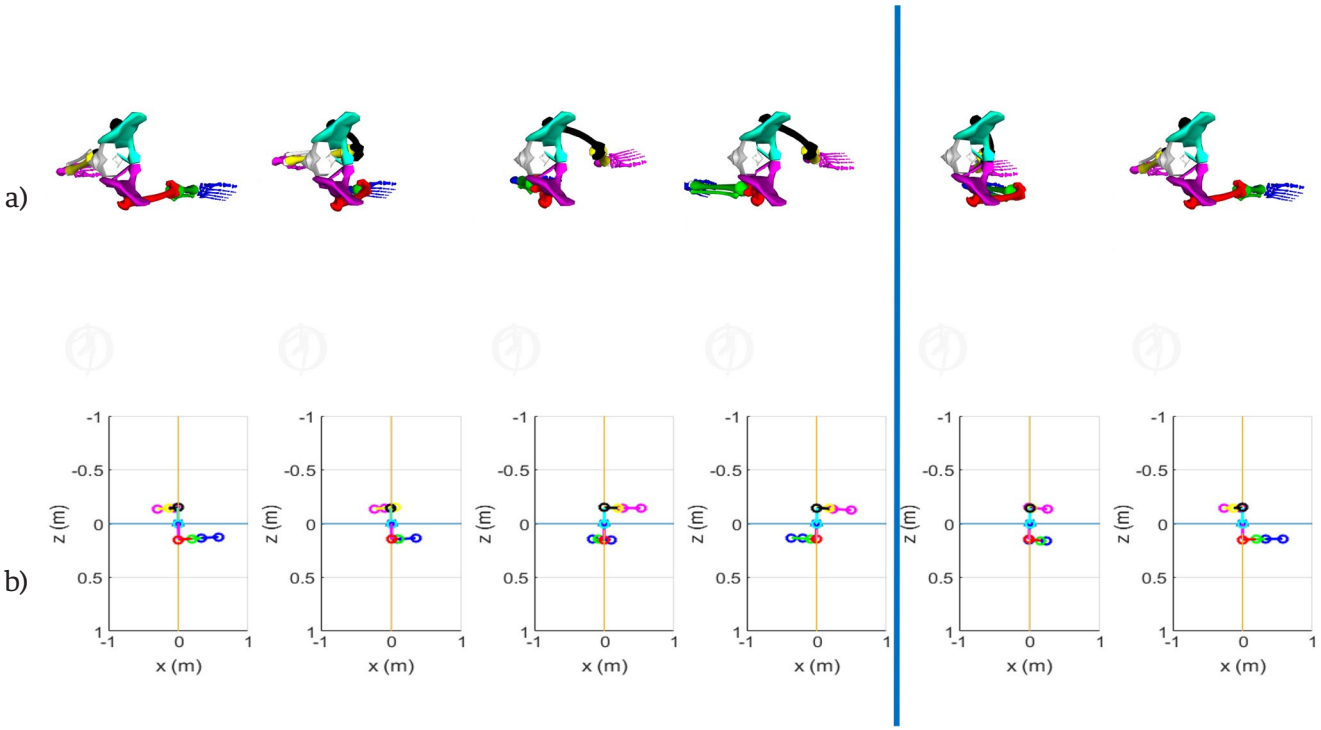

FIGURE 7. **View in the transverse plane of 6 states of the kinematics of the lower limbs in (0,20,40,60,80 y 100) % of the normal gait cycle. a) Biomechanical simulation platform [24] and b) Quaternions-algebra based platform.**

in tasks of rehabilitation. The diseases are the same, the level of progress that makes the disease critical, changes over time to worsen or improve. Therefore, the analysis of the variation of the angular amplitude, maximum and minimum points of occurrence and shape factor of the angles of the joints is extremely important to determine the evolution of a patient in conditions of disability.

In addition to the joint and geometric parameters of the lower limbs, the calculation of the forward kinematics of position of the hip, knee, ankle and big toe of the right (Figure 8) and left (Figure 9) lower limbs is very important for gait analysis.

In (Figure 8) and (Figure 9), the positions of the reference frames of the hip, knee, ankle and big toe in the sagittal plane for each limb, respectively, provide information on the behavior in the operational space of the gait. It is possible through these graphs to determine the differences between a normal gait and pathological gaits in relation to the range of motion and shape factor. Which is very useful in the clinical diagnosis and in the treatments related to gait problems.

In (Figure 8a), regarding the positions of the hip frames, it is observed that for a normal gait, both the right and the left move around the origin (z axis), while in the abnormal gaits the centers of position shift .02 m, and 08m for mild crouch and severe crouch, respectively. In addition to highlighting the shape pattern, which makes evident a flexion in the hip for abnormal gaits. The joints have the same shape pattern for the 3 types of gait and only a decrease in movement of approximately 40% is observed. However, the same does not occur for the left limb, since the movement factor is far between normal gait and abnormal gait, in which the severity of gait increases, thereby decreasing the movement in the operational space.

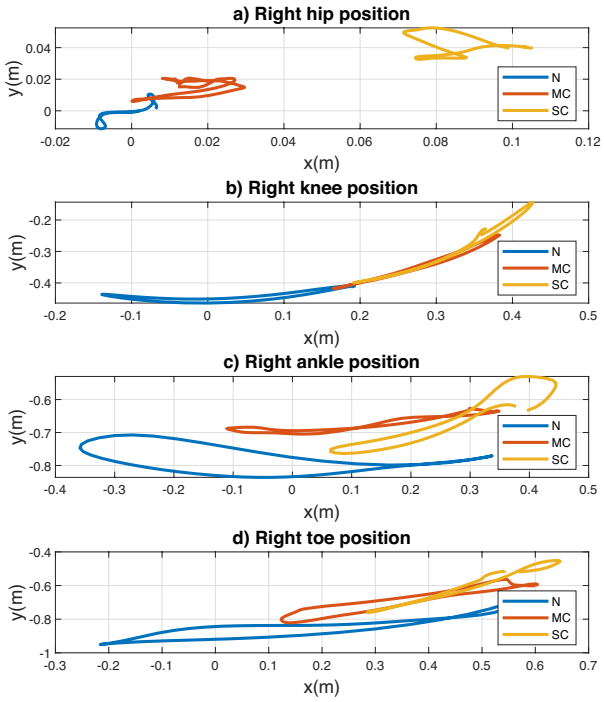

FIGURE 8. a) Hip, b) Knee, c) Ankle and d) Big toe, right positions in the sagittal plane during gaits: normal (N), mild crouch (MC) and severe crouch (SC), using the quaternion-based approach.

Conventional methods establish a gait analysis from the comparison of the gait pattern associated with each bone structure in its corresponding anatomical plane with the performance of the studied subject. This activity represents exhaustive work to establish a diagnosis, particularly when the performance of one bone structure depends on some other (in the same lower extremity or the other). However, analyzing performance globally significantly reduces analysis time, particularly when running in operational space or gait space; thus, being possible to evaluate classical metrics, and other proposals that better describe the anomaly.

The position of the joints is useful to improve the anatomical models or attachments that help to walk. Likewise, obtaining the position by forward kinematics, the cadence can be obtained from the calculation of the angular velocity, which cannot be obtained from the joint space. Also, through forward kinematics it is possible to obtain the distance between the joints during the gait cycle and from there determine the dependency that exists between them. Therefore, using metrics such as these, through these comparative metrics, it is possible to contribute to diagnosis and decision-making.

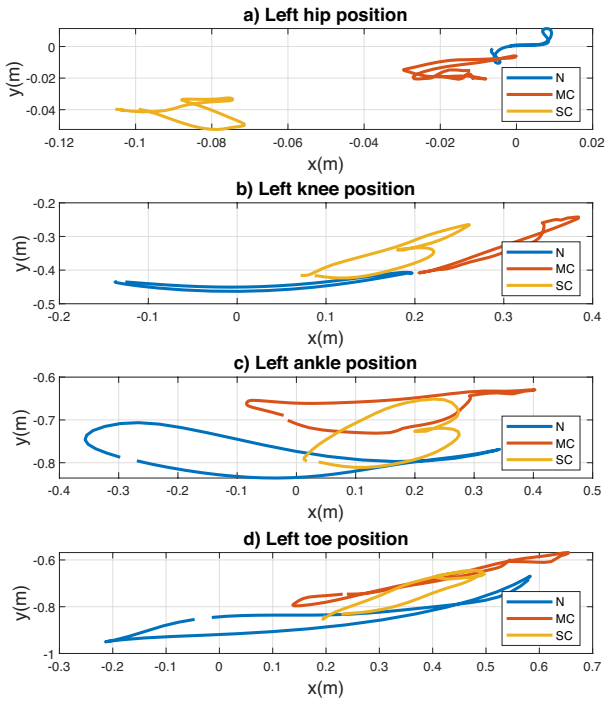

FIGURE 9. a) Hip, b) Knee, c) Ankle and d) Big toe, left positions in the sagittal plane during gaits: normal (N), mild crouch (MC) and severe crouch (SC), using the quaternion-based approach.

The use of specific metrics to develop the biomechanical analysis of gait depends on the objective of interest. Generally, these metrics are used to determine age, gender, pathologies [34] or physiotherapeutic progress [35].

The most common metrics used in gait analysis are speed, cadence, stride length, toe angle, number of daily steps [23]. There are some less used ones based on the calculation of the area of the silhouette to determine gender [36]. This represents an area of opportunity to study and propose new metrics evaluated in the operational space. While the Euclidean distance is the

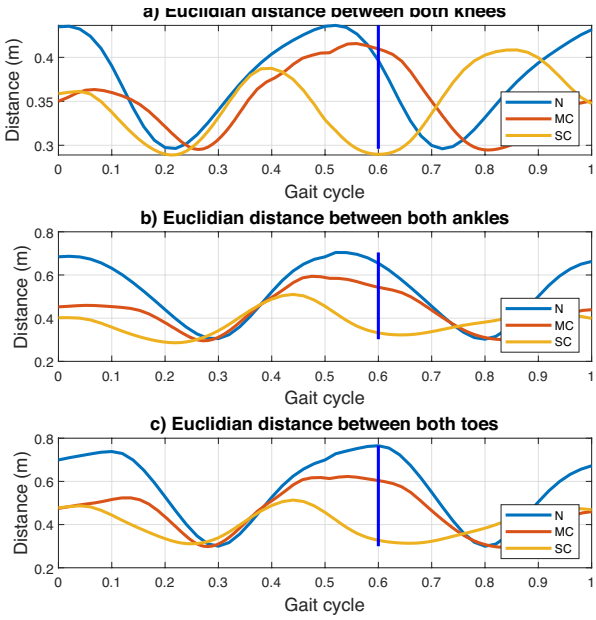

FIGURE 10. Euclidean distance between a) knees, b) ankles, and c) big toes of the lower limbs during normal (N), mild crouch (MC) and severe crouch gaits.

usual norm used in cartesian space, for human gait analysis, it has not been reported as a useful metric. The Euclidean distance between orthonormal frames of the joint references (Figure 3) of lower limbs is shown in (Figure 10) and is calculated as

$$\overline{O\Sigma_{2R}\,O\Sigma_{2L}} = \sqrt{\begin{matrix}(O\Sigma_{2Rx} - O\Sigma_{2Lx})^2 + \cdots \\ (O\Sigma_{2Ry} - O\Sigma_{2Ly})^2 + (O\Sigma_{2Rz} - O\Sigma_{2Lz})^2\end{matrix}} \tag{18}$$

for the distance between the knees, while

$$\overline{O\Sigma_{3R}\,O\Sigma_{3L}} = \sqrt{\begin{matrix}(O\Sigma_{3Rx} - O\Sigma_{3Lx})^2 + \cdots \\ (O\Sigma_{3Ry} - O\Sigma_{3Ly})^2 + (O\Sigma_{3Rz} - O\Sigma_{3Lz})^2\end{matrix}} \tag{19}$$

and

$$\overline{O\Sigma_{4R}\,O\Sigma_{4L}} = \sqrt{\begin{matrix}(O\Sigma_{4Rx} - O\Sigma_{4Lx})^2 + \cdots \\ (O\Sigma_{4Ry} - O\Sigma_{4Ly})^2 + (O\Sigma_{4Rz} - O\Sigma_{4Lz})^2\end{matrix}} \tag{20}$$

are used to calculate the euclidian distance between ankles and big toes, respectively.

The use of the metric of the Euclidean distance in the cartesian space of the gait allows to establish a distance pattern to determine the normal and abnormal parameters during the evaluation and it is related to the range of motion of each joint. The distance between the right and left hip references due to the human model used is kept constant and for this reason is not presented in (Figure 10). The distance between knees references during normal gait is greater for each gait sample than mild and severe crouch gaits, which implies that the global performance in abnormal gaits reflects a limitation of movement, which is characteristic of diseases such as cerebral palsy or hemiplegia. On the other hand, the form factor of the distance measurement of normal gait references can be established as the gait pattern in cartesian space, so it is clear that in (Figure 10a) the abnormal gaits do not maintain the same distance between knees as the pattern. Similar performance in measuring the Euclidean distance between the ankles and the big toes of both lower limbs.

CONCLUSIONS

Unlike classical Denavit-Hartenberg and geometric methods for calculating the forward kinematics of position of a serial kinematic chain, the method based on quaternion algebra proposed in this work reduces the complexity of kinematic modeling and the computational cost of numerical calculation when the number of degrees of freedom of the chain increases. Furthermore, through the method introduced, it is possible to approximate the gait pattern of the 23 DoF human model, through the 8 DoF model used in this work, reducing the number of orthonormal frames in the modeling and instrumentation required for the acquisition of biomechanical data of the gait.

The analysis in the 3 anatomical planes of the 8 DoF model allows an evaluation of the performance of the lower limb joints during the gait cycle both, independently and as a whole. If the movements of the joints in a single anatomical plane are evaluated, as for

example in the 3 DoF model presented, a local analysis is obtained, which does not consider the movements in other anatomical planes that limit the comprehensive diagnosis, and there may be loss of an objective diagnosis.

Finally, gait analysis in the cartesian space from the joint space is useful to assess gait abnormalities of the studied subject with respect to the normal gait pattern. The evaluation in the operational space of abnormal gaits, such as mild crouch and severe crouch respect to normal gait, shows an anatomical displacement of excessive flexion in the knees and ankles presented in this type of gait, noted numerically through the proposed model. In addition, it is possible to determine the normal patterns and metrics of these and other joints such as the hip, which help diagnose diseases related to the detected abnormalities. The use of other metrics in cartesian space, the calculation of inverse kinematics, and differential kinematics can greatly improve the biomechanical gait analysis.

ETHICAL STATEMENT

The authors declare that they have no potential conflicts of interest regarding the research, authorship and / or publication of the article.

AUTHOR CONTRIBUTIONS

J.C.G.I. Contributed to the state-of-the-art analysis, numerical methods associated to direct position kinematic modelling in robotic systems, numerical algorithms programming in Matlab for virtual visualization of the gait space, mapping and interpretation of the gait space (operational) and the anatomic space (articular), mathematical formulation base in quaternion theory. Writing of the final manuscript. O.A.D.R. Contributed to the mathematical analysis and modelling based on the theory of quaternion algebra from a bio-robotic point-of-view, with a vision in the application of metrics for the diagnosis associated with healthy and anomalous gait, writing and review of the different sections of the manuscript. Analysis and test of convergence of the proposed numerical method related to classic procedures, definition of a vision of the quaternion differential kinematic defining cadence and quaternionic inverse kinematic. O.L.O. participated in the state-of-the-art analysis, writing and reviewed the manuscript, numerical validation of the algorithm for the direct kinematics of position between bone limbs and database management on reliable sources associated to healthy and anomalous gait. All authors agree with all the contents and approved the final version of the manuscript.

SUPPLEMENTARY MATERIAL

Visualizations of the positions of the lower limbs during the gait cycle in the cartesian space using the proposed method in this work and OpenSim®, in the three anatomical planes of normal, mild crouch and, severe crouch gaits are shown at:

https://youtu.be/frCdRDTfLz4

REFERENCES

[1] Klöpfer-Krämer I, Brand A, Wackerle H, Müßig J, Kröger I, Augat P. Gait analysis - Available platforms for outcome assessment. Injury [Internet]. 2019;2:90-6. Available from: https://doi.org/10.1016/j.injury.2019.11.011

[2] Correa-Bautista F. Análisis de marcha en pacientes con hemiplejia desde un punto de vista Bio-robótico [Master's thesis]. [Distrito Federal]: Instituto Politécnico Nacional, 2011. 294p.

[3] Munteanu SE, Barton CJ. Lower limb biomechanics during running in individuals with achilles tendinopathy: A systematic review. J Foot Ankle Res [Internet]. 2011;4(1). Available from: https://doi.org/10.1186/1757-1146-4-15

[4] Willems T, Witvrouw E, Delbaere K, De Cock A, De Clercq D. Relationship between gait biomechanics and inversion sprains: A prospective study of risk factors. Gait & Posture [Internet]. 2005;21(4):379-87. Available from: https://doi.org/10.1016/j.gaitpost.2004.04.002

[5] Morris M, Iansek R, McGinley J, Matyas T, Huxham F. Three-dimensional gait biomechanics in Parkinson's disease: Evidence for a centrally mediated amplitude regulation disorder. Mov Disord [Internet]. 2005;20(1):40-50. Available from: https://doi.org/10.1002/mds.20278

[6] Beaulieu ML, Lamontagne M, Beaulé PE. Lower limb biomechanics during gait do not return to normal following total hip arthroplasty. Gait & Posture [Internet]. 2010;32(2):269-73. Available from: https://doi.org/10.1016/j.gaitpost.2010.05.007

[7] Levinger P, Menz HB, Morrow AD, Feller JA, Bartlett JR, Bergman NR. Lower limb biomechanics in individuals with knee osteoarthritis before and after total knee arthroplasty surgery. J Arthroplasty [Internet]. 2013;28(6):994-999. Available from: https://doi.org/10.1016/j.arth.2012.10.018

[8] Schmid S, Studer D, Hasler CC, Romkes J, Taylor WR, Lorenzetti S, et al. Quantifying spinal gait kinematics using an enhanced optical motion capture approach in adolescent idiopathic scoliosis. Gait & Posture [Internet]. 2016;44:231-7. Available from: https://doi.org/10.1016/j.gaitpost.2015.12.036

[9] Kitade I, Nakajima H, Takahashi A, Matsumura M, Shimada S, Kokubo Y, et al. Kinematic, kinetic, and musculoskeletal modeling analysis of gait in patients with cervical myelopathy using a severity classification. Spine J [Internet]. 2020;20(7):1096-1105. Available from: https://doi.org/10.1016/j.spinee.2020.01.014

[10] Mirelman A, Patritti BL, Bonato P, Deutsch JE. Effects of virtual reality training on gait biomechanics of individuals post-stroke. Gait & Posture [Internet]. 2010;31(4):433-7. Available from: https://doi.org/10.1016/j.gaitpost.2010.01.016

[11] Bharatkumar AG, Daigle KE, Pandy MG, Cai Q, Aggarwal JK. Lower limb kinematics of human walking with the medial axis transformation. In: Proceedings of 1994 IEEE Workshop on Motion of Non-rigid and Articulated Objects [Internet]. Austin: IEEE; 1994:70-6. Available from: https://doi.org/10.1109/MNRAO.1994.346252

[12] Delahunt E, Monaghan K, Caulfield B. Changes in lower limb kinematics, kinetics, and muscle activity in subjects with functional instability of the ankle joint during a single leg drop jump. J Orthop Res [Internet]. 2006;24(10):1991-2000. Available from: https://doi.org/10.1002/jor.20235

[13] Hamilton WR. Elements of quaternions. London: Longmans, Green, & Company; 1899. 583p.

[14] Cohen A, Shoham M. Hyper Dual Quaternions representation of rigid bodies kinematics. Mech Mach Theory [Internet]. 2020;150:103861. Available from: https://doi.org/10.1016/j.mechmachtheory.2020.103861

[15] Özgür E, Mezouar Y. Kinematic modeling and control of a robot arm using unit dual quaternions. Rob Auton Syst [Internet]. 2016;77:66-73. Available from: https://doi.org/10.1016/j.robot.2015.12.005

[16] Spong MW, Vidyasaga M. Robot Dynamics and Control. John Wiley & Sons Inc.; 1989. 352p.

[17] Reyes-Cortes F. Matlab aplicado a robótica y mecatrónica. Distrito Federal:Alfaomega; 2012. 457p.

[18] Cardona M, García Cena CE, Serrano F, Saltaren R. ALICE: Conceptual development of a lower limb exoskeleton robot driven by an on-board musculoskeletal simulator. Sensors [Internet]. 2020;20(3):789. Available from: https://doi.org/10.3390/s20030789

[19] Khokar K, Beeson P, Burridge R. Implementation of KDL inverse kinematics routine on the atlas humanoid robot. Procedia Comput Sci [Internet]. 2015;46:1441-8. Available from: https://doi.org/10.1016/j.procs.2015.02.063

[20] Tadano S, Takeda R, Miyagawa H. Three dimensional gait analysis using wearable acceleration and gyro sensors based on quaternion calculations. Sensors [Internet]. 2013;13(7):9321-43. Available from: https://doi.org/10.3390/s130709321

[21] Sabatini AM. Quaternion-based strap-down integration method for applications of inertial sensing to gait analysis. Med Biol Eng Comput [Internet]. 2005:94-101. Available from: https://doi.org/10.1007/BF02345128

[22] Piórek M, Josiński H, Michalczuk A, Świtoński A, Szczęsna A. Quaternions and joint angles in an analysis of local stability of gait for different variants of walking speed and treadmill slope. Inf Sci [Internet]. 2017;384:263-80. Available from: https://doi.org/10.1016/j.ins.2016.08.069

[23] Whittle M. An Introduction to Gait Analysis. Butterworth-Heinemann; 2006. 244p.

[24] Seth A, Hicks JL, Uchida TK, Habib A, Dembia CL, Dunne JJ, et al. OpenSim: Simulating musculoskeletal dynamics and neuromuscular control to study human and animal movement. PLoS Comput Biol [Internet]. 2018;14(7):1-20. Available from: https://doi.org/10.1371/journal.pcbi.1006223

[25] Radavelli LA, Simoni R, Pieri E De, Martins D. A Comparative Study of the Kinematics of Robots Manipulators by Denavit-Hartenberg and Dual Quaternion. In Cardona A, Kohan PH, Quinteros RD, Storti MA (eds.). Mecánica Comput [Internet]. Salta, Argentina: Asociación Argentina de Mecánica Computacional. 2012; XXXI: 2833-2848. Available from: https://cimec.org.ar/ojs/index.php/mc/article/view/4224

[26] Lu TW, Chen HL, Chen SC. Comparisons of the lower limb kinematics between young and older adults when crossing obstacles of different heights. Gait & Posture [Internet]. 2006;23(4):471-9. Available from: https://doi.org/10.1016/j.gaitpost.2005.06.005

[27] BioDigital I. Female Musculoskeletal System. BIODIGITAL [Internet]. 2020; Available from: *https://human.biodigital.com/*

[28] Hart JC, Francis GK, Kauffman LH. Visualizing Quaternion Rotation. ACM Trans Graph [Internet]. 1994;13(3):256-76. Available from: https://doi.org/10.1145/195784.197480

[29] Shoemake K. Animating rotation with quaternion curves. In: 12th annual conference on Computer graphics and interactive techniques [Internet]. New York: Association for Computing Machinery; 1985:19(3):245-54. Available from: https://doi.org/10.1145/325165.325242

[30] Arnold AS, Anderson FC, Pandy MG, Delp SL. Muscular contributions to hip and knee extension during the single limb stance phase of normal gait: A framework for investigating the causes of crouch gait. J Biomech [Internet]. 2005;38(11):2181-9. Available from: https://doi.org/10.1016/j.jbiomech.2004.09.036

[31] Steele KM, van der Krogt MM, Schwartz MH, Delp SL. How much muscle strength is required to walk in a crouch gait? J Biomech [Internet]. 2012;45(15):2564-9. Available from: https://doi.org/10.1016/j.jbiomech.2012.07.028

[32] Kedem P, Scher DM. Evaluation and management of crouch gait. Curr Opin Pediatr [Internet]. 2016;28(1):55-9. Available from: https://doi.org/10.1097/mop.0000000000000316

[33] Rodda JM, Graham HK, Nattrass GR, Galea MP, Baker R, Wolfe R. Correction of Severe Crouch Gait in Patients With Spastic Diplegia With Use of Multilevel Orthopaedic Surgery. JBJS [Internet]. 2006;88(12):2653-64. Available from: https://doi.org/10.2106/jbjs.e.00993

[34] Miodonska Z, Stepien P, Badura P, Choroba B, Kawa J, Derejczyk J, et al. Inertial data-based gait metrics correspondence to Tinetti Test and Berg Balance Scale assessments. Biomed Signal Process Control [Internet]. 2018;44(7):38-47. Available from: https://doi.org/10.1016/j.bspc.2018.03.012

[35] Ghent F, Mobbs RJ, Mobbs RR, Sy L, Betteridge C, Choy WJ. Assessment and Post-Intervention Recovery After Surgery for Lumbar Disk Herniation Based on Objective Gait Metrics from Wearable Devices Using the Gait Posture Index. World Neurosurg [Internet]. 2020;142:e111-6. Available from: https://doi.org/10.1016/j.wneu.2020.06.104

[36] Foster JP, Nixon MS, Prügel-Bennett A. Automatic gait recognition using area-based metrics. Pattern Recognit Lett [Internet]. 2003;24(14):2489-97. Available from: https://doi.org/10.1016/S0167-8655(03)00094-1

RESEARCH ARTICLE

Vol. 41 | No. 3 | **SEPTIEMBRE - DICIEMBRE 2020** | pp 72-86

REVISTA MEXICANA DE Ingeniería Biomédica

dx.doi.org/10.17488/RMIB.41.3.5

E-LOCATION ID: **1111**

Electrical Cochlear Response as an Objective Measure of Hearing Threshold and Hearing Performance Evaluation in Pediatric Cochlear Implant Users

Respuesta Coclear Eléctrica como Medida Objetiva del Umbral Auditivo y la Evaluación del Rendimiento Auditivo en Usuarios Pediátricos de Implante Coclear

A. K. Quintana-López[1], *N. E. Beltran-Vargas*[2], *M. P. Granados-Trejo*[3], *J. M. Cornejo-Cruz*[3]

[1]Universidad Autonoma Metropolitana, Posgrado en Ingeniería Biomédica

[2]Universidad Autonoma Metropolitana, Cuajimalpa

[3]Universidad Autonoma Metropolitana, Iztapalapa

ABSTRACT

The difficulties of applying the audiometry in pediatric populations and its methodological limitations in implanted patients have spurred the development of new alternative auditory evaluation methods. This study aimed to show an objective method to estimate hearing thresholds in pediatric cochlear implanted patients through Electrical Cochlear Response (ECR) and to quantify the hearing performance by using an Auditory Skills Questionnaire (ASQ) and a Calibrated Sounds Test (CST) designed on purpose. Eighteen implanted patients, 1-6 years old underwent standard audiometry, ECR, and ASQ in two evaluation sessions T1 and T2. At T2, in addition, patients underwent CST. For patients ≤3 years old (G1), Pure Tone Averages (PTA and PTA_{ECR})showed a statistically significant difference between them at T1 and T2. At T2 improvements in audiometric and ECR thresholds were observed ($p<0.05$), regarding T1. Patients older than 3 years (G2) had significantly better ASQ and CST scores. CST detection scores at 40 dB_{HL} for groups G1 and G2, 36% and 70% respectively, showed a better relationship to ECR thresholds. The relationship observed between ECR thresholds and CST detection scores seems to confirm that ECR brings the feasibility of objective hearing threshold estimation and provides a better frequency resolution than audiometry.

KEYWORDS: electro-acoustic test; frequency specificity; intensity calibrated sounds; hearing performance

RESUMEN

Las dificultades para la aplicación de la audiometría en la población pediátrica además de sus limitaciones metodológicas en pacientes usuarios de implante coclear, señalan la necesidad de métodos audiométricos alternos. En el presente trabajo se utiliza el potencial eléctrico, denominado Respuesta Coclear Eléctrica (ECR) observado solamente en usuarios de implante coclear, para la estimación de umbrales auditivos prescindiendo de la participación consiente del paciente, además de evaluar el desempeño auditivo mediante un Cuestionario de Habilidades Auditivas (ASQ) y la Prueba de Sonidos Calibrados (CST). A dieciocho participantes de 1 a 6 años, se les practicó Audiometría, ECR y ASQ en dos sesiones, T1 y T2; adicionalmente, en T2 se aplicó CST. En T1 y T2 los promedios de tonos puros, PTA y PTA_{ECR}, de pacientes ≤ 3 años (G1), mostraron una diferencia estadísticamente significativa entre ellos. En T2 los umbrales audiométricos y ECR ($p < 0.05$), mejoraron respecto de T1. Pacientes > 3 años (G2) lograron puntuaciones ASQ y CST significativamente mejores. Los puntajes de detección CST a 40 dB_{HL}, G1(36%) y G2(70%), mostraron mejor relación con los umbrales ECR. Esta relación entre los umbrales ECR y los puntajes de detección CST indican que la ECR permite estimar el umbral de audición, logrando adicionalmente mayor resolución en frecuencia que la audiometría.

KEYWORDS: prueba electro-acústica; especificidad en frecuencia; sonidos calibrados en intensidad; desempeño auditivo

Corresponding author

TO: Nohra Elsy Beltrán Vargas

INSTITUTION: Universidad Autónoma Metropolitana, Cuajimalpa

ADDRESS: Vasco de Quiroga #4871, Col. Santa Fé, Del. Cuajimalpa de Morelos, C. P. 05348, CDMX, Ciudad de México, México

E-MAIL: nbeltran@cua.uam.mx

Received:

20 August 2020

Accepted:

09 December 2020

INTRODUCTION

Today, a technological alternative for patients suffering from profound bilateral sensorineural hearing loss is the cochlear implant (CI) which, based on banded spectrum analysis for extraction of significant voice attributes, obtains an electrical stimulation code which, applied to the patient's hearing system, generates an auditory sensation. The FDA (Food and Drug Administration) recommends using CI in children from 12 months of age, due to the difficulty of performing behavioral hearing tests in younger patients. This is a limitation when seeking successful rehabilitation in the implanted patients, considering that the critical period for language acquisition comprises the first years of life [1] [2] [3].

Four to six weeks following implant surgery, CI is programmed for the first time, starting the process of customizing the device to the patient's needs, in order to achieve useful, safe, and comfortable hearing. The different parameters involved in CI programming include establishing the dynamic range of electrical stimulation current in each intracochlear electrode, delimited by the minimum (T) and maximum (M) levels corresponding to the threshold and maximum tolerable auditory sensation, respectively [4]. In clinical practice these current levels are determined by observing the patient's auditory behavior in response to the electrical stimulation provided for a limited number of electrodes. This behavioral CI fitting can be more difficult in pediatric patients who lack the communication skills needed to obtain reliable feedback information.

This scenario has led to the use of electrophysiological methodologies such as Brainstem Auditory Evoked Potentials (BAEPs) [5] [6], the Electric Stapedial Reflex Threshold (ESRT) [7] [8] [9] [10], and the Electrically-Evoked Compound Action Potential (ECAP) [5] [9] [10] [11], to estimate T and M current levels for the electrode array. Of these methodologies, ECAP is the most used because it can be recorded for selected electrodes during or after implantation surgery [12].

Unfortunately, neither ECAP nor other electrophysiological methodologies mentioned previously, allow the estimation of hearing thresholds. The audiometry is the only clinical test available to determine hearing thresholds for a number of standardized frequencies [13] [14] [15] [16], which requires the conscious participation of the patient.

Audiometry results are reliable in patients older than 4 years old, while in younger patients it is difficult to perform because they frequently do not present perceptible behavioral changes. It is even more difficult to observe the changes in implanted patients, especially in their first CI programming session because they are not familiar with the use of the device [17].

Furthermore, standard audiometry was not originally designed for implanted users. Test standardized frequencies set does not consider the band pass filter number for the spectral analysis that CI sound processor performs on the external input sound. The number of the band pass filter depends on the number of active electrodes and the IC manufacturer. Therefore, if any audiometry test frequency fall outside the band-pass filter bandwidth, corresponding to a certain intracochlear electrode, the hearing threshold may not be evaluated correctly.

Despite audiometry application difficulties and limitations in implanted pediatric patients, this test is used as a guide to readjust stimulation current level in the intracochlear electrode array, in order to lead the patient from an auditory status equivalent to profound deafness to normal hearing. The methodological limitations to determine the optimal M and T current levels across the electrode array, by using electrical stimulation tests like ECAP, as well as the difficulties in estimating the hearing thresholds due to the adjustment of the current levels, especially in pediatric patients, has generated the need to develop new alternative methods to evaluate hearing.

Our research group at the Metropolitan Autonomous University (UAM) Audiology Laboratory has developed a test called Electrical Cochlear Response (ECR) [18], as an alternative method for hearing threshold estimation in implanted pediatric patients. ECR measures the electrical response of the auditory nerve due to electric stimulation every time CI processes an incoming external sound. The ECR considers the auditory nerve portion responsiveness to the electrical current involved with each intracochlear electrode. For a given dynamic range of electrical current in an intracochlear electrode, ECR allows establishing the minimum sound intensity level for which auditory nerve portion near to intracochlear electrode generates a threshold electrical response.

Through individual electrode current adjusting, ECR test can help to estimate the auditory threshold at each of the intracochlear electrodes. This is done by quantifying the change in amplitude of the ECR due to variations in the sound intensity level of the input sound.

Previous ECR results have shown that the activation profile of the intracochlear electrodes follows the audiometric threshold profile [19]. These results have shown the feasibility of estimating the patient's hearing thresholds based on ECR, which is independent of the age, general health condition, previous time of use, or brand of the CI.

On the other hand, considerable efforts have been made in the clinical field to establish an auditory-verbal rehabilitation program for pediatric CI users, by using a standardized set of tests that include questionnaires about child' hearing abilities development, and evaluation of speech and sounds discrimination [20] [21]. However, up to now, there are no standardized methodologies to quantify the patient's hearing performance during the period of adaptation to the device.

The purpose of this work is to show the use of ECR to estimate hearing thresholds in implanted pediatric patients and to evaluate hearing performance through the application of a set of tests designed to assess the patient's hearing abilities (see Table 1).

MATERIALS AND METHODS

Population

We included a group of 25 pre-lingual CI users between 1.4-6.6 years of age, who underwent CI surgery at the National Institute of Rehabilitation (INR), in Mexico City. Patients were diagnosed with bilateral profound sensorineural deafness and used hearing aids for at least six months previous to implantation surgery. All patients had a full insertion of the electrode array. Patients with neurological disease or ossified cochlea, and those without audiometry were excluded. Patients who did not complete the follow-up period were eliminated. The patient's parents accepted to wake up their children around 10 hours before ECR test. Ethical Research Committee of INR approved and supervised the study complied with all applicable research and ethical standards and laws followed by the Declaration of Helsinki principles. All patients' parents signed informed consent.

Two evaluation sessions were considered, T1: 1.5 to 9 months after CI implantation, and T2: 7 months after T1. The Figure 1 shows a flow diagram of the procedure used for patient´s hearing evaluation in each session.

Tests

Tests were performed at the INR audiology service in a 2.5x2.5x3.0 m audiometric test booth. The free field was calibrated according to ISO 389-7 Standard using a B&K 2235 sound meter, B&K 1625 filter, and a B&K 4230 microphone calibrator. The free field audiometry and ECR test were obtained in two different and successive days. Audiometry was performed using an *Interacoustics* clinical audiometer AC-40, while the

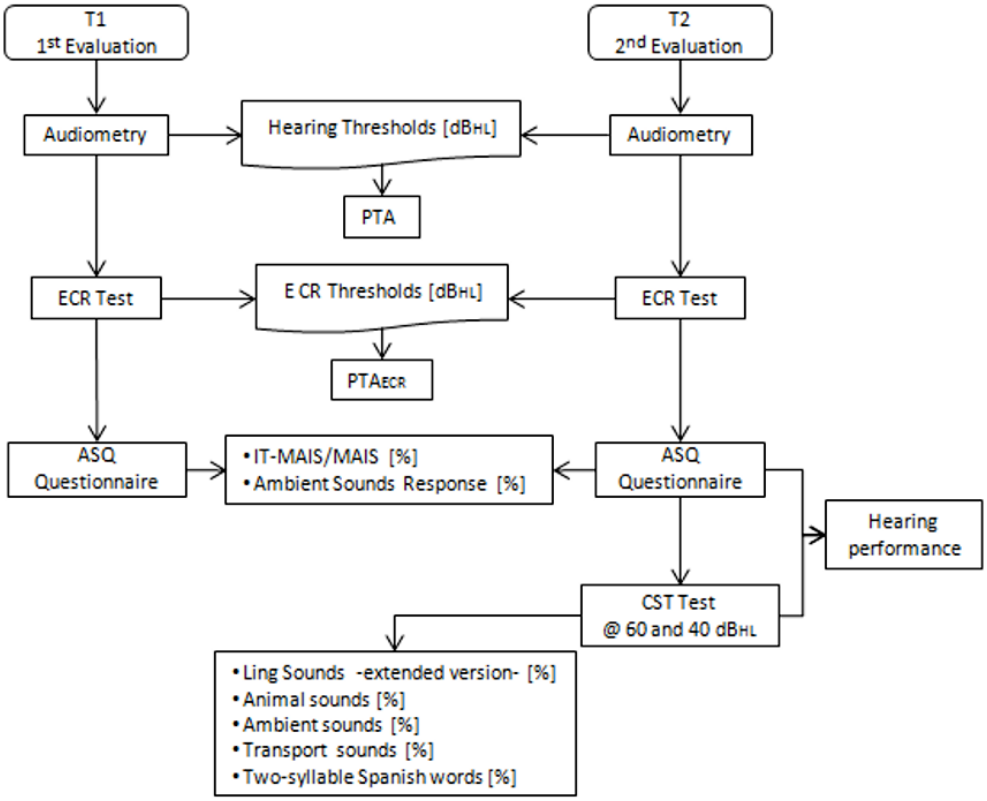

FIGURE 1. Flow diagram procedure used for patient´s hearing evaluation in T1 and T2 sessions.

patient was wearing the CI, seated a meter away from the loudspeaker. Pure Tone Average (PTA) was calculated in the frequency range of 500 to 2000 Hz to determine the patient's hearing level [15].

A prototype of ECR Monitor developed by the UAM Audiology Laboratory jointly with the company Innovamedica was used to obtain ECR. The prototype consists of one module to generate and reproduce sound stimuli, and other to acquire EEG, and a PC platform with software which synchronizes and organizes the acquisition of EEG with the reproduction of the stimuli (Figure 2).

Two recording EEG channels with A1(-), A2(-), Cz(+) and FPz(GND) according to 10-20 system [22], observing an electrode-skin impedance < 5 kΩ at 100 Hz were used. One hundred 50 ms EEG epochs were averaged, previously filtered with a second-order Butterworth low-pass filter of 0.1 to 300 Hz with cutoff slope of 12 dB/Octave, zero phase, ±10 μV artifact rejection window, and a sampling frequency of 20 kHz.

The waveform of ECR response (*) is shown in Figure 2 for a stimulation tone pip of 1278 Hz (central frequency assigned to the intracochlear electrode number eight). The increase in the ECR amplitude and the decrease in latency are due to the increase in the intensity of the tone pip. The ECR threshold is defined as the minimum intensity for robust ECR detection.

During the ECR test the patient remained asleep on a cot with the head facing a loudspeaker positioned at a distance of one meter, with CI operating under everyday usage conditions, according to the CI programming parameters previously defined by the audiologist. The test was performed in the presence of the patient's parents and supervised by the audiologist.

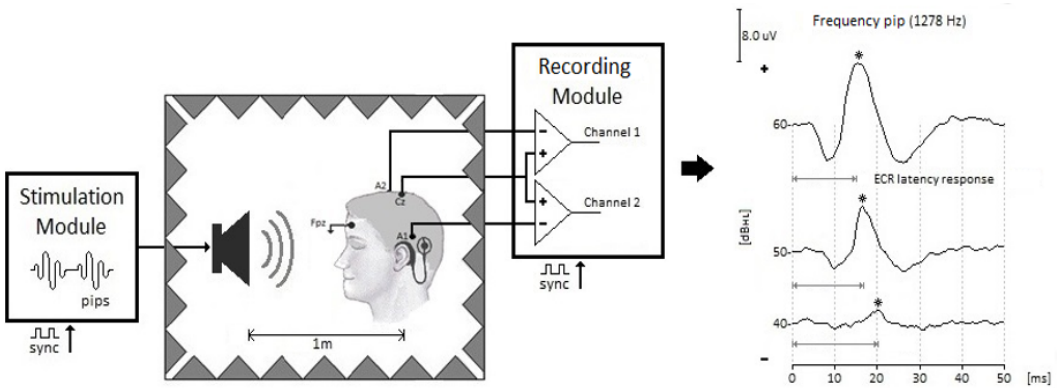

FIGURE 2. Block diagram of the system for ECR acquisition. The tone pip is generated in the Stimulation Module and sent to the patient while the patient is asleep inside the audiometric test booth. Two channels of EEG recording are used in the Acquisition Module. ECR waveforms obtained from an average of 100 EEG epochs due to a tone pip of 1278 Hz, for an increasing intensity level.

A PTA_{ECR} value was calculated considering intracochlear electrode central frequencies in the frequency range of 500 to 2000 Hz (540, 642, 762, 906, 1076, 1278, 1518 and 1803 Hz). Patients' hearing level was classified as normal (0-20 dB_{HL}), mild deafness (20-40 dB_{HL}), moderate deafness (40-60 dB_{HL}), severe deafness (60-80 dB_{HL}), and profound deafness (>80 dB_{HL}) [9]. Additional intermediate audiometric threshold values were interpolated to compare audiometry with ECR test result frequency by frequency.

Once ECR test finished, patients' parents answered the ASQ to provide information about the child's ability to use the CI in daily situations and the ability to detect, identify, and repeat 18 ambient sounds, as indicated in Table 1. Items evaluated were taken from the IT-MAIS/MAIS scale and the LiP Profile [20] [23]. The CST was designed to evaluate the patient's ability to detect, identify, and repeat 6 seconds duration real sounds and two-syllable Spanish words (Table 1).

All the CST items were normalized in amplitude and grouped in the following five groups: 1. An extended version of Ling sounds, which include eight representative phonemes of the speech spectrum [1] [24]; 2. Thirteen animal sounds; 3. Seven transportation sounds; 4. Ten ambient sounds [1] [25]; 5. Fourteen two-syllable Spanish words [1]. Ling sounds -*extended version*- and two-syllable Spanish words were recorded in a soundproof chamber at INR Audiology Service.

During CST, the patient remained seated at a distance of one meter from the loudspeaker. Three different sessions of 40 minutes were necessary to complete CST. At each session, cards with allusive images to sounds were given to the patient to keep their attention during the test. Each item was randomly played up to three times, starting at 60 dB_{HL}, while the therapist registered the patient's responses. The test was performed in the presence of the patients' parents, under the everyday CI program mode.

ASQ and CST scores achieved by patients were used to quantify the hearing performance at the end of the follow-up period. Table 1 details all test items and the evaluation criteria considered to achieve a hearing performance of 100%.

Statistical analysis

The dependent t-test was used to evaluate changes in audiometry and ECR thresholds for all the patients between sessions T1 and T2. The independent t-test was

TABLE 1. Itemize of test items taken into account to evaluate the hearing performance in implanted patients.

Items		Score [%]	Score assignment criteria
Auditory Skills Questionnaire			
1. IT-MAIS/MAIS	Does the child … 1. ask the CI is turned on, off or the child turned it on itself? 2. report the CI does not work? 3. respond to its name without visual cues in: silent environment? 4. noise environment 5. respond spontaneously to the house sounds? 6. respond spontaneously in unknown environments? 7. recognize auditory cues in the school? 8. distinguish different voices? 9. relate voice tone and meaning? 10. make a difference between voiced and voiceless?	15	At the beginning of the study, 89% of patients still had not acquired the necessary skills to cooperate with the sound detection task, so to know something about children's hearing abilities was through this standardized test.
2. Ambient Sounds Response * *Detection* * *Identification* * *Repetition*	bell, car, bird, train, whisper, baby crying, truck, siren, plane, faucet, barking, conversation, blender, firework, helicopter, telephone, motorcycle, knock-on-the-door.	15	Known sounds by children provided by their parents and therapists.
Calibrated Sound Test @ 60 and 40 dB_{HL} –*Detection, Identification and Repetition*–			
1. Ling Sounds -extended version-	/a/, /u/, /i/, /m/, /s/, /sh/, /e/, /o/.	40	Based on a standardized test used on CI programming and rehabilitation therapy and this is the first time that recorded phonemes are used.
2. Animal sounds	cat, dog, pig, cow, bird, lion, duck, sheep, horse, mouse, rooster, chicken, donkey.	10	Recorded animal and ambient sounds are used to evaluate the hearing perception of implanted patients for the first time.
3. Ambient sounds	bell, clock, siren, faucet, blender, fireworks, telephone, conversation, baby crying, knock-on-the-door.	10	
4. Transport sounds	car, train, truck, plane, ship, helicopter, motorcycle.	5	Transport recorded sounds presented similar spectral content.
5. Two-syllable Spanish words	ala (wing), caja (box), cama (bed), capa(cape), cara(face), casa (house), gafa (glasses), jarra (tankard), hada (fairly), lava (wash), maga (magician), rana (frog), rata (rat), vaca (cow).	5	Difficulty in evaluating these words in a recorded way due to patients' unfamiliarity with some of them.
Hearing performance		100	

used to evaluate differences between PTA and PTA_{ECR} by gender or age, at T1 and T2 sessions. The performance tests were evaluated by non-parametric analysis because the data did not show a normal distribution.

ASQ scores by gender and age were analyzed using the Mann-Whitney U test at each evaluation session. Scores obtained between T1 and T2 sessions were analyzed using the Wilcoxon rank-sum test. The CST scores were compared in patients grouped by age using the Mann-Whitney U test. The data were analyzed with NCSS V.9.0.5 [26], considering $p<0.05$ as significant value. Results are presented in terms of mean ± standard deviation (SD) and percentages.

RESULTS AND DISCUSSION

Of the 25 patients initially included, seven were eliminated because they did not complete the follow-up period. Two of them experienced problems with the implant and five did not complete the battery of tests. The average age of the 18 patients included in the analysis (9 girls and 9 boys) was 3.2±0.9 (1.8-5.7) years. The average auditory age (elapsed time between CI activation and ECR recording) was 7.2 months. Information about the patients is presented in Table 2.

Figure 3 shows the mean thresholds values for audiometry and ECR for all patients in sessions T1 and T2. A significant decrease in these thresholds is observed

TABLE 2. Patients included in the analysis, users of IC brand Advanced Bionics, model Hires 90K/HiFocus with complete insertion of intracochlear electrodes.

				T1 Evaluation			T2 Evaluation			
Subject	Gender	Diagnosis	CI processor	Chronological age	Auditory age	CI stimulation strategy	Chronological age	Auditory age	CI stimulation strategy	Time between T1 and T2
S1	F	BPSD	Harmony	3 y	7 m	HS/F	4 y, 2m	1 y, 5 m	HS/F	1 y, 2 m
S2	M	BSCMD	PSP	3 y, 8 m	5 m	HP/F	4 y, 7m	1 y, 1 m	HS/F	11 m
S3	M	BSCMD	Harmony	3 y, 8 m	1 m	HP/F	5 y	1 y, 2 m	HP/F	1 y, 4 m
S4	F	BPSD	Harmony	1 y, 10 m	4 m	HS/F	2 y, 8m	1 y, 1 m	HP/F	10 m
S5	F	BPSD	Harmony	3 y, 6 m	10 m	HP/F	4 y, 5 m	1 y, 7 m	HP/F	11 m
S6	F	BPSD	Harmony	3 y, 2 m	4 m	HP/F	3 y, 11 m	11 m	HP/F	9 m
S7	M	BPSD	Harmony	2 y, 4 m	4 m	HP/F	2 y, 11 m	10 m	HP/F	7 m
S8	M	BPSD	Harmony	3 y, 4 m	7 m	HP/F	4 y	1 a, 2 m	Hires-P	8 m
S9	M	BSCMD	Harmony	3 y	2 m	HP/F	3 y, 7 m	7 m	HP/F	7 m
S10	F	BSCMD	Harmony	2 y, 7 m	2 m	HP/F	3 y, 2 m	8 m	HP/F	7 m
S11	M	BPSD	Harmony	3 y, 5 m	4 m	HP/F	4 y, 2 m	11 m	Hires-P	9 m
S12	M	BPSD	Harmony	2 y, 5 m	6 m	HP/F	3 y, 1 m	1 y	HP/F	8 m
S13	F	BPSD	PSP	5 y, 8 m	1 y, 11 m	HP/F	6 y, 7 m	2 y, 6 m	HP/F	11 m
S14	F	BPSD	Harmony	3 y, 6 m	5 m	HP/F	4 y, 4 m	1 y, 1 m	HP/F	10 m
S15	M	BSCMD	Neptuno	1 y, 11 m	1 m	HP/F	2 y, 6 m	7 m	HS/F	7 m
S16	F	BSCMD	Harmony	3 y, 5 m	1 y, 7 m	HP/F	4 y, 1 m	2 y, 1 m	HP/F	8 m
S17	M	BPSD	Harmony	4 y, 4 m	1 y, 6 m	HP/F	5 y	2 y	HP/F	8 m
S18	F	BPSD	Harmony	2 y, 10 m	1 m	HP/F	3 y, 7 m	8 m	HS/F	9 m

Auditory age: CI use time elapsed from CI activation.
BSCMD: Bilateral Sensorineural Conductive Mixed Deafness.
BPSD: Bilateral Profound Sensorineural Deafness.
HP/F: Hires-P w/Fidelity 120.
HS/F: Hires-S w/Fidelity 120.

in T2 in relation to T1 ($p<0.05$), 11±2 dB_{HL} and 7±3 dB_{HL}, respectively, indicating an improvement in hearing thresholds over time. ECR thresholds were obtained at lower intensity than audiometry, 7 dB_{HL} at T1 y 3 dB_{HL} at T2, on average. Significant differences ($p<0.05$) were observed for 1076, 1278 and 6665 Hz in T1. In both testing sessions, the ECR threshold values showed less dispersion (≈10 dB_{HL}) than the audiometry (≈20 dB_{HL}).

Audiometric and ECR thresholds, PTA, PTA_{ECR}, ASQ and CST scores did not show significant differences when analyzed by gender. For the analysis by chronological age, patients were divided into 2 groups: 3 years and younger (G1; n=8) and older than 3 years (G2; n=10).

Table 3 shows significant PTA differences between G1 and G2 groups in the two sessions, with lower values in G2; while the PTA_{ECR} do not show significant changes between G1 and G2. In both sessions, PTA_{ECR} values were lower than PTA values for G1 group ($p<0.05$); 22 dB_{HL} at T1 session, and 13 dB_{HL} at T2 session. On the other hand, G2 group did not show significant differences between PTA and PTA_{ECR} values, 4 dB_{HL} at T1 ($p=0.37$) and 5 dB_{HL} at T2 ($p=0.29$).

Regarding ASQ, G1 group improved significantly their scores ($p<0.05$) from T1 to T2 session for IT-MAIS/MAIS and Ambient Sounds Response -*Detection*-. The scores improvement for *Identification* ($p=0.13$) and

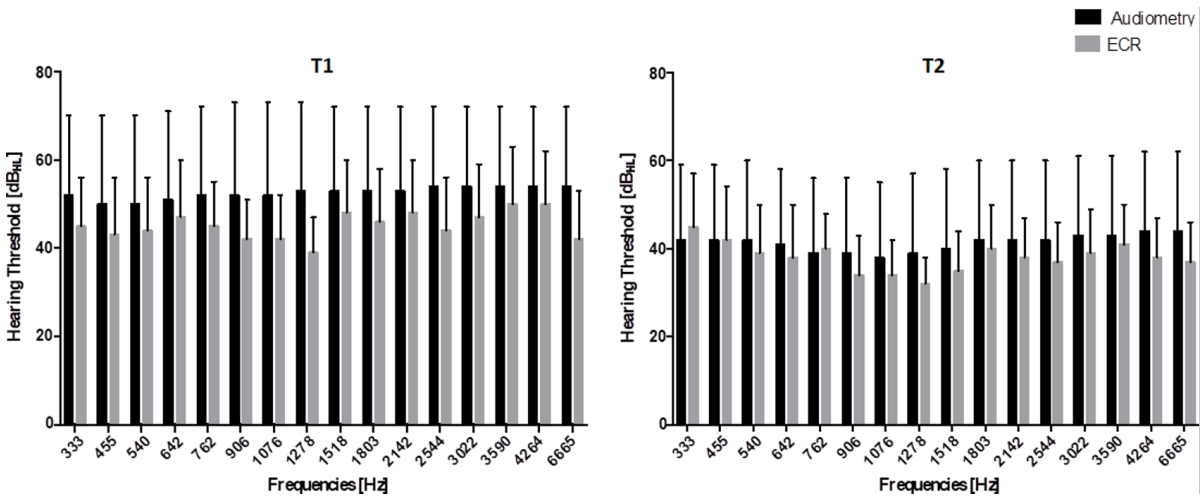

FIGURE 3. **Mean and standard deviation values of the audiometric and ECR thresholds by frequency obtained from 18 patients, ages 3.2±0.9 years, at T1 and T2 sessions.**

Repetition ($p=0.23$) ambient sounds were not significant. For G2 group there was not a score significantly improvement for any ASQ items. Better scores were obtained by G2 group at T1 and T2 sessions and only for *Identification*, significantly differences between groups were found at both sessions.

Figure 4 shows mean audiometric and ECR thresholds for both patient groups at T2 session when patients' cooperation got better allowing reliable audiometry. For G1 group ECR had lower threshold and less dispersion than audiometry. Significant differences ($p<0.05$), 17±2 dB_{HL} on average, between audiometric and ECR thresholds for frequencies above 1278 Hz were observed. For G2 group, audiometry and ECR had lower threshold than G1 group without significant differences between tests. Audiometry showed lower threshold, 5±3 dB_{HL} on average, and greater variability than ECR. In T2, after more than a year wearing the CI in most patients, the CST was evaluated to quantify the hearing performance, once the children became familiar with the use of the CI. G2 had better CST detection scores than G1.

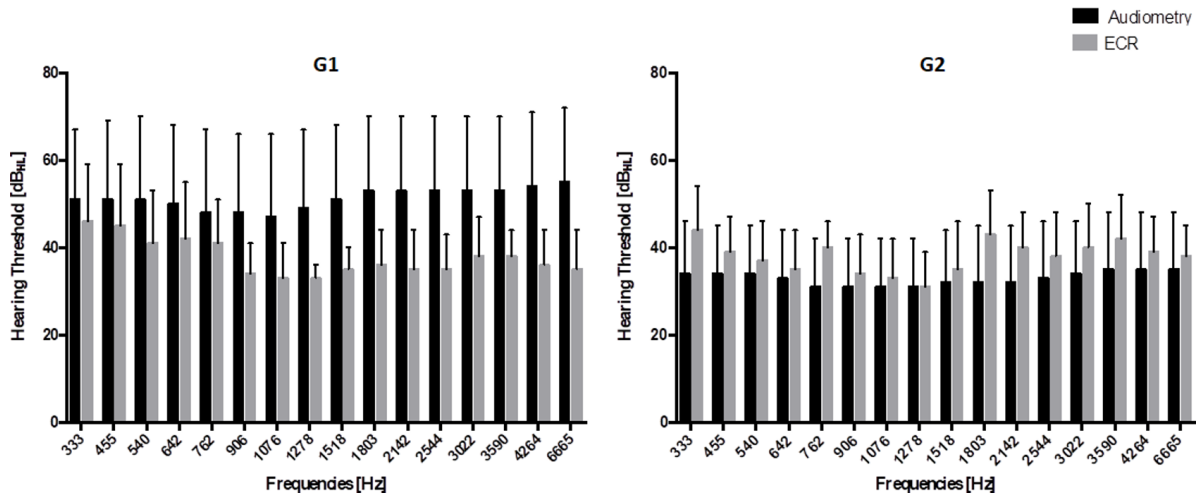

FIGURE 4. **Audiometric and ECR thresholds of patients 3 years of age or younger (group G1), and patients older than 3 years (group G2), in session T2.**

TABLE 3. Features of the patients in sessions T1 and T2.

Evaluation Session	T1			T2		
Patient group	G1 (n=8)	G2 (n=10)	*p*	G1 (n=8)	G2 (n=10)	*p*
Age [Years]						
Chronological	2.5 ± 0.5 (1.8-3)	3.8 ± 0.7 (3.2-5.7)	*0.05**	3.2 ± 0.6 (2.4-4.2)	4.6 ± 0.8 (3.9-6.6)	*0.05**
Auditory	0.3± 0.1 (0.1-0.5)	0.8 ± 0.6 (0.1-1.9)	*0.05**	0.9 ± 0.3 (0.6-1.4)	1.5 ± 0.6 (0.96-2.5)	*0.05**
Hearing level [dB_{HL}]						
PTA	68 ± 13 (50-90)	40 ± 11 (18-53)	*0.05**	51 ± 17 (19-80)	33 ± 12 (23-63)	*0.05**
PTA_{ECR}	46 ± 10 (32-61)	44 ± 10 (33-66)	*0.74*	38 ± 6 (27-44)	38 ± 7 (27-52)	*0.98*
Auditory Skills Questionnaire [%]						
1. IT-MAIS/MAIS	22	39	*0.31*	52	68	*0.12*
Ambient sound response						
Detection	30	71	*0.05**	81	87	*0.24*
Identification	15	48	*0.05**	47	79	*0.05**
Repetition	10	35	*0.17*	17	54	*0.05**

*Statistically significant between G1 and G2 at each session time.

The largest changes between the two groups (G1 and G2) were found in animal sounds, environmental sounds, and two-syllable Spanish words at 40 dB_{HL} (Table 4).For group G1, the PTA_{ECR} of 38±6 dB_{HL} seems to show better relationship with CST detection scores at 40 dB_{HL} than PTA of 51 ±17 dB_{HL} showed in Table 3. The average hearing performance obtained for G1 and G2 groups was 32% and 58% respectively, ($p<0.05$).

Below is an example of a patient (S2) older than 3 years, who is already familiar with the use of his CI, which has the audiometric and ECR thresholds of Figure 5 and the CST detection scores of Table 5.

According to audiometry patient S2 should detect all sounds at 40 dB_{HL}, however he is not. His CST detection scores are more related to ECR, where thresholds are below 40 dB_{HL} only at some frequencies.

A common practice for CI fitting purposes is to use ECAP threshold to establish M and T levels of the dynamic range of electrical current for a limited number of intracochlear electrodes, without considering the CI sound processor operation. Unfortunately, ECAP is not a predictor of post-operative performance [27]. Some studies had shown that ECAP threshold tends to fall over time [11], and is absent in approximately 5% of

TABLE 4. Average CST detection scores achieved for patients groups at T2 session.

Test intensity	60 dB_{HL} [%]			40 dB_{HL} [%]		
Patient group	G1 (n=8)	G2 (n=10)	*p*	G1 (n=8)	G2 (n=10)	*p*
Ling sounds -extended version-	78	94	*0.41*	39	78	*0.07*
Animal sounds	77	95	*0.17*	39	75	*0.05**
Transport sounds	71	92	*0.31*	43	63	*0.24*
Ambient sounds	74	94	*0.12*	38	74	*0.05**
Two-syllable Spanish words	63	92	*0.17*	23	58	*0.05**

*Statistically significant between G1 and G2 at each intensity.

patients [12] [28]. ECAP thresholds profile does not fully coincide with M levels profile [12], hence final M and T levels values should be confirmed by expert observation of the patient's auditory behavior and successive application of audiometry, which is not an easy task in pediatric patients.

TABLE 5. Calibrated Sounds Test detection score for patient S2 in session T2.

Test intensity	60 dB_{HL}	40 dB_{HL}
1. Ling sounds -extended version-	100%	63%
2. Animal sounds	100%	99%
3. Transportation sounds	100%	57%
4. Ambient sounds	100%	90%
5. Two-syllable Spanish words	100%	64%

Bear in mind that audiometry was not originally designed for implanted patients. Thus, the standard test frequencies have no relationship with the frequency bands assigned to the intracochlear electrodes. This may cause to underestimate the hearing threshold by up to 3 dB when test frequency falls within the bandwidth of any band-pass filter or an inadequate estimation of hearing threshold if it falls outside bandwidth.

Due to its objective nature, ECR can be use since the initial CI programming. Furthermore, the utilization of sound stimulus of frequency equal to the central frequency assigned to each stimulation electrode allows individual addressing of intracochlear electrodes.

Additionally, ECR thresholds showed less dispersion than audiometry, probably due to its objective nature compared to the subjectivity of the audiometry which generated greater deviations.

The high variability found in the audiometry of the youngest patients, G1, may be due to their short age, limited experience using the CI, and the difficulty they presented in performing the test.

In the other hand, it was difficult to obtain thresholds at high frequencies in these patients. For older children, G2, according to the audiometry, all of them would be in mild deafness, with hearing thresholds below 40 dB_{HL}, Figure 4, however the CST shows detection scores less than 80% for 40 dB_{HL}.

This is probably due to the fact that most patients have not developed the skills to detect the different sounds evaluated. G1 achieved a total CST detection score of 55% and G2 of 82% after approximately one year of CI use, Table 4.

The patient S2 hearing thresholds illustrate how the inherent subjectivity of audiometry affected the determination of hearing thresholds for test frequencies below 906 Hz, where an average difference of 20 dB_{HL} was observed with respect to the ECR thresholds after 8.4 months of CI activation (Figure 5).

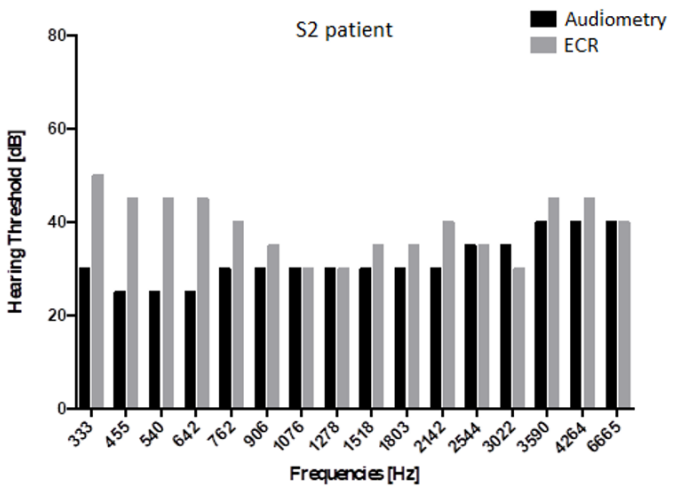

FIGURE 5. Audiometric and ECR thresholds obtained for patient S2 in session T2.

This study corroborated the feasibility of evaluating the patient-CI pair making the use of known frequency and variable intensity tone pips with the CI operating under everyday usage conditions, which take account of the effect of microphone sensitivity and sound processor gain.

A limitation of the ECR test is that requires patients to remain asleep during the entire test. Nevertheless, the results showed the possibility of knowing the minimum sound intensity level for the detection of ECR corresponding to the probable hearing threshold. The relationship between patients' hearing performance improvement and ECR was also shown after modifying T and M levels, and/or extent of the dynamic range of electrical current derived from the amplitude and waveform analysis of the ECR.

The promising results provided in this study lead us to propose ECR as a tool for the evaluation and follow-up of CI users, especially for ages ≤ 3 years. Although more studies are needed to show the possible benefits of this objective approach from the activation of the CI.

CONCLUSIONS

The most significant differences between audiometric and ECR thresholds obtained by PTA and PTA_{ECR} were observed for patients aged 3 years or younger. Additionally, no statistically significant differences were obtained for older patients. However, the similarity in the threshold profiles obtained in both tests allows us to think about the possibility of obtaining hearing thresholds using ECR.

Furthermore, our study highlighted the limitations of audiometry to provide information on the hearing threshold due to subjectivity and the absence of a relationship between test frequencies and the central frequencies of the band pass filter assigned to each CI intracochlear electrode.

The application of ASQ and CST tests was very difficult due to the age of the patients and the lack of experience in the use of the CI; however, these made possible to relate auditory behavior with audiometry and ECR, where a better relationship was shown between ASQ and CST scores and ECR thresholds.

This research project showed the possible benefits of employing ECR to estimate hearing thresholds per frequency in pediatric implanted patients, especially younger than 3 years, as well as the implementation of ASQ and CST to quantify hearing performance. During the patients' follow-up period, the methodology developed helped audiologists and therapists to identify some difficult situations related to CI programming and rehabilitation therapy strategy, helped them to quantify and improve the performance of their patients, and to have additional information about their hearing.

ABBREVIATIONS

- ***ASQ***: Auditory Skills Questionnaire
- ***BSCMD***: Bilateral Sensorineural Conductive Mixed Deafness
- ***BPSD***: Bilateral Profound Sensorineural Deafness
- ***CI***: cochlear implant
- ***CST***: Calibrated Sounds Test
- ***ECR***: Electrical Cochlear Response
- ***ECR threshold***: hearing threshold estimated by ECR
- ***G1***: patients group ages 3 years and younger
- ***G2***: patients group older than 3 years
- ***HP/F***: Hires-P w/Fidelity 120
- ***HS/F***: Hires-S w/Fidelity 120
- ***PTA***: Pure Tone Average in the frequency range 500 to 2000 Hz
- $\boldsymbol{PTA_{ECR}}$: Pure Tone Average for ECR test in the frequency range 500 to 2000 Hz
- ***T1***: first evaluation sessions
- ***T2***: second evaluation session.

AUTHOR CONTRIBUTIONS

A.K.Q. and J.M.C. contributed with the experimental design; data acquisition, analysis, and interpretation, and drafting the manuscript. In addition, A.K.Q. contributed with reviewing the manuscript and J.M.C contributed with critical revision of the manuscript and gave the final approval for publication. M.P.G. and

N.E.B. contributed to the study design, data analysis and interpretation, critical revision of the manuscript, and gave the final approval for publication.

ACKNOWLEDGMENTS

This study is part of Agar Quintana's graduate research as a doctoral student in Biomedical Engineering at UAM-Iztapalapa, Mexico City. Her studies were supported by a grant from CONACyT. The authors thank patients and their parents for their kindly cooperation We also thank Dr. Maria E. Mena and Dr. Laura E. Chamlati from the National Institute of Rehabilitation for their valuable support with patient's recruitment and following.

ETHICAL STATEMENT

Ethical Research Committee of National Institute of Rehabilitation (INR) approved and supervised the study complied with all applicable research and ethical standards and laws followed by the Declaration of Helsinki principles. All patients' parents signed informed consent.

REFERENCES

[1] Flores-Beltran L. The Auditory-Verbal Therapy: a Trainning Program for Professionals in the Field of Hearing Disorders [Ph.D.'s thesis]. [Honolulu]: Atlantic International University, 2007. 251p.

[2] Manrique Rodríguez M, Huarte Irujo A. Organisation of a Cochlear Implant Programme. Acta Otorrinolaringol [Internet]. 2013;64(1):55-67. Available from: https://doi.org/10.1016/j.otoeng.2013.02.006

[3] Mitchell RM, Christianson E, Ramirez R, Onchiri FM, Horn DL, Pontis L, et al. Auditory comprehension outcomes in children who receive a cochlear implant before 12 months of age. Laryngoscope [Internet]. 2020;130(3):776-81. Available from: https://doi.org/10.1002/lary.28061

[4] Baudhuin J, Cadieux J, Firszt JB, Reeder RM, Maxson JL. Optimization of Programming Parameters in Children with the Advanced Bionics Cochlear Implant. J Am Acad Audiol [Internet]. 2012;23(5):302-12. Available from: https://doi.org/10.3766/jaaa.23.5.2

[5] Eisenberg LS. Clinical Management of Children With Cochlear Implants. 2nd ed. San Diego: Plural Publishing Inc; 2009. 890p.

[6] Guenser G, Laudanski J, Phillipon B, Backus BC, Bordure P, Romanet P, et al. The relationship between electrical auditory brainstem responses and perceptual thresholds in Digisonic® SP cochlear implant users. Cochlear Implants Int [Internet]. 2015;16(1):32-8. Available from: https://doi.org/10.1179/1754762814Y.0000000082

[7] Lira De Andrade KC, De Caevalho Leal M, Ferreira Muniz L, De Lemos Menezes P, Gomes De Albuquerque KM, Tenório A. The importance of electrically evoked stapedial reflex in cochlear implant. Braz J Otorhinolaryngol [Internet]. 2014;80(1):68-77. Available from: https://doi.org/10.5935/1808-8694.20140014

[8] Gattaz G, Battmer RD, Lehnhardt E, Gnadeberg D. [Correlation between electrically-induced stapedius reflex and discomfort threshold in cochlear implant patients]. HNO [Internet]. 1992;40(12):480-3. German. Available from: https://pubmed.ncbi.nlm.nih.gov/1493968/

[9] Van Den Abbeele T, Noël-Petroff N, Akin I, Caner G, Olgun L, Guiraud J, et al. Multicentre investigation on electrically evoked compound action potential and stapedius reflex: how do these objective measures relate to implant programming parameters? Cochlear Implants Int [Internet]. 2012;13(1):26-34. Available from: https://doi.org/10.1179/1754762810Y.0000000001

[10] Walkowiak A, Lorens A, Polak M, Kostek B, Skarzynski H, Szkielkowska A, et al. Evoked Stapedius Reflex and Compound Action Potential Thresholds versus Most Comfortable Loudness Level: Assessment of Their Relation for Charge-Based Fitting Strategies in Implant Users. ORL [Internet]. 2011;73(4):189-95. Available from: https://doi.org/10.1159/000326892

[11] Marsella P, Scorpecci A, Pacifico C, Resca A, Vallarino MV, Ingrosso A, et al. Safety and Functional Results of Early Cochlear Implant Switch-On in Children. Otol Neurotol [Internet]. 2014;35(2):277-82. Available from: https://doi.org/10.1097/mao.0000000000000259

[12] Botros A, Banna R, Maruthurkkara S. The next generation of Nucleus® fitting: a multiplatform approach towards universal cochlear implant management. Int J Audiol [Internet]. 2013;52(7):485-94. Available from: https://doi.org/10.3109/14992027.2013.781277

[13] American Speech-Language-Hearing Association. Guidelines for Methods for Manual Pure-Tone Threshold Audiometry [Internet]. New York: Acoustical Society of America; 2004. Available from: *https://www.asha.org/policy/gl2005-00014/*

[14] Caner G, Olgun L, Gültekin G, Balaban M. Optimizing Fitting in Children Using Objective Measures Such as Neural Response Imaging and Electrically Evoked Stapedius Reflex Threshold. Otol Neurotol [Internet]. 2007;28(5):637-40. Available from: https://doi.org/10.1097/mao.0b013e3180577919

[15] Katz J. Hand book of clinical audiology. 7th ed. Philadelphia: Wolters Kluwer; 2009. 927p.

[16] Cosetti M, Shapiro W, Green J, Roman B, Lalwani A, Gunn S, et al. Intraoperative Neural Response Telemetry as a Predictor of Performance. Otol Neurotol [Internet]. 2010;31(7):1095-9. Available from: https://doi.org/10.1097/mao.0b013e3181ec1b8c

[17] Gifford RH. Cochlear Implant Patient Assessment: Evaluation of Candidacy, Performance, and Outcomes. 2nd ed. San Diego: Plural Publishing Inc; 2020. 189p.

[18] Cornejo Cruz JM, Granados Trejo MP, inventors; Systems and methods for detecting and using an electrical cochlear response ("ECR") in analyzing operation of a cochlear stimulation system. WO2010041920A1. 2010. Spanish.

[19] Quintana A, Beltran N, Granados PM, Chamlati E, Mena M, Cornejo JM. Objective Approach to Audiometry in the Pediatric Implanted Patient. In: Braidot A, Hadad A. (eds.). VI Latin American Congress on Biomedical Engineering CLAIB 2014 [Internet]. Paraná, Argentina: IFMBE Proceedings, Springer Cham. 2014;49:707-10. Available from: https://doi.org/10.1007/978-3-319-13117-7_180

[20] Cavicchiolo S, Mozzanica F, Guerzoni L, Murri A, Dall'Ora I, Ambrogi F, et al. Early prelingual auditory development in Italian infants and toddlers analysed through the Italian version of the Infant-Toddler Meaningful Auditory Integration Scale (IT-MAIS). Eur Arch Otorhinolaryngol [Internet]. 2018;275(2):615-22. Available from: https://doi.org/10.1007/s00405-017-4847-6

[21] Dos Santos Pedrett M, Pedrett Costa MB. Application of RDLS scale to characterize oral language profiles in children using cochlear implant. CoDAS [Internet]. 2019; 31(5):1-7. Portuguese. Available from: https://doi.org/10.1590/2317-1782/20192018158

[22] Klem GH, Lüders HO, Jasper HH, Elger C. The ten-twenty electrode system of the International Federation. The International Federation of Clinical Neurophysiology. Electroencephalogr Clin Neurophysiol Suppl. 1999;52:3-6.

[23] Fu Y, Chen Y, Xi X, Hong M, Chen A, Wang Q, Wong L. [Development of early auditory and speech perception skills within one year after cochlear implantion in prelingual deaf children]. Zhonghua Er Bi Yan Hou Tou Jing Wai Ke Za Zhi. 2015;50(4):274-80. Chinese.

[24] Ling D. Speech and the hearing-impaired child Theory and Practice. Washington: The Alexander Graham Bell Association'for the Deaf. Inc; 1976. 402p.

[25] Archbold S. Organisation of the Nottingham Paediatric Cochlear Implant Programme. Central East Eur J. 1996;1(1):20-7.

[26] NCSS Software. NCSS 9 Statistical Software. Kaysville, Utah, USA. 2013.

[27] El Shennawy AM, Mashaly MM, Shabana MI, Sheta SM. Telemetry changes over time in cochlear implant patients. Hear Balance Commun [Internet]. 2016;13(1):24-31. Available from: https://doi.org/10.3109/21695717.2014.999427

[28] Moura ACG, Goffi-Gomez MVS, Couto MIV, Brito R, Tsuji RK, Befi-Lopes DM, et al. Longitudinal Analysis of the Absence of Intraoperative Neural Response Telemetry in Children using Cochlear Implants. Int Arch Otorhinolaryngol [Internet]. 2014;18(4):362-8. Available from: https://doi.org/10.1055/s-0034-1372510